

# Advancements in TlBr for Gamma-Ray Detection and Imaging

by

Sean P. O'Neal

A dissertation submitted in partial fulfillment  
of the requirements for the degree of  
Doctor of Philosophy  
(Nuclear Engineering and Radiological Sciences)  
in The University of Michigan  
2018

Doctoral Committee:

Professor Zhong He, Chair

Professor Igor Jovanovic

Assistant Professor Kai Sun

Dr. Steven Payne, Lawrence Livermore National Laboratory

© Sean P. O’Neal 2018

---

All Rights Reserved

ORCID iD: 0000-0003-3851-5344

To my grandfather: I am sad that you cannot be here.

## ACKNOWLEDGEMENTS

A doctoral thesis is in some ways an individual work, but in many ways a group achievement. I would like to begin by thanking my adviser Prof. Zhong He. Thank you for convincing me to join your group; I have learned so much from you over the years and have come out a better scientist, researcher, and person. I would also like to thank generally all the past students who helped develop the methods I used and also created the great working culture in the Orion Research Group. As Isaac Newton said, “If I have seen further it is only by standing on the shoulders of giants.”

Personally I would like to thank my coworkers and friends who helped keep me motivated and made coming into the lab an enjoyable experience. To Will Koehler, thanks for getting me started and helping me develop the intuition that I need to work on this hard material. To Charles Leak, thanks for sharing your enthusiasm with me for both work and non-work related topics and challenging me to extend my own understanding by explaining it to you. I wish you the best as you continue to work on TlBr. To Michael Striecher, thanks for your friendship, for the memories during travel to conferences, and for your very insightful perspective when I wanted to discuss theory. To Steven Brown, thanks for a great example of good experimental design and your infectious attitude of excellence. To David Goodman, thanks for keeping me challenged by asking good questions and thinking about all sorts of new ideas. For those who helped review my draft, Jiawei Xia, Bennett Williams, Daniel Shy, David Goodman, and Charles Leak thank you very much. And thanks in general to everyone else in the group for making the lab a fun place to be.



A special thanks to Jim Berry for putting up with me and always being willing to help when I needed something. And thanks to Dr. Yuefeng Zhu without whose incredible work, the digital ASIC technology would not be possible. I would also like to thank my collaborators at RMD: Len Cirignano, Hadong Kim, and Kanai Shah. Thank you for providing me material to work on, I hope my contributions have helped you advance the development of TlBr. I would also like to thank my committee members: Professors Igor Jovanovic and Kai Sun, and Dr. Steve Payne. Thank you for taking time understand and challenge my work so that I can make meaningful contributions to the scientific community.

I would also like to thank Ben Sturm, Nerine Cherepy, and Steve Payne at LLNL because my first internship there got me excited about research and led me to pursue my doctorate. There are many others who have contributed professionally to my development that I cannot name them all, but thank you everyone in the NERS department for making it an exciting place to be, and especially to the Chair Prof. Ron Gilgenbach for making it a great place and for believing in me enough to let me teach NERS 211.

But my graduate time has not only been work. I would also like to thank my friends and family for keeping me sane throughout the process. Both those at the University like Tim Burke, Matt Marcath, and Marc Rusch who were always available to chat. To those outside the University like Brad Stark and Kevin Chang who helped me keep the work-life balance in the right place.

Thanks again to my parents for equipping me with the skills to succeed and for your unwavering support in the ups and the downs for the last 5 years. I could have not done it without everyone's support.

\*This work was funded by a by DNDO of DHS under a subcontract through Lawrence Livermore National Laboratory (contract #DE-AC52-07NA27344) and Radiation Monitoring Devices, Inc. (contract #HSHQDN-16-C-00024).

# TABLE OF CONTENTS

<b>DEDICATION</b> . . . . .	ii
<b>ACKNOWLEDGEMENTS</b> . . . . .	iii
<b>LIST OF FIGURES</b> . . . . .	viii
<b>LIST OF TABLES</b> . . . . .	xiv
<b>ABSTRACT</b> . . . . .	xv
<b>CHAPTER</b>	
<b>I. Introduction</b> . . . . .	1
1.1 Types of Neutral Particles . . . . .	2
1.2 The Ideal Photon Detector . . . . .	2
1.2.1 Detection Efficiency . . . . .	3
1.2.2 Source Identification . . . . .	3
1.2.3 Engineering Concerns . . . . .	4
1.3 Currently Available Technologies . . . . .	4
1.3.1 Room Temperature Semiconductors . . . . .	6
1.4 TlBr . . . . .	8
1.4.1 Challenges - Polarization . . . . .	8
1.4.2 Challenges - Conditioning . . . . .	9
1.4.3 Challenges - Non-Uniformity . . . . .	10
1.5 State of the Art in TlBr . . . . .	10
1.6 Contributions of This Work . . . . .	13
<b>II. Theory</b> . . . . .	14
2.1 The Energy Spectrum . . . . .	14
2.2 Energy Resolution . . . . .	17
2.2.1 Fundamental Limit . . . . .	17
2.2.2 Degradation of Energy Resolution . . . . .	18

2.3	The Shockley-Ramo Theorem . . . . .	19
2.3.1	Integral form of the Shockley-Ramo Theorem . . . .	20
2.3.2	Single-Polarity Charge Sensing . . . . .	21
2.3.3	3D Correction . . . . .	22
2.4	$\mu\tau$ -Product . . . . .	24
2.4.1	Two-bias Method . . . . .	26
2.4.2	Hecht-Fitting . . . . .	27
<b>III.</b>	<b>Methods . . . . .</b>	<b>28</b>
3.1	Fabrication . . . . .	28
3.1.1	Growth . . . . .	28
3.1.2	Fabrication . . . . .	29
3.2	Read Out . . . . .	32
3.2.1	3x3 Detectors . . . . .	32
3.2.2	Large Volume Detectors . . . . .	35
3.3	Digital Signal Processing . . . . .	36
3.3.1	CRRC . . . . .	36
3.3.2	Simple Subtraction . . . . .	36
3.4	Decay Correction . . . . .	38
3.4.1	Theory of Decay Correction . . . . .	38
3.4.2	Validation on Simulated Waveforms . . . . .	39
3.4.3	Validation on Measured Waveforms . . . . .	40
<b>IV.</b>	<b>Material Characterization . . . . .</b>	<b>43</b>
4.1	Ionization Energy . . . . .	43
4.1.1	Comparison . . . . .	45
4.1.2	Detectors . . . . .	46
4.1.3	Measurements . . . . .	47
4.1.4	Results . . . . .	48
4.1.5	Prediction of Limiting Energy Resolution . . . . .	53
4.1.6	Conclusions . . . . .	54
4.2	Anode Slopes . . . . .	56
4.2.1	Causes of High Energy Tails . . . . .	57
4.2.2	Analysis Tools . . . . .	59
4.2.3	Analysis of Detrapping Hypothesis . . . . .	61
4.2.4	Quantification of Extra Charge . . . . .	63
4.2.5	Positive Bias . . . . .	66
4.2.6	Conclusions . . . . .	68
4.3	Storage Effects . . . . .	69
4.3.1	Cause: Surface Effect . . . . .	70
4.3.2	Refabrication . . . . .	71
4.3.3	Conclusions . . . . .	73

<b>V. Extending Detector Lifetime</b>	75
5.1 Ionic Conduction Mitigation (2°C Operation)	76
5.1.1 Leakage Current and Lifetime	76
5.1.2 Leakage and Temperature	77
5.1.3 Detectors and Experimental Design	78
5.1.4 Results: Detector Pair	79
5.1.5 Results: Long-term Operation	82
5.1.6 Conclusions	84
5.2 Surface Preparation	85
5.2.1 Detectors	85
5.2.2 Results - Detector 935-38AA2L	85
5.2.3 Results - Detector 935-38AA3L	88
5.2.4 Failure Mechanism	89
5.2.5 Detector 125ABA2R	91
5.2.6 Conclusions	92
<b>VI. ASIC Systems</b>	93
6.1 v1.2 System	94
6.1.1 System Overview	94
6.1.2 Cooling Performance	96
6.1.3 Results	98
6.2 v2.2 Benchtop System	104
6.2.1 System Overview	104
6.2.2 Triggering	106
6.2.3 Sampling Frequency Effects	107
6.2.4 Degradation	108
6.3 Espresso UM Hand-held System	110
6.4 System Overview	110
6.4.1 Results	112
6.5 Conclusions	113
<b>VII. Conclusions and Future Work</b>	114
7.1 Conclusions	114
7.2 Future Work	115
<b>BIBLIOGRAPHY</b>	119

## LIST OF FIGURES

### Figure

1.1	Spectra at $-20^{\circ}\text{C}$ and three days at room temperature of detector 44AB1R showing the degrading performance due to polarization. Spectra are shifted vertically for clarity. . . . .	9
1.2	Picture of the anode electrode from an (a) normal and (b) polarized TlBr detector showing how room-temperature operation has degraded the contact surface. . . . .	10
1.3	Energy resolution versus time for detector 44B2L at $-20^{\circ}\text{C}$ showing improvement over the first few days referred to as conditioning. . . .	11
1.4	Example TlBr $^{137}\text{Cs}$ spectrum from a $5\text{x}5\text{x}5\text{ mm}^3$ TlBr detector showing performance of 1% FWHM . . . . .	11
1.5	Pixel-by-pixel breakdown of the spectrum from Fig. 1.4, with the best and worst pixel highlighted. The best pixel (blue) shows a resolution of 0.81% FWHM where the worst pixel (green) shows a resolution of 3.07% FWHM. . . . .	12
2.1	Example TlBr spectrum with the key features labeled. . . . .	15
2.2	Comparison of the photopeak interaction probability between TlBr and CZT in a 5mm thick detector using the data from NIST. [33] . .	16
2.3	Geometry of 11x11 pixelated electrodes. Each pixel pad is $0.9 \times 0.9\text{ mm}^2$ with a $100\text{ }\mu\text{m}$ gap between pixels. The cathode is planar and the detector is 5 mm thick. . . . .	21
2.4	Weighting potential for the (a) anode (blue) and (b) cathode (red) for the electrode geometry shown in Fig. 2.3. . . . .	22
2.5	Depth separated spectrum for one pixel. The photopeak amplitude decreases towards the anode side (green) due to the non-ideal weighting potential and towards the cathode side (red) due to trapping. .	23
2.6	Example of depth correction on the data shown in Fig. 2.5, (a) shows the raw spectrum at 3.56% FWHM and (b) the depth-corrected spectrum at 2.15% FWHM. . . . .	24
3.1	Photograph of the (a) TMZ growth setup, showing the two heaters and the TlBr material loaded in a quartz ampule and (b) the finished TlBr boule showing the pure end (seed) and less pure end (tail). . .	29
3.2	Diagram showing the boule location of detector 58A3L. . . . .	30

3.3	Picture of a packaged 3x3 TlBr detector . . . . .	30
3.4	Picture of an 11x11 TlBr array showing the (a) contacts before bonding and (b) after flip-chip bonding to a substrate board. Silver expoy is used to bond a cathode wire to the electrode. . . . .	31
3.5	Layout of 3x3 detector testing board. . . . .	33
3.6	Picture of the detector testing board. . . . .	33
3.7	Picture of the outside of the detector testing box showing the connections to the data acquisition PC. . . . .	34
3.8	Basic layout of the digital ASIC systems, showing the important components. . . . .	36
3.9	Example of CRRC4 digital shaping on an anode TlBr waveform showing the raw waveform (blue), shaped waveform (red) and determined amplitude (green). . . . .	37
3.10	Example of 100-point simple subtraction used to determine the amplitude of a TlBr anode waveform. . . . .	37
3.11	Example raw waveforms take at (a) 10MHz and (b) 2MHz showing the effects of preamplifier decay. . . . .	38
3.12	Decay correction examples using simple simulated data. . . . .	40
3.13	Decay correction examples using simulated data with hole drift, Gaussian noise, and a large baseline decay. . . . .	41
3.14	Example of decay correction on a measured waveform at 5MHz showing both the (a) raw and (b) corrected waveforms. Two regions are highlighted in the tail of the raw waveform which are used to measure the amount of decay in the waveform. . . . .	42
3.15	Distribution of tail decay in (a) raw and (b) decay corrected waveforms using the ratio of the green region to the red region in Fig. 3.14(a) . . . . .	42
4.1	Ionization energy versus bandgap for many semiconductor materials from Ref [47], using their value of the ionization energy for TlBr. TlBr falls off the Klein relation on a line with a different slope. . . . .	44
4.2	Block diagram of the Si detector measurement system showing the RC filter on the power supply, the PIN diode, and the shaping amplifier used for triggering. . . . .	47
4.3	Example Si detector waveform showing full collection time in the 51.2 $\mu s$ window (512 samples at 10 MHz). The waveform is linear as expected for the planar PIN diode. . . . .	48
4.4	$^{241}\text{Am}$ spectrum in detector 935-38AA2L (pixel 3) for multiple detector biases. . . . .	49
4.5	Photopeak centroid versus bias for detector 935-38AA2L showing fits for both the classic Hecht relation (Eq. 2.28) and the modified Hecht relation (Eq. 2.31). (Note: these fits are very similar and overlap in the figure). . . . .	50
4.6	Ionization energy versus bandgap for many semiconductor materials using the value for TlBr obtained in this work. Other materials ionization energies from Refs [1] and [12]. . . . .	55

4.7	(a) Depth-corrected spectra for detector 935-38AA2L using simple subtraction to determine the pulse amplitudes showing the high-energy tailing on the photopeak and (b) raw spectrum in a single depth bin showing the high energy tail is present on the voxel level.	56
4.8	Comparison between a typical TlBr anode waveform (blue) and one showing an anode slope (red).	57
4.9	Comparison of (a) typical flat cathode waveform (blue) and (b) one showing hole motion (red).	58
4.10	Anode weighting potential, demonstrating the small amount of signal holes contribute to the anode signal for an event in the middle of a 5 mm thick detector with a 1 mm pitch.	58
4.11	Example of prompt subtraction shaping. The raw waveform is shown in blue and the fast shaper is shown in red. The horizontal green line shows the amplitude determined from prompt subtraction.	60
4.12	Depth-corrected spectra for detector 935-38AA2L using both simple subtraction (red) and prompt subtraction (blue) to determine the pulse amplitude. With the removal of the tail, the resolution improves from 4.59% FWHM at 662 keV to 2.21%.	61
4.13	Mean (a) anode and (b) cathode waveforms for the cathode side, near cathode side, middle, and anode side of detector 935-38AA2L at 1000 V and 2 MHz.	62
4.14	Comparison of the average waveforms from the middle of the detector at two different biases.	63
4.15	Planar electrode waveform in positive bias (+2000V), with the red line showing the amplitude from electrons determined by prompt subtraction.	67
4.16	Trapping on planar electrode (holes) in reverse bias (+2000V) with an exponential fit.	67
4.17	Resolution for each testing for detector 58A3L showing the degradation with storage time.	70
4.18	Resolution (%FWHM at 662 keV) versus depth for two testings of detector 935-16B1L.	71
4.19	Photopeak centroid versus depth for the September 2015 testing of detector 935-16B1L. The photopeak centroids do not decrease towards the cathode side indicating very low trapping.	72
4.20	Energy resolution versus time for each testing of detector 935-38AA1R at $-20^{\circ}\text{C}$ .	74
5.1	Leakage current versus time for one anode pixel of detector 935-34AA1L during polarization, showing the increase as the device fails.	77
5.2	Leakage current versus temperature for detector 935-29AA1-3.	78
5.3	Depth-corrected single-pixel energy resolution versus time for detectors (a) 935-43BA1L at $2^{\circ}\text{C}$ and (b) 935-43BA1R at $-20^{\circ}\text{C}$ .	79
5.4	Comparison of the photopeak centroids versus depth for multiple days for detector (a) 935-43BA1L at $2^{\circ}\text{C}$ and (b) 935-43BA1R at $-20^{\circ}\text{C}$	81

5.5	Resolution versus time for detector 935-16B1R at both $-20^{\circ}\text{C}$ and $2^{\circ}\text{C}$ . After 43 total days of testing, the device polarized in less than one day at room temperature. . . . .	82
5.6	Resolution versus depth for two characteristic pixels of detector 935-16B1R comparing the performance on the best and worst day at $2^{\circ}\text{C}$ . . . . .	83
5.7	Drift velocity versus depth for two characteristic pixels of detector 935-16B1R showing the fast region which develops on the anode side during $2^{\circ}\text{C}$ operation. . . . .	84
5.8	Depth-corrected single-pixel resolution versus time for the first room-temperature operation of detector 935-38AA2L. . . . .	86
5.9	Photopeak centroids versus depth for detector 935-38AA2L at different days showing increases in the cathode side amplitude with time, indicating a reduction in overall trapping. . . . .	87
5.10	Resolution versus time for the second testing of detector 935-38AA2L at room-temperature about one year after the initial testing. . . . .	88
5.11	Depth-corrected single-pixel energy resolution versus time for room-temperature operation of detector 935-38AA3L. The detector experienced breakdown multiple times; each run represents continuous operation between breakdown events. . . . .	89
5.12	Photopeak centroids versus depth for detector 935-38AA3L at different days showing both increasing and decreasing centroids with time. . . . .	90
5.13	Picture of the (a) top and (b) side of detector 935-38AA3L after greater than 100 days of operation at room-temperature compared with the (c) top and (d) side of a normal TlBr detector. The side surfaces are covered in a $\text{TlO}_x$ coating, with one corner showing a brown spot which is likely Br. . . . .	91
5.14	Single-pixel energy resolution versus time for detector 125ABA2R. . . . .	92
6.1	Picture of the VAD_UM v2.2 digital ASIC capable of reading out 121 pixels compared with the eV-509 preamplifier used for reading out a single pixel in the 3x3 readout system. . . . .	94
6.2	Picture of the first generation system based on the VAD_UM v1.2 ASIC. Showing the (a) Faraday cage, (b) Espresso board, and (c) UMROB. The power supplies are also labeled based on their numbers in Fig. 6.3, with the computer and high voltage power supply off screen. . . . .	95
6.3	Block diagram of the v1.2 ASIC system. Power supplies and power lines shown in blue. . . . .	96
6.4	Diagram of the two-stage TEC cooling system showing the copper cold finger connected to the ASIC. . . . .	97
6.5	Total TEC power versus ASIC temperature for the VAD_UM v1.2 ASIC system. . . . .	97
6.6	Pictures of the (a) condensation in the system and (b) the system after two weeks of operation showing the effectiveness of the condensation mitigation. . . . .	98



6.7	Photopeak waveforms showing the anode (blue) and cathode (red) in the v1.2 system showing full collection on the cathode side. . . . .	99
6.8	Anode (blue) and cathode (red) waveforms from the (a) standard trigger cell and (b) shifted trigger cell showing the improved ability to find the cathode amplitude for a low electric field detector (935-40AS2). . . . .	100
6.9	(a) Overall depth-corrected single-pixel spectra for cooled operation of detector 935-43AS6 and (b) pixel-by-pixel single-pixel energy resolution. . . . .	100
6.10	Photopeak centroids versus depth for detector 935-43AS6 showing both the low detector trapping (example highlighted in blue) and poor surface charge collection (highlighted in red). . . . .	101
6.11	Overall single-pixel resolution in detector 935-40AS2 for cooled operation under continuous bias showing no significant improvement. . .	102
6.12	Spectrum from detector 935-43AS6 irradiated with both $^{137}\text{Cs}$ and $^{60}\text{Co}$ . Vertical lines indicate the true energy of each gamma-ray line. . . . .	103
6.13	Picture of the benchtop system using the VAD_UM v2.2 digital ASIC. Showing the (a) Faraday cage, (b) Espresso board, and (c) Zedboard. The power supplies and computer are not included. An 11x11 detector is included for scale. . . . .	104
6.14	Block diagram of the benchtop system using the VAD_UM v2.2 digital ASIC. Power supplies and power lines are shown in blue. . . . .	105
6.15	Comparison of the raw performance of detector 935-38AS4 in the (a) v1.2 system compared with the (b) v2.2 system without updated trigger settings. Data taken on subsequent days. . . . .	106
6.16	(a) Raw and (b) depth-corrected spectrum from detector 935-38AS4 showing the return to good performance after optimizing the trigger settings for TlBr. . . . .	107
6.17	Photopeak waveforms from detector 935-38AS4 at 5 MHz showing the ability to use more points for amplitude determination compared with the v1.2 system. . . . .	108
6.18	Picture of the outside of the EspressoUM handheld system. The front is where the detector is mounted and the back has openings for the power and data connectors. . . . .	110
6.19	Inside of the handheld system showing the circuit boards and Faraday cage with the detector inside. . . . .	111
6.20	Diagram of the handheld ASIC system. . . . .	112
6.21	Raw spectrum from detector 935-38AS4 taken with the hand-held system. . . . .	113
7.1	Comparison of new thicker 11x11 array with an older 11x11 array and a 3x3 detector. . . . .	116

7.2	(a) Overall single-pixel spectrum from the thicker detector 125BB1 and (b) the pixel-by-pixel FWHM. The material on the left side shows significantly better energy resolution than on the right. The equivalent of a good 3x3 detector is shown highlighted in green and a bad 3x3 detector is shown in red. . . . .	116
-----	---	-----

## LIST OF TABLES

### Table

1.1	Properties of available photon detector materials . . . . .	5
1.2	Properties of room-temperature semiconductors . . . . .	7
1.3	Comparison of the properties of TlBr and CZT . . . . .	8
3.1	Details of processing methods . . . . .	31
3.2	Mean and median for the distributions shown in Fig. 3.15 . . . . .	41
4.1	Charge collection efficiency fit parameters for detector 935-38AA2L	49
4.2	Ionization energy in detector 935-38AA2L (room temperature . . . .	51
4.3	Ionization energy in detector 935-16B1R ( $-20^{\circ}C$ ) . . . . .	52
4.4	Comparison of theoretical limit of resolution in TlBr and CZT at 662 keV . . . . .	54
4.5	Estimated signal from extra charge on anode and cathode . . . . .	65
4.6	Comparison of estimated and measured cathode signal from extra charge . . . . .	65
4.7	Comparison of estimated hole trapping and anode extra charge . . . .	68
4.8	Performance of TlBr arrays over time . . . . .	69
4.9	Refabricated performance of TlBr detectors . . . . .	73
5.1	Example room-temperature lifetime of TlBr detectors . . . . .	75
6.1	Summary of 11x11 detectors tested with the v1.2 digital ASIC system.	102
6.2	Energy non-linearity in TlBr measured in the v1.2 System . . . . .	103
6.3	Summary of 11x11 detectors tested with the v2.2 digital ASIC system.	108

# ABSTRACT

Advancements in TlBr for Gamma-Ray Detection and Imaging

by

Sean P. O’Neal

Chair: Zhong He

Thallium bromide is an attractive material for room-temperature gamma-ray spectroscopy and imaging because of its high atomic number (Tl: 81, Br: 35), high density ( $7.56 \text{ g/cm}^3$ ), and a wide bandgap (2.68 eV). TlBr detectors can achieve better than 1% FWHM at 662 keV for single-pixel events, but these results are limited to stable operation at  $-20^\circ\text{C}$ . After days to weeks of room-temperature operation, ionic conduction leads to device failure, or polarization. In this work, methods for extending the room-temperature lifetime of these detectors was investigated, and stable operation for greater than 3 months was achieved using special surface processing techniques. Additionally, the effects of intermediate temperature operation (between  $-20^\circ\text{C}$  and room temperature) were investigated and noticeably longer lifetimes were observed with cooling to only  $2^\circ\text{C}$ . This can help reduce the cooling power requirements in field deployable systems if longer term stability at room temperature cannot be achieved.

Important material characterization is also presented including the use of detailed waveform analysis showing that some TlBr detectors have charge multiplication by drifting holes and the measurement of the ionization energy of TlBr. Which when cor-

rected for trapping was shown to be below 5.5 eV. This means the limiting theoretical performance is close to CZT even with TlBr's wider bandgap.

The performance of large volume ( $12 \times 12 \times 5 \text{ mm}^3$ ) TlBr detectors is presented; measured using newly developed digital ASIC based systems. These systems include both benchtop systems which have cooling for the detectors and a prototype handheld system designed for room-temperature operation. 2.2 % FWHM at 662 keV for all single-pixel events was achieved by the best large volume detector. Better performance should be achievable with these systems with improvements in material as more focus is placed on growing and fabricating large volume detectors.

# CHAPTER I

## Introduction

Radiation is a term used to describe subatomic particles emitted from nuclei as a result of either spontaneous decay or an induced reaction. There are many sources of radiation including naturally occurring radioactive materials (NORM) which comprises background, medical isotopes, and potential nuclear weapons material. Identifying and locating sources is important for law enforcement and homeland security, though they are not detectable by the human senses. Radiation is odorless, tasteless, and invisible, so to detect radiation, special sensors called radiation detectors must be developed.

Radiation comes in many forms, requiring varied radiation detectors. Types of radiation include heavy charges particles (including single protons and helium-4 nuclei called  $\alpha$ -particles), high energy electrons, and neutral particles like photons and neutrons. Charged particles slow down in materials by indirect electromagnetic interactions with electrons where neutral particles interact by more direct ways such as scattering. Consequently, charged particles tend to have a shorter range than most neutral particles given equivalent incident energy. Therefore, radiation detectors deployed in searching for radioactive material tend to focus on neutral particle detection, taking advantage of the much higher likelihood that neutral particles escape their source and penetrate into the environment reaching the detector.

## 1.1 Types of Neutral Particles

There are two main types of neutral particles which comprise radiation: photons and neutrons. Using neutrons to detect radioactive material benefits from a much lower natural background, but they are only emitted by certain (though important) materials. Additionally, neutrons emitted by most common sources (U and Pu) originate from fission and consequently have similar energy distributions making source identification difficult.

Fast neutrons from fission interact primarily by elastic scattering and induce the most signal on light nuclei. As a result, the materials which offer the highest detection probability are organic materials and plastics and detectors utilizing these materials are relatively large, low density detectors [1]. Some excellent work has been done on fast neutron detectors capable of identifying and localizing special nuclear material by multiple researchers including Goldsmith [2] and others [3],[4], but these systems are large and cumbersome. Detectors for thermal neutrons offer very high stopping power, but provide little information about the source. They are not able to distinguish between neutrons from fission and those from natural sources such as cosmic rays.

Photons, on the other hand, are emitted by nearly all radioactive materials whether from nuclear transitions (gamma rays) or from electron transitions (X-rays). Furthermore, because energy levels are quantized, the energies of photons from a source are discrete and knowledge of their energy can be used to infer the material which emitted them. This work focuses on photon detection for these reasons.

## 1.2 The Ideal Photon Detector

The ideal photon detector has very high sensitivity achieving both a high detection efficiency (a high chance of stopping an incident photon) and good identification through background rejection. Additionally, it should be cost effective for mass de-

ployment, reliable, and robust for a wide range of operating conditions that can be encountered in the field.

### **1.2.1 Detection Efficiency**

High detection efficiency can be achieved in two ways: large detector volume and high intrinsic efficiency. That is both a high likelihood that a photon will cross the detector (large area) and a high probability of it interacting when it crosses the detector. In general, photons interact with electrons in the detector material[1], so high electron density is desirable. This can be achieved by both high material density and high atomic number (or large number of electrons per atom).

### **1.2.2 Source Identification**

Good source identification is also achieved through a combination of factors. The most important factor is the ability to accurately measure the incident photon energy. The energy discrimination ability of a detector is quantified by its energy resolution which is generally reported as the full width at half maximum (FWHM) of the full energy peak at a particular incident energy. A lower FWHM represents both the ability to distinguish between two gamma rays closer in energy and lower uncertainty in the estimation of the energy of a single gamma ray line.

Additionally, better energy resolution allows for better background rejection in the detector. A detector with no energy discrimination integrates all background events in with source counts. When a narrow spectral region of interest (ROI) around a full energy signal can be identified, however, background counts outside of this region can be ignored while preserving all the full-energy deposition source counts. This improves the signal to noise ratio (SNR) of the calculated source intensity. The better the energy resolution, the narrower the ROI can be, and therefore the more background can be rejected.



Just as energy resolution can separate background counts out in energy domain, the use of imaging can discriminate background counts in physical space. If the detector can determine the direction a photon comes from, and the source can be localized, then counts from non-source directions can be rejected decreasing background. In practice, imaging also reduces the observed signal as well, but can be used to still improve the SNR in some applications [5].

Beyond improving detection sensitivity, imaging is also beneficial in search applications such that users can find out where a source is spatially in addition to the information that it exists and its identity (from its energy).

### **1.2.3 Engineering Concerns**

The deployability, cost, and reliability of photon detectors are also important for real world applications. Ideally, the detector should be cheap to produce allowing for more total deployed volume, increasing the total sensitivity. It should be fieldable, meaning it should be easily transported and be able to be set up quickly. Finally, it should be reliable, offering stable performance over a wide range of situations including different environments (ranging from deserts to rainforests) and be robust against storage, power cycling, shipping and other practical concerns.

## **1.3 Currently Available Technologies**

Table 1.1 shows some examples of common and currently available photon detector materials and summarizes their strengths and weaknesses against the ideal photon detector. Broadly speaking, there are two classes of detectors: scintillators which convert incident gamma rays to visible light, and semiconductors which directly measure ionization produced by incident photons.

Scintillators tend to be less costly, but offer worse energy discrimination and higher temperature drift due to their photosensors. Scintillators also tend to have worse

Table 1.1: Properties of available photon detector materials

Material	Detector Type	Density [g/cm <sup>3</sup> ]	Effective Z	Energy Res- olution at 662 keV	Imaging	Cost	Stability
Ideal		High	High	Very Good	Great	Low	High
Plastics	Scintillator	~1	~ 5	None	None	Inexpensive	Moderate
NaI	Scintillator	3.67	51	7-9 % [1]	Sometimes - Poor	Low	Strong Tempera- ture Drift
LaBr <sub>3</sub>	Scintillator	5.06	44	3 % [6]	Sometimes	Moderate	Strong Tempera- ture Drift
HPGe	Semiconductor	5.3	32	0.2% [7]	Sometimes	Very High	Requires Cryo- genic Cooling
CZT	Semiconductor	6.1	50	0.35% - 1.0% [8]	Most	Very High	Some (correctable) Temperature Drift

imaging performance due to poorer position and energy resolution. Semiconductors tend to have much better energy resolution, but often have much lower detector volume and are much more costly.

In most commercial systems, NaI is widely used due to its availability in large sizes and its moderate performance at a reasonable price point [1]. High-purity Germanium (HPGe) is the gold standard for energy resolution. However, it suffers in field uses due to its need for cryogenic cooling (operating at 77K) because of its narrow band gap (0.7 eV). HPGe detectors either require regular replenishing with liquid nitrogen or large, heavy, mechanical cooling systems which often need hours to cool the detector down before they can be used [9].

Recent developments have brought exciting new materials to the market including high performance scintillators such as LaBr<sub>3</sub> [6] and SrI<sub>2</sub> [10] which improve on the energy resolution of NaI at a cheaper price than semiconductors. These materials are still more expensive (and smaller) than commercially available NaI, but are promising alternatives in some applications. These high performance scintillators are still limited in many applications though, because they cannot achieve competitive energy discrimination with HPGe.

### 1.3.1 Room Temperature Semiconductors

Significant work has been done in seeking alternative semiconductors to HPGe with wider band gaps to allow for room-temperature operation. This has led to the development of many materials including GaAs, CdTe, CdZnTe (CZT), and HgI<sub>2</sub>. Table 1.2 summarizes the properties of these materials.

GaAs and CdTe were among the first room-temperature materials studied with GaAs being the first material to demonstrate good gamma-ray energy resolution at room temperature [11]. However these results were with epitaxial grown material which is very expensive, and the development of cheaper bulk-grown GaAs mate-

Table 1.2: Properties of room-temperature semiconductors

Material	Density [g/cm <sup>3</sup> ]	Effective Z	Band Gap [eV]
GaAs	5.3	32	1.43
CdTe	6.2	50	1.44
CZT	6	50	1.64
HgI <sub>2</sub>	6.4	66	2.13

rial has not been very successful [12]. CdTe offers a higher stopping power due to its higher atomic number, but still only has a moderate band gap requiring some cooling for thick detectors [1]. By adding some zinc to CdTe, the band gap can be widened allowing true room-temperature operation for even very thick (up to 15 mm) detectors.

The initial development of CZT was challenging due to it being a ternary compound. Large-volume CZT boules have suffered from numerous defects especially non-uniformity due to Te rich regions called inclusions [13]. However, advances in material growth process [14] and read out methods [15, 16] have improved the performance of CZT detectors significantly. CZT now offers energy resolutions competitive with HPGe in the field and good imaging performance from even a single detector [17, 18]. This is shown in Table 1.1.

Currently, pixelated CZT scores as one of the best materials offering good reliability, energy resolution competitive with HPGe, and quickly reducing cost as production increases. The Polaris-H pixelated CZT handheld detector is now used by over half of US nuclear power plants [19].

Even higher Z and wider band gap materials than CZT are available. HgI<sub>2</sub> has been studied and has shown good energy resolution and higher stopping power than CZT [20, 21]. However, these devices suffer from a range of issues including space charge polarization and a conditioning period where the detector requires bias for multiple days before showing good performance [1].

Table 1.3: Comparison of the properties of TlBr and CZT

Material	Density [g/cm <sup>3</sup> ]	Effective Z	Band Gap [eV]	Best Resolution [% FWHM at 662 keV]
CZT	6	50	1.64	0.5%
TlBr	7.56	69	2.68	1.0%

## 1.4 TlBr

Thallium-bromide (TlBr), the major focus of this work, is a room-temperature semiconductor and an exciting alternative option to CZT. Table 1.3 shows a comparison of the properties of TlBr to CZT.

TlBr has a higher stopping power (or intrinsic efficiency) due to its higher atomic number and density. TlBr has a wider bandgap and thus should have a lower leakage current at the same temperature, allowing it to operate at higher temperatures than CZT. Also, TlBr is capable of using the same methods for imaging as CZT. The charge clouds in TlBr should be smaller than in CZT due to its high electron density, leading to better depth-correction at high energy.

For cost, TlBr is an easier material to grow than CZT. It is binary instead of ternary and has a simple cubic structure with a single solid phase between room temperature and its melting point. This allows for simple melt based growth processes to be used (see Section 3.1.1 for more on growth) [22, 23]. The simplicity of TlBr growth should mean that at a similar developmental states, TlBr should be cheaper than CZT.

### 1.4.1 Challenges - Polarization

TlBr has its own challenges. It is an ionic material, so under bias lattice constituents can drift causing damage to the detector [24]. This process is called as polarization and can ruin a detector after only days to weeks of operation at room temperature [25]. Fig 1.1 shows the degrading energy spectra versus time for a TlBr

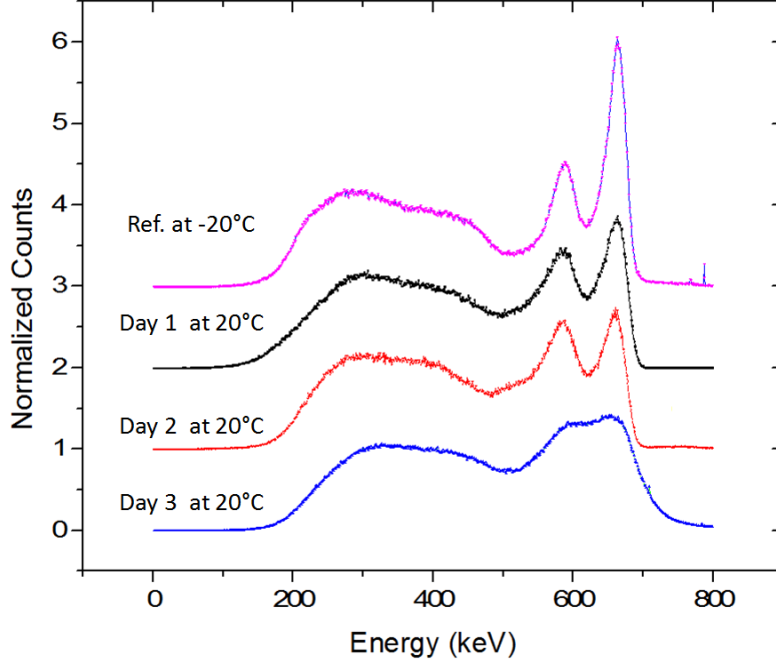


Figure 1.1: Spectra at  $-20^{\circ}\text{C}$  and three days at room temperature of detector 44AB1R showing the degrading performance due to polarization. Spectra are shifted vertically for clarity.

detector at room temperature demonstrating polarization. Fig. 1.2 shows a comparison of the anode from a polarized detector and a regular TlBr detector. Koehler demonstrated it was this contact degradation that causes the detectors to stop working, leading to focused efforts on surface treatments to mitigate the effects of polarization [25].

#### 1.4.2 Challenges - Conditioning

Donmez [26] demonstrated that by cooling the detectors to  $-20^{\circ}\text{C}$  the effects of polarization could be effectively stopped. Though it is desirable to have true room-temperature operation, cooling to  $-20^{\circ}\text{C}$  is better than requiring cryogenic cooling (such as in HPGe) and allows for more reproducible material study in TlBr.

However, the performance of TlBr with time is not stable at  $-20^{\circ}\text{C}$ . Generally, the resolution improves with time over the first few days, a process called conditioning. This is demonstrated from an example detector in Fig. 1.3. Koehler [27] demonstrated

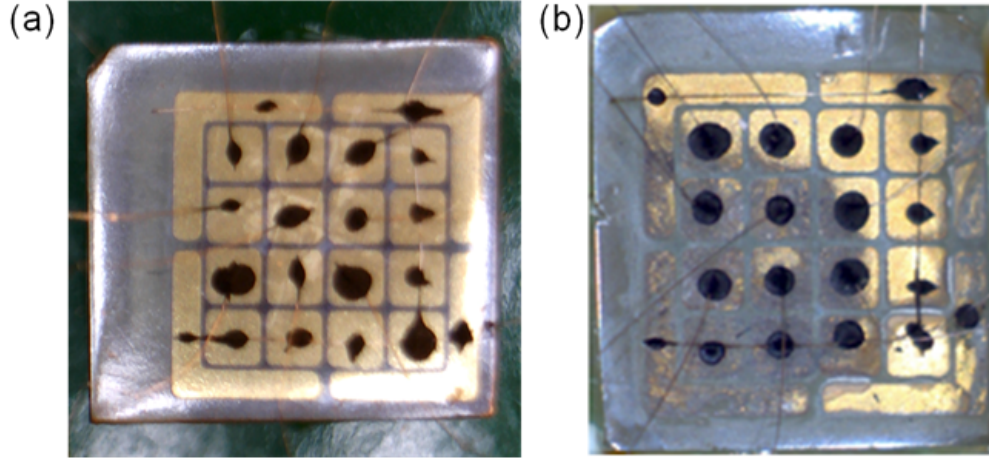


Figure 1.2: Picture of the anode electrode from an (a) normal and (b) polarized TlBr detector showing how room-temperature operation has degraded the contact surface.

this process was due to the drift of charged impurities out of the detector, leading to a more uniform electric field and better charge collection.

#### 1.4.3 Challenges - Non-Uniformity

TlBr also suffers from material inhomogeneity. Fig. 1.4 shows the energy spectrum from a good TlBr detector where the overall energy resolution is 1.06% FWHM at 662 keV with Fig. 1.5 showing this spectrum broken up by its constituent pixels. The best pixel shows a performance of 0.8% FWHM where the worst shows about 3% and this variation is over only a few millimeters of material.

Energy resolution also varies highly sample to sample. The best detectors can achieve better than 1% FWHM at 662 keV while an average detector ranges from  $\sim 1\%$  - 2.5% FWHM. CZT can reliably achieve around 0.6% FWHM at 662 keV.

### 1.5 State of the Art in TlBr

Significant work has been done in understanding TlBr and addressing its challenges. As mentioned previously, Koehler and Donmez's work has been pivotal in understanding the conditioning and polarization of TlBr detectors. In particular,

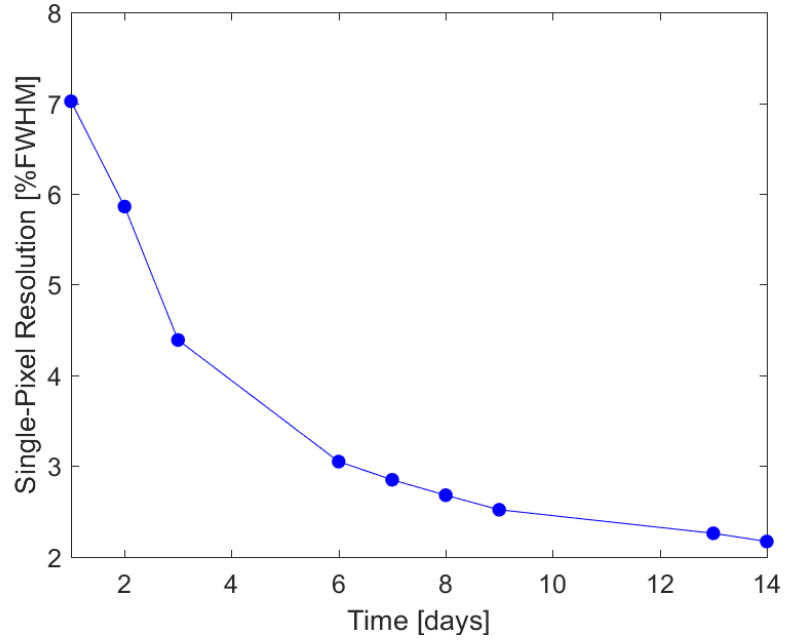


Figure 1.3: Energy resolution versus time for detector 44B2L at  $-20^{\circ}\text{C}$  showing improvement over the first few days referred to as conditioning.

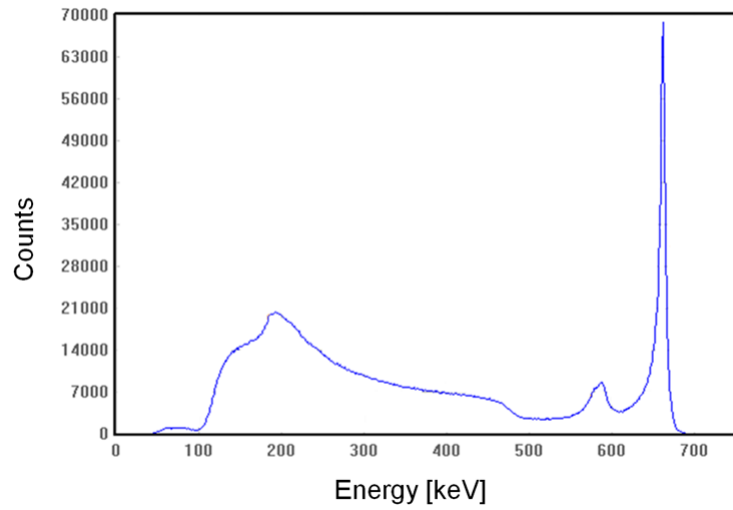


Figure 1.4: Example TlBr  $^{137}\text{Cs}$  spectrum from a  $5\times 5\times 5\text{ mm}^3$  TlBr detector showing performance of 1% FWHM



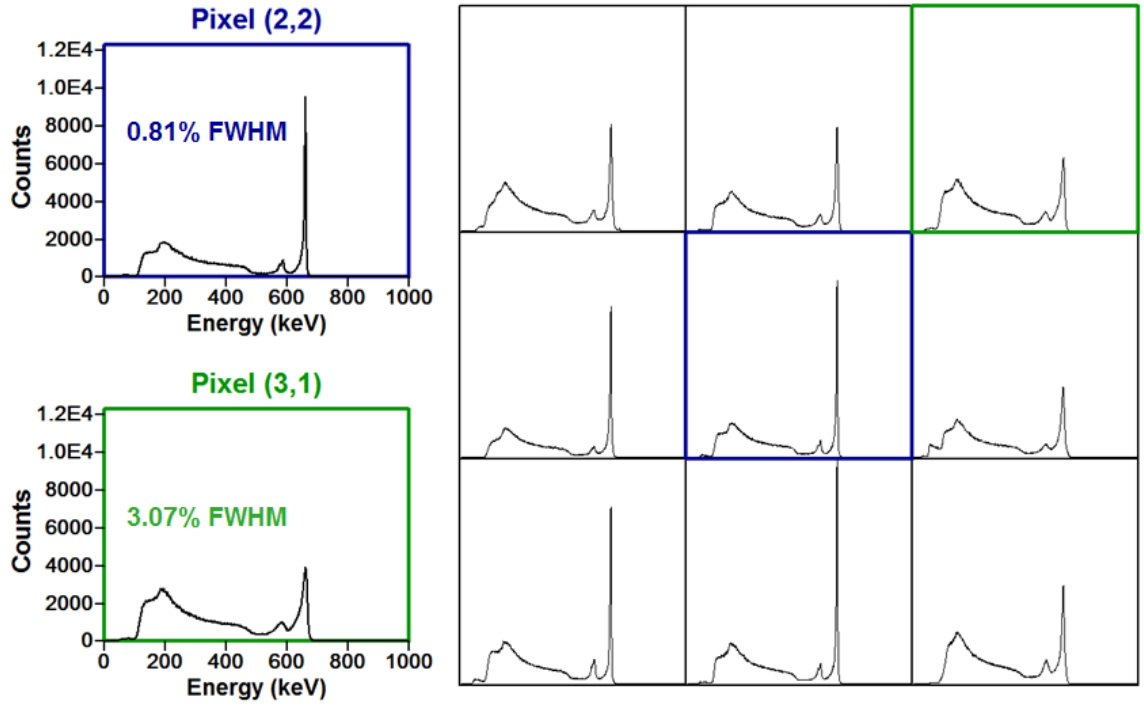


Figure 1.5: Pixel-by-pixel breakdown of the spectrum from Fig. 1.4, with the best and worst pixel highlighted. The best pixel (blue) shows a resolution of 0.81% FWHM where the worst pixel (green) shows a resolution of 3.07% FWHM.

Koehler demonstrated that refabrication of polarized detectors could return them to good performance [25].

Hitomi, et al. demonstrated that the polarization can be mitigated using Tl electrodes and periodically reversing the bias [28, 29]. This prevents foreign elements from contacts getting into the crystal which normally causes device failure. Hitomi has also demonstrated good performance from TlBr detectors using a wide range of electrode configurations including pixelated, Frisch grid, and cross-strip geometries [30, 31].

Conway, et al. at Lawrence Livermore National Laboratory (LLNL), demonstrated that different surface etches and contact materials affect the polarization rate in planar detectors [32]. Specifically, they proposed using an HCl etch to create a surface layer of TlCl, which has a wider bandgap than TlBr, and should therefore create an energy barrier preventing the contact material from entering the detector. They also refined their processing technique to prevent precipitation of Tl on the surface (called “dendrites”) which provided another mode of device failure.

## **1.6 Contributions of This Work**

This work expands the state of the art in TlBr in both material characterization and the engineering deployment of the technology. Section 3.4 includes a preamplifier decay correction algorithm which is valid for all digital waveforms. Chapter IV discusses material characterization including new methodologies for analyzing pulse waveforms and establishes that drifting holes can free excess electrons in some TlBr detectors. Chapter V discusses methods for extending the lifetime of TlBr detectors including validation of LLNL results on thicker pixelated detectors and investigation into the effects of temperature on the polarization rate. Finally, Chapter VI discusses the development of ASIC based system which allow for the use of larger TlBr arrays and demonstrates the first prototype handheld TlBr detector system.

## CHAPTER II

### Theory

When a gamma ray interacts in a semiconductor, it typically creates a high energy electron which subsequently slows down exciting a large number of electron-hole pairs. The number of electron-hole pairs is proportional to the original electron energy. The conversion rate of electron energy to number of electron-hole pairs is described by the ionization energy,  $w$  [1]

$$N = \frac{E}{w}, \quad (2.1)$$

where  $N$  is the number of electron-hole pairs created and  $E$  is the electron energy.

#### 2.1 The Energy Spectrum

The signal induced from these  $N$  electron-hole pairs is recorded and histogrammed creating a spectrum. Fig. 2.1 shows an example TlBr spectrum with significant features highlighted.

The full-energy peak (or photopeak) corresponds to gamma rays that deposit all their energy in the detector. The photopeak is primarily comprised of gamma rays that undergo the photoelectric effect. In the photoelectric effect, gamma rays are fully stopped by knocking out an inner shell electron from an atom in the detector. This

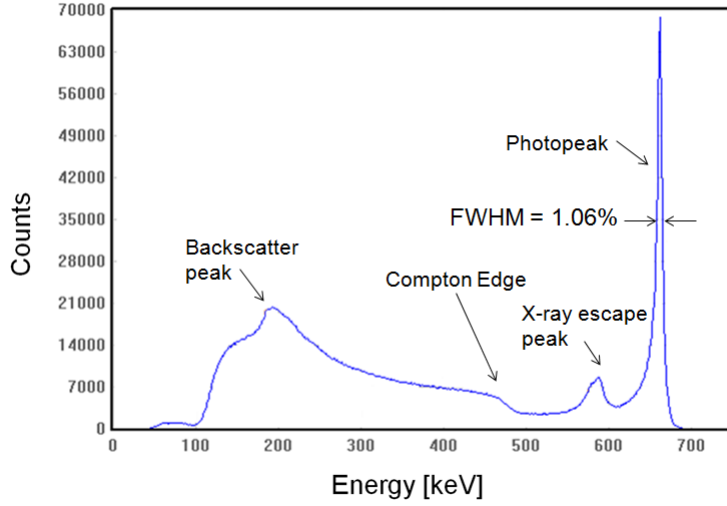


Figure 2.1: Example TlBr spectrum with the key features labeled.

gives the electron energy equal to the photon energy less the electron binding energy. The empty location in the atom's inner shell is then filled by another electron, which emits an X-ray in the transition with energy equal to the electron binding energy. This X-ray is usually absorbed, resulting in a peak with energy equal to the incident gamma ray.

If the X-ray escapes the detector (or the collecting pixel in pixelated detectors) before being absorbed it will contribute to a peak at slightly lower energy, the X-ray escape peak. This escape peak usually only occurs for small samples, but because the TlBr X-ray energy is high (70-80 keV) and TlBr is a binary semiconductor, it escapes the pixel a non-trivial percentage of the time.

Full-energy depositions are the most important events for source identification and the likelihood of photoelectric absorption is a strong function of the atomic number ( $Z$ ) of the detector. The cross section is roughly proportional to  $Z^4$  and this accounts for the very high photopeak efficiency in TlBr due to Tl's very high  $Z$  (81) versus other detector materials ( $Z_{Ge} = 32$ ) [1]. Fig. 2.2 shows the photopeak interaction probability in a 5mm thick TlBr detector compared with the same sized CZT. At moderate gamma energies, TlBr has greater than three times the photoelectric

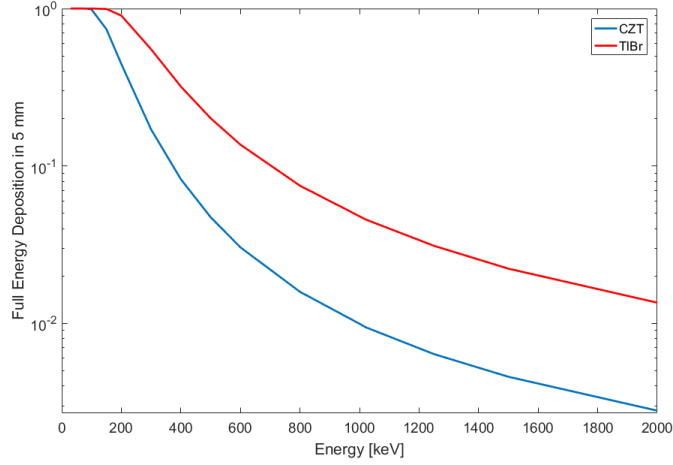


Figure 2.2: Comparison of the photopeak interaction probability between TlBr and CZT in a 5mm thick detector using the data from NIST. [33]

interaction probability.

The other primary way gamma rays interact in TlBr is by Compton scattering. Here the gamma ray scatters off an electron depositing some, but not all, of its energy. The energy deposited is a function of the scattering angle,  $\theta$ , between the gamma ray's initial direction and its scattered direction. Eq. 2.2 shows this relationship [1].

$$E_{electron} = E_{\gamma_0} - E'_{\gamma} = E_{\gamma_0} - \frac{E_{\gamma_0} m_e c^2}{E_{\gamma_0} [1 - \cos(\theta)] + m_e c^2} \quad (2.2)$$

This results in a continuum of deposited energies between zero and a maximum called the Compton Edge.

The final feature labeled in Fig. 2.1 is the backscatter peak. This corresponds to gamma rays which have Compton scattered in the environment and then enter the detector. Since at high scattering angles (close to  $180^\circ$ ) the scattered energy is a weak function of angle, gamma rays which scatter at these angles either in the source, environment, or detector housing contribute roughly the same energy forming this peak.

## 2.2 Energy Resolution

The photopeak width is called the energy resolution. This is because a narrower peak allows for separation (or resolving) of gamma-ray peaks which fall closer in energy. The energy resolution is quoted as the full width at half maximum (FWHM) divided by the energy, or

$$R = \frac{FWHM}{E}. \quad (2.3)$$

The FWHM can be calculated geometrically, or as

$$FWHM = 2.35\sqrt{F}\sigma \quad (2.4)$$

for a Gaussian shaped peak. Where  $F$  is the Fano Factor which describes correlation in the ionization process and  $\sigma$  is the standard deviation of the Gaussian peak.

### 2.2.1 Fundamental Limit

Fundamentally, not all events will create the same number of electron-hole pairs for the same incident energy. The natural variance in the number of electron-hole pairs is due to counting statistics and determines the theoretical limiting performance of the detector [1]. The ionization process can be described as a Poission process [1] so the variance is equal to the mean, therefore

$$R_{limit} = 2.35\sqrt{F}\frac{\sigma_{CS}}{N} = 2.35\frac{\sqrt{FN}}{N} = 2.35\sqrt{\frac{F}{N}} = 2.35\sqrt{wF/E}. \quad (2.5)$$

For HPGe,  $w = 2.96$  eV [34] and  $F \approx 0.11$  [35], so the limiting performance at 1332 keV is 0.116%. In practice, HPGe detectors can achieve  $\sim 0.135\%$  at 1332 keV due to non-ideal factors [36].

### 2.2.2 Degradation of Energy Resolution

Three major factors affect the ability to reliably measure the number of generated electron-hole pairs which consequently degrades the energy resolution: electronic noise, trapping, and detector non-uniformity.

#### Electronic Noise

Electronic noise represents uncertainty in the estimation of the number of electron-hole pairs and is an additive feature in degrading energy resolution. The magnitude of the electronic noise is roughly constant with energy, so the peak width,  $\sigma_{tot}$  becomes

$$\sigma_{tot}^2 = \sigma_{CS}^2 + \sigma_{Noise}^2 = F \frac{w}{E} + \sigma_{Noise}^2 \quad (2.6)$$

where  $\sigma_{Noise}^2$  is the variance from electronic noise and  $\sigma_{CS}^2$  is the variance from counting statistics.

#### Trapping

Trapping is the process by which the number of measured carriers will be less than the number initially created due to absorption of electrons or holes by impurities during their drift through the detector. Trapping depends both on the number of initial carriers and the carrier drift distance. This can greatly degrade performance when drift distances are comparable to mean trapping lengths.

#### Inhomogeneity

Inhomogeneity is where variation across the detector causes the measured signal to be different at different locations. This can be from different amounts of trapping, from different leakage currents (which contribute to noise) or from variation in the ionization energy across the detector. The effects of inhomogeneity can be corrected

in some cases when the location of the interaction is known. However, non-uniformity on very small scales (such as the size of the electron cloud) cannot be corrected for and limit the performance of non-homogeneous materials.

## 2.3 The Shockley-Ramo Theorem

The Shockley-Ramo theorem states that the signal induced in semiconductor detectors from radiation interactions is due to the drifting of charge in the detector, not the collection of the charge [37]. Equation 2.7 states the Shockley-Ramo theorem mathematically. The induced charge,  $Q_{induced}$ , is proportional to the drifting charge,  $q_{drifting}$ , times the change in the weighting potential,  $\psi_0$ , along the carrier drift,

$$Q_{induced} = -q_{drifting} \times \Delta\psi_0. \quad (2.7)$$

The weighting potential is the solution to the Poisson equation ignoring space charge in the detector and applying special boundary conditions [37]. The potential on the collecting electrode is set to unity and the potential on all other electrodes is set to zero,

$$\nabla^2\psi_0 = 0, \quad \begin{pmatrix} \psi_0(\text{collecting electrode}) = 1 \\ \psi_0(\text{all other electrodes}) = 0 \end{pmatrix}. \quad (2.8)$$

If all electrons drift to the anode and all holes to the cathode, then the Shockley-Ramo theorem predicts that the induced charge will be equal to the drifting charge. This is demonstrated in Eqs. 2.9 - 2.12.

$$Q_{induced} = Q_e + Q_h = \quad (2.9)$$

$$Q_e = -q_e[1 - \psi(z_0)] \quad (2.10)$$

$$Q_h = -q_h[0 - \psi(z_0)] = -q_h\psi(z_0) = q_e\psi(z_0) \quad (2.11)$$

$$Q_{induced} = -q_e[1 - \psi(z_0) + \psi(z_0)] = -q_e \quad (2.12)$$



In traditional semiconductor materials (HPGe and Si), the lifetime of electrons and holes are sufficiently large that almost all charge is collected and any electrode geometry can be used. For simplicity, planar electrodes or a coaxial geometry is often used requiring only two electrodes. However, with room-temperature semiconductors, the mobility of holes is often more than an order of magnitude worse than the mobility of electrons, causing complete charge collection to be impossible. Therefore alternative charge collection techniques are required to achieve good energy resolution.

### 2.3.1 Integral form of the Shockley-Ramo Theorem

Eq. 2.7 can be written in a differential form, such that the small amount of induced charge,  $dQ$ , from the short drift distance  $dx$ , can be expressed as

$$dQ_{induced} = -q_{drifting} \times [\psi_0(x + dx) - \psi_0(x)]. \quad (2.13)$$

This exactly mirrors the definition of the derivative of a function  $f$ , or,

$$\frac{df}{dx} = \frac{f(x + dx) - f(x)}{dx}. \quad (2.14)$$

Therefore the change in the weighting potential in Eq. 2.13 can be replaced with the derivative of the weighting potential, or,

$$dQ_{induced} = -q_{drifting} \times \psi'_0(x)dx. \quad (2.15)$$

Using Eq. 2.15, the amount of drifting charge does not have to stay constant, but can be allowed to vary over the drift from effects such as trapping. Finally integrating Eq. 2.15, the total induced charge can be expressed as

$$Q_{induced} = \int_{x_0}^{x_f} -q_{drifting}(x') \times \psi'_0(x')dx'. \quad (2.16)$$

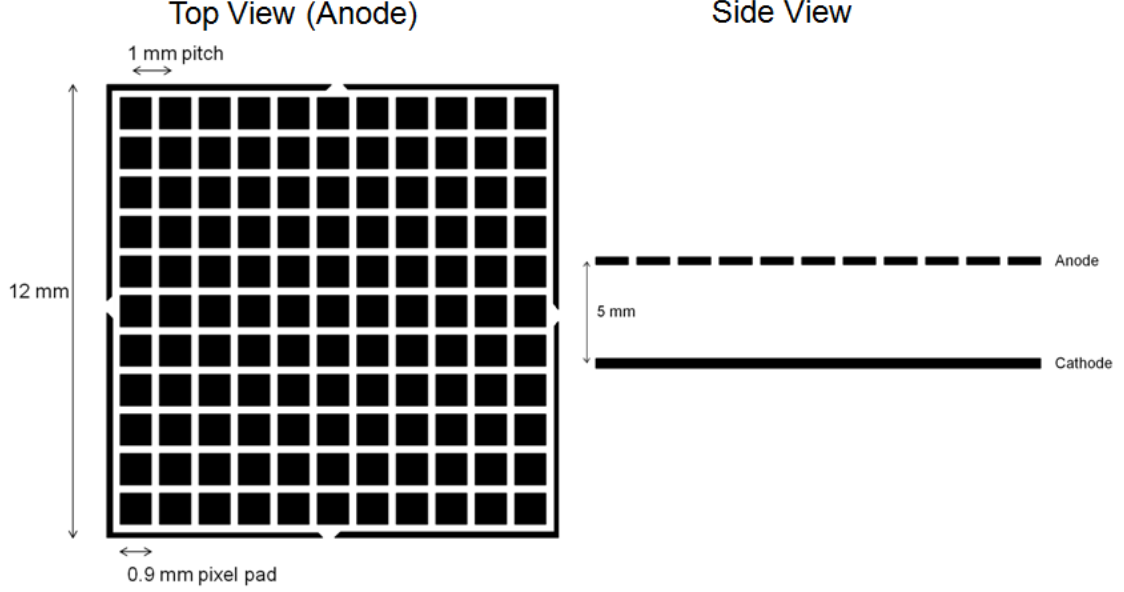


Figure 2.3: Geometry of 11x11 pixelated electrodes. Each pixel pad is  $0.9 \times 0.9 \text{ mm}^2$  with a  $100 \text{ }\mu\text{m}$  gap between pixels. The cathode is planar and the detector is 5 mm thick.

### 2.3.2 Single-Polarity Charge Sensing

Single-polarity charge sensing is a technique where the electrode geometry is carefully chosen such that the drift of only one carrier (generally electrons) is required so that the induced charge is a good estimate the charge generated by the gamma ray[38]. From Eq. 2.10, this implies that the weighting potential should be near zero for most of the detector volume. This can be achieved in a number of ways including a co-planar grid, virtual Frisch grid, or pixelated electrodes [37]. In this work, a pixelated anode is used to achieve the near zero bulk weighting potential.

Two anode configurations are used in this work: a 3x3 and an 11x11 pixelated anode. With both, the pixel pitch is 1 mm with a  $0.9 \times 0.9 \text{ mm}^2$  pixel area and a  $100 \text{ }\mu\text{m}$  gap between pixels. Both configurations have a guard ring surrounding the pixels and a planar cathode. Fig. 2.3 shows the 11x11 pixelated electrodes with Fig. 2.4 showing the resulting weighting potential for both the (a) anode and (b) cathode.

As shown in Fig. 2.4, the pixelated (collecting) anode weighting potential is near

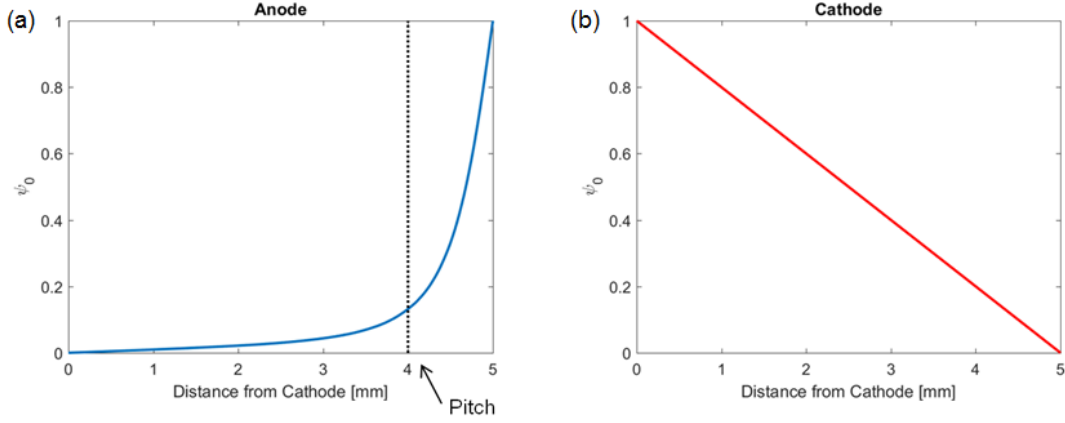


Figure 2.4: Weighting potential for the (a) anode (blue) and (b) cathode (red) for the electrode geometry shown in Fig. 2.3.

zero for most of the detector volume and then rises quickly to unity at approximately one pixel pitch from the anode. However, it is not actually zero throughout the bulk. The slight rise in the bulk depends on the pixel pitch to thickness ratio and decreases as this ratio decreases. This non-ideal part of the weighting potential gives rise to the need for a correction factor when calculating the  $\mu\tau$ -product as discussed in Section 2.4. The cathode weighting potential is simply linear, so the signal induced on the cathode will be proportional to both the number of charges and the depth of interaction.

### 2.3.3 3D Correction

Using pixelated electrodes, the 3D position of each gamma ray interaction can be localized and the effects of electron trapping and non-ideal weighting potential can be corrected [15]. The signal induced after complete collection on the pixelated anode is approximately equal to the drifting charge, where the signal on the planar cathode is proportional to both the drifting charge and the normalized depth of interaction,  $z_n$ . Therefore the depth of interaction can be calculated by taking the cathode-to-anode

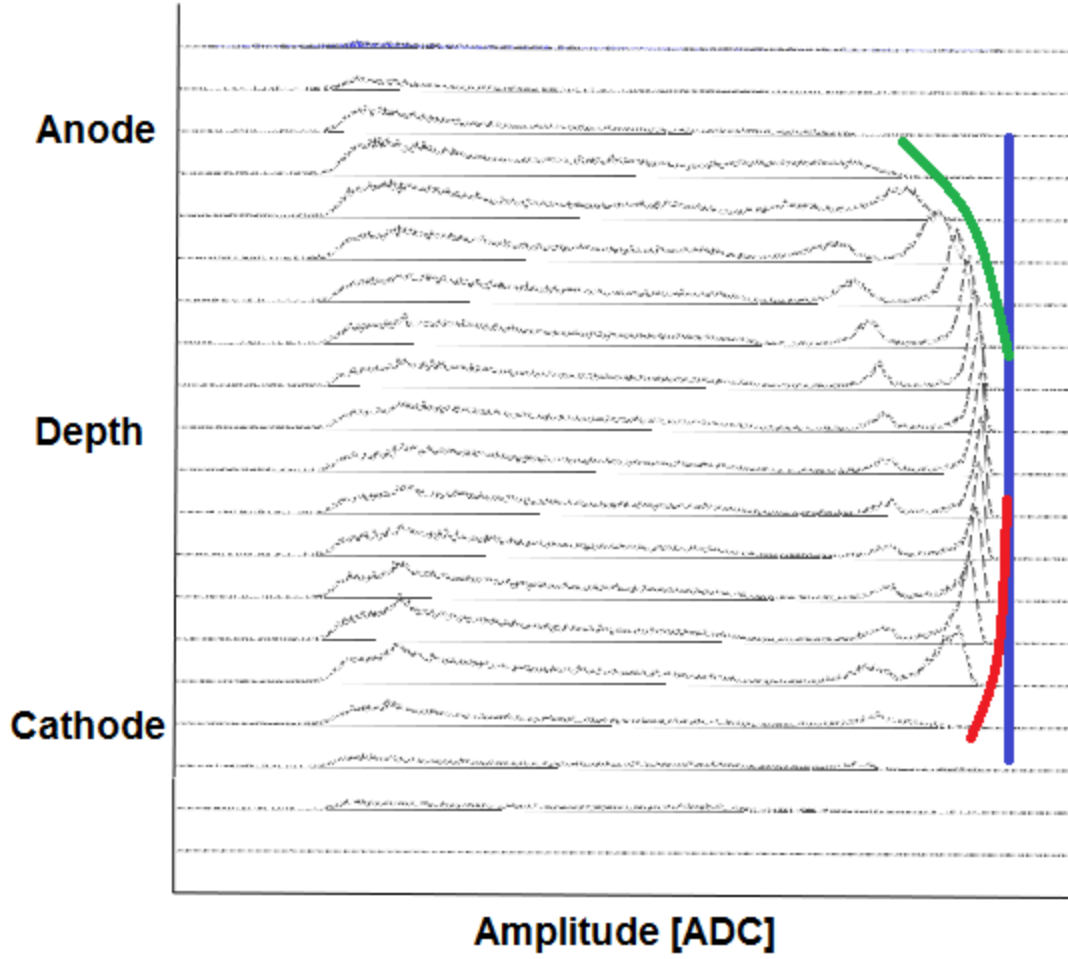


Figure 2.5: Depth separated spectrum for one pixel. The photopeak amplitude decreases towards the anode side (green) due to the non-ideal weighting potential and towards the cathode side (red) due to trapping.

ratio (CAR) [39]. This is demonstrated in Eqs. 2.17 - 2.19.

$$Q_{anode} = q_{drifting} \times [1 - \psi_{anode}(z)] \approx q_{drifting} \times [1 - \delta(z)] = q_{drifting} \quad (2.17)$$

$$Q_{cathode} = q_{drifting} \times [\psi_{cathode}(z) - 0] = q_{drifting} \times [z_n - 0] = z_n q_{drifting} \quad (2.18)$$

$$CAR = \frac{Q_{cathode}}{Q_{anode}} = \frac{z_n q_{drifting}}{q_{drifting}} = z_n \quad (2.19)$$

Using depth determined from the CAR, the spectrum for each pixel can be broken up into different depths. Fig. 2.5 demonstrates this for a  $^{137}\text{Cs}$  source in TlBr.

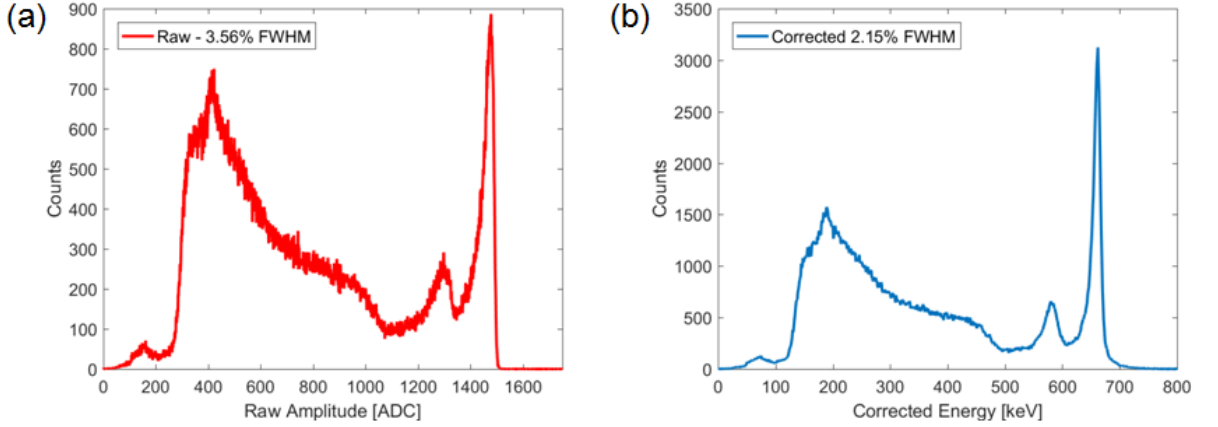


Figure 2.6: Example of depth correction on the data shown in Fig. 2.5, (a) shows the raw spectrum at 3.56% FWHM and (b) the depth-corrected spectrum at 2.15% FWHM.

The amplitude of the photopeak decreases towards the cathode side due to trapping of electrons in the material and decreases towards the anode side due to the non-ideal weighting potential. Since the incident energy (662 keV) is the same for all photopeak events, the centroids of each peak can be aligned, correcting for trapping and weighting potential effects in the detector. This calibration is done for each depth bin (15 bins in 5 mm) and for each pixel, resulting in a 3D trapping correction. Fig. 2.6 show a comparison of the raw pixel spectrum and the 3D corrected spectrum showing the improvement from a raw resolution of 3.6% FWHM to 2.2% FWHM when the effects of trapping and weighting potential variation are corrected.

## 2.4 $\mu\tau$ -Product

The amount of carrier trapping in a detector is determined by the mobility-lifetime (or  $\mu\tau$ ) product [40]. The lifetime is the mean time that a carrier can drift before it is trapped. The number of un-trapped carriers with time can be expressed in terms of the lifetime as,

$$N(t) = N_0 e^{-t/\tau} \quad (2.20)$$

where  $N_0$  is the initial number of carriers and  $\tau$  is the mean carrier lifetime.

The mobility is defined as the ratio between carrier velocity ( $v$ ) and the electric field ( $E$ ), or

$$\mu = \frac{v}{E}. \quad (2.21)$$

A higher mobility implies that the charges drift faster for the same electric field, leading to a faster collection time and consequently less trapping. Combining Eq. 2.21 and 2.20, the number of carriers along a drift from  $x_0$  to  $x$  can be expressed as,

$$N(x) = N_0 e^{\frac{-(x-x_0)}{\mu\tau E}}. \quad (2.22)$$

The charge collection efficiency ( $CCE$ ) is the ratio of the collected charges to the original charges, or

$$CCE = \frac{N(x)}{N_0} = e^{\frac{-(x-x_0)}{\mu\tau E}}. \quad (2.23)$$

For an event where the charges drift through the entire detector thickness,  $d$ , Eq. 2.23 can be simplified as

$$CCE = e^{\frac{-d}{\mu\tau E}}. \quad (2.24)$$

The  $\mu\tau$ -product defines material quality. As shown in Eq. 2.24 a combination of the operating electric field and the  $\mu\tau$ -product determines the mean trapping length and thus the maximum thickness of the detector.

While the 3D correction can correct for the mean value of trapping, it cannot account for increased variance introduced by trapping or non-homogeneous trapping especially on scales smaller than the electron cloud, so a high  $\mu\tau$ -product is desirable.

### 2.4.1 Two-bias Method

There are multiple ways to measure the  $\mu\tau$ -product of a detector. For single-polarity charge sensing detectors, the two-bias method is often used [40]. In the two-bias method, the amplitude of the full energy peak (cathode side in pixelated detectors) is compared at two different biases. Mathematically, this involves solving Eq. 2.22 for two different biases, and setting  $N_0$  to be the same in both cases. Solving for the  $\mu\tau$ -product results in

$$\mu\tau = \frac{d^2}{\ln(N_1/N_2)} \left( \frac{1}{V_2} - \frac{1}{V_1} \right), \quad (2.25)$$

where  $t$  is the detector thickness and  $N_1$  and  $N_2$  are cathode-side amplitudes at biases  $V_1$  and  $V_2$  respectively. It should be noted that Eq. 2.25 assumes a uniform electric field and a perfect weighting potential.

The assumption of a perfect weighting potential works well for coplanar grid detectors. However, for pixelated detectors which have non-ideal weighting potentials, Koehler et. al demonstrated that the two-bias method can over estimate the  $\mu\tau$ -product by as much as 20% based on detector geometry [41]. Koehler developed a correction factor to account for this over estimation.

The correction factor,  $k$ , is a function of the pitch to detector thickness ratio ( $PDR$ ). The updated two-bias method for pixelated detectors is shown in Eq. 2.26 with Eq. 2.27 showing the empirically determined correction factor.

$$\mu\tau = k \frac{d^2}{\ln(N_1/N_2)} \left( \frac{1}{V_2} - \frac{1}{V_1} \right) \quad (2.26)$$

$$k = -0.459 \times PDR + 0.993 \quad (2.27)$$

### 2.4.2 Hecht-Fitting

The Hecht-relation can also be used to determine  $\mu\tau$ -products [42]. Hecht fitting uses more than two biases and fits the measured amplitude as a function of the detector bias. Eq. 2.28 shows the classic Hecht relation which is valid only for planar detectors,

$$N_{planar} = N_0 \frac{\mu\tau V}{d^2} \left[ 1 - e^{-\frac{d^2}{\mu\tau V}} \right]. \quad (2.28)$$

Eq. 2.28 is the solution to Eq. 2.16 using the trapping model from Eq. 2.22 and a linear weighting potential. For ideal pixelated detectors the same process can be applied using the pixelated weighting potential. This results in the modified Hecht-relation for ideal pixelated detectors given in Eq. 2.31

$$N_{pixel} = \int_0^d -N_0 e^{\frac{-x}{\mu\tau E}} \times \psi'_{0,pixel}(x') dx' \quad (2.29)$$

$$= \int_0^d -N_0 e^{\frac{-xd}{\mu\tau V}} \times \delta(x' - t) dx' \quad (2.30)$$

$$= -N_0 e^{-\frac{d^2}{\mu\tau V}} \quad (2.31)$$

where multiple measured values of  $N_{pixel}$  will be fit against values of  $V$  to determine both  $N_0$  and  $\mu\tau$ . Again, the electric field has been assumed to be uniform and the effects of the non-ideal weighting potential will cause an over estimation of  $\mu\tau$  it not accounted for.

Eq. 2.29 can also be used to determine the  $\mu\tau$ -product where the numerical value of the exact weighting potential is used. The effects of these methods on determining the  $\mu\tau$ -product and the charge collection efficiency are discussed in Chapter IV.



## CHAPTER III

### Methods

#### 3.1 Fabrication

The majority of TlBr detectors in this work were grown and fabricated by Radiation Monitoring Devices, Inc. (RMD). A few detectors were fabricated by LLNL, but the material for these detectors was still grown by RMD.

##### 3.1.1 Growth

RMD grows TlBr by the traveling molten zone (TMZ) method. This is possible because of TlBr's simple cubic structure, low melting point (460 °C), and single solid phase [22]. RMD uses 5N pure TlBr beads which are loaded into a quartz ampule which is then sealed. The ampules used by RMD are circular with a  $\frac{1}{2}$ -inch diameter and they are loaded so that they are half full with TlBr. This yields boules with a semicircular cross-sectional area.

In the TMZ method, two heaters travel up and down the ampule moving a molten zone across the boule. Fig 3.1(a) shows the boule and the two heaters. Because impurities preferentially stay in the melt, moving these heaters up and down the boule collects impurities on one end (labeled at the tail in Fig. 3.1(b)). This results in purer material throughout the rest of the boule. This process is called zone refining, and the heaters traveling the length of the boule once is called a zone pass. The boules

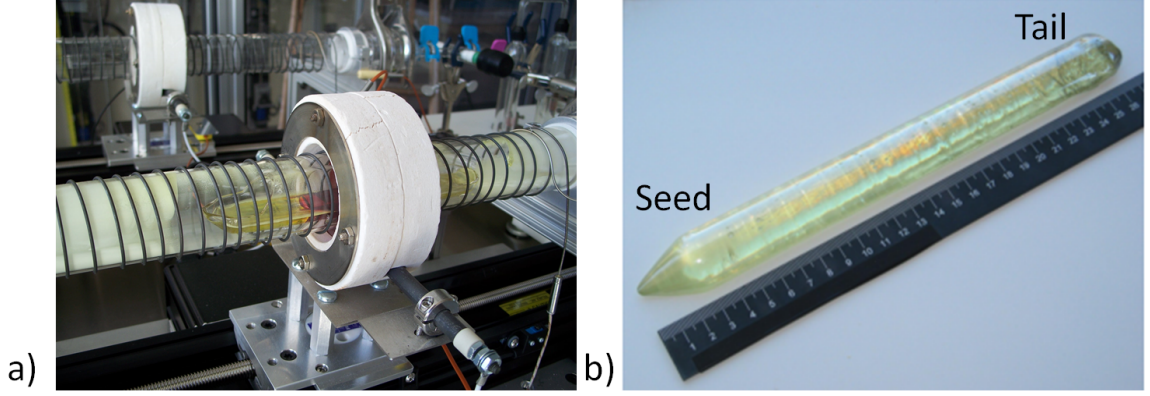


Figure 3.1: Photograph of the (a) TMZ growth setup, showing the two heaters and the TiBr material loaded in a quartz ampule and (b) the finished TiBr boule showing the pure end (seed) and less pure end (tail).

are refined for a large number (100-300) of zone passes with the heaters traveling at a speed of 50 mm/hr. After the zone refining is completed, the heaters perform one last slower growth pass at 2.5-5 mm/hr. Fig. 3.1(b) shows a completed boule removed from the quartz ampule.

### 3.1.2 Fabrication

The boule is then cut with a diamond wire saw into detectors. The detectors in this work are named based on this cutting process. The names have the form:

Boule Number	Region	Slice	Side
--------------	--------	-------	------

In the cutting process, the boule is first cut into three regions (A, B, and C) with the A region being from the purest end (seed). Numbered 5 mm thick slices are then cut from these regions, and the resulting hemispherical slice yields two 5 mm<sup>3</sup> detectors (L and R) from the left and right sides respectively.

For example, detector 58A3L comes from boule number 58, region A, slice 3, left side; Fig. 3.2 demonstrates this. For the larger 11x11 pixelated detectors (which are 12x12x5 mm<sup>3</sup>), the whole slice is used for one detector. This is indicated by an S, such as detector 935-38AS4 which is the whole fourth slice from region A in boule

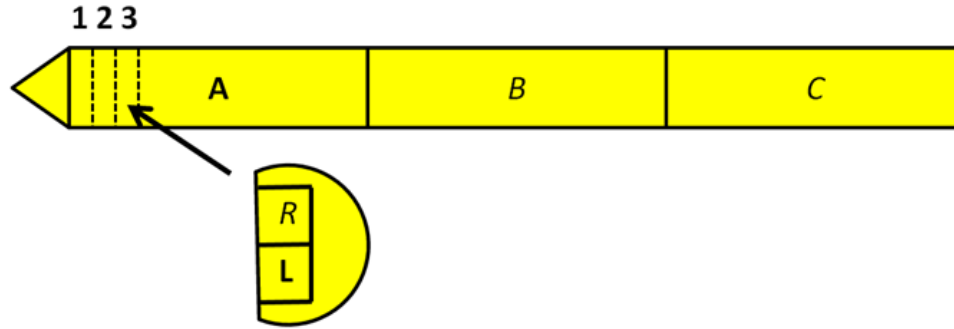


Figure 3.2: Diagram showing the boule location of detector 58A3L.

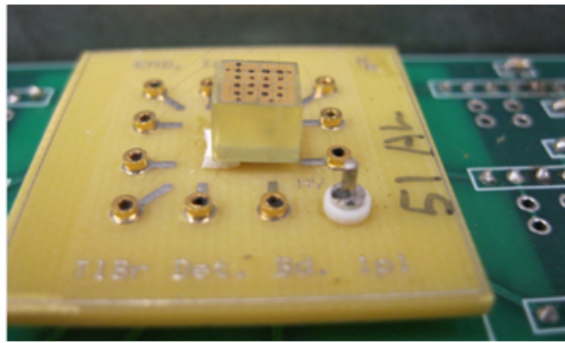


Figure 3.3: Picture of a packaged 3x3 TlBr detector

935-38. Detectors are sometimes refabricated multiple times during their lifetime and each refabrication is indicated by a (R) at the end of the detector name. For example, detector 58A3L(RR) is the second refabrication of detector 58A3L.

After cutting, the material is polished with  $3\ \mu\text{m}$  grain  $\text{Al}_2\text{O}_3$  to finalize the detector shape and to make flat surfaces for contact deposition. After polishing, the detector is etched to remove surface damage from cutting and polishing to prepare the surface for electrode deposition. The electrodes are then deposited using either vapor deposition or an electron beam and the detector is wire bonded using carbon paste to a substrate board. Fig. 3.3 shows a finished 3x3 TlBr detector.

The 11x11 arrays are flip-chip bonded to a substrate board by Polymer Assembly Technologies. Figure 3.4 shows an 11x11 array with the electrodes before bonding (anodes up) and after bonding (anodes down).

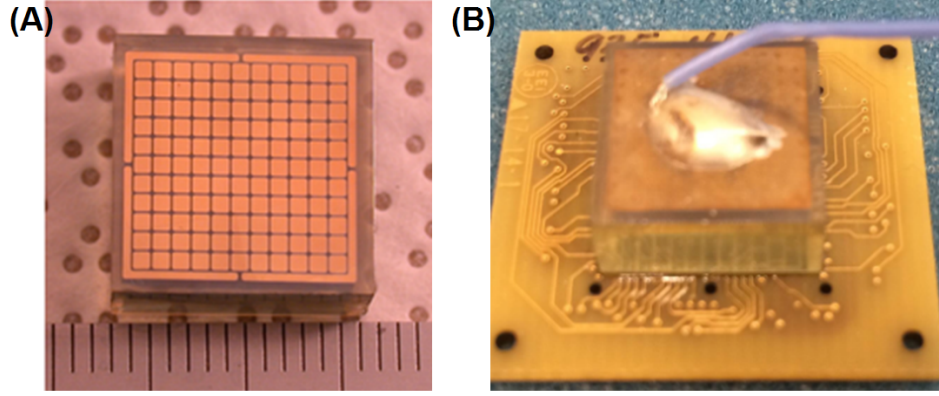


Figure 3.4: Picture of an 11x11 TlBr array showing the (a) contacts before bonding and (b) after flip-chip bonding to a substrate board. Silver expoxy is used to bond a cathode wire to the electrode.

Table 3.1: Details of processing methods

Name	Etchant	Electrode Metal
Standard	Br-MeOH	Cr/Au
LLNL	HCl	Pt (or Pd)

Two different fabrication methods (etchants and electrodes) were used in this work. The first is the standard fabrication method which was developed by RMD and used in all previous work at UM with TlBr. The second is the LLNL developed fabrication method which should provide longer stability at room temperature [43]. Table 3.1 shows the etchants and electrode materials for each process.

The standard process uses Br-methanol etching with contacts having a layer of Cr and then a layer of Au. These contacts are deposited by vapor deposition using a shadow mask. The LLNL method uses an HCl etch and primarily Pt contacts deposited by electron beam (though Pd contacts are used sometimes).

## 3.2 Read Out

### 3.2.1 3x3 Detectors

The signals from each anode pixel and the cathode are read out using eV-509 charge sensitive preamplifiers. These are mounted on a detector testing board where the detector is also mounted. Fig. 3.5 shows the layout of this board which includes preamplifier power and detector bias circuitry. Each anode is DC coupled to the preamplifiers which allows for measuring the leakage current through the preamplifier DC offset. The cathode is AC coupled to the preamplifiers which prevents preamplifier saturation from leakage current. Fig. 3.6 shows a picture of the testing board with a detector mounted.

The output of each preamplifier is connected by a coaxial cable to 14-bit GaGe Compuscope PCI-digitizers in a computer which are DC coupled and have a  $1\text{ G}\Omega$  input impedance. Fig 3.7 shows the outside of the testing box and the connections to the acquisition computer. The preamplifier power is supplied by an Agilent E3630A power supply and the high voltage by a Keithly Model 248 high voltage power supply.

In most measurements, the detector is cathode-biased to -1000V and flood irradiated with 662 keV gamma rays from  $^{137}\text{Cs}$ . Data are collected in the form of digitally sampled waveforms of the preamplifier output. Whenever the signal from any pixel crosses a preset trigger threshold, every pixel and the cathode is read out. Then the amplitude of each pixel is determined and the waveforms from each pixel which passes a software threshold (minimum amplitude) are saved. For most of this work, only the events where one pixel crosses the software threshold (or single-pixel events) are considered.

The preamplifier outputs are normally sampled at 10 MHz for 512 sample points unless otherwise stated. The saved waveforms are then processed later including amplitude determination, spectrum generation and depth correction.

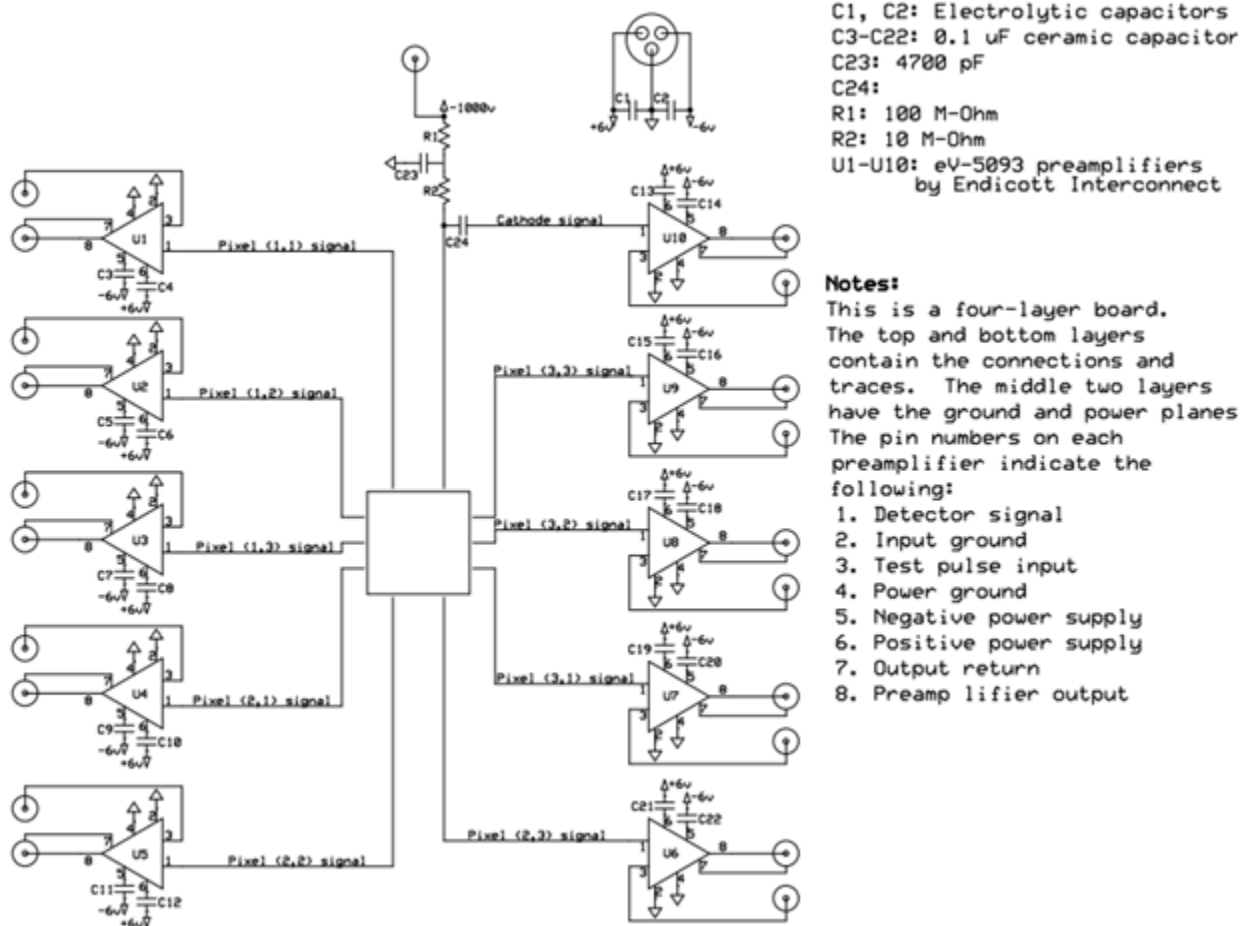


Figure 3.5: Layout of 3x3 detector testing board.

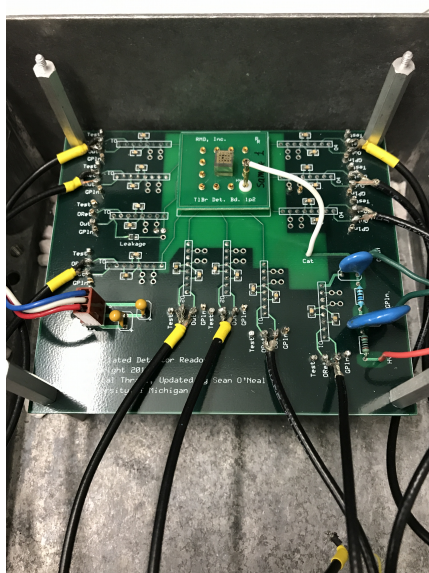


Figure 3.6: Picture of the detector testing board.

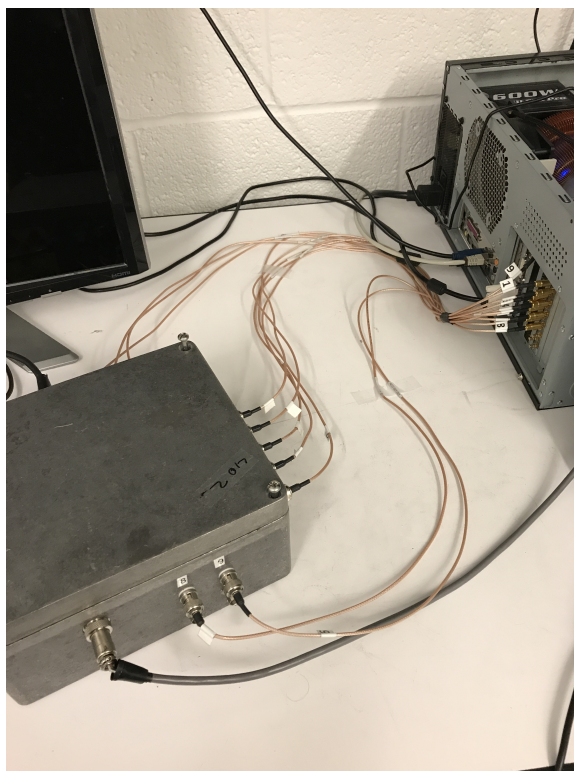


Figure 3.7: Picture of the outside of the detector testing box showing the connections to the data acquisition PC.

For cooled operation, the detector testing box is placed in a Thermotron S-1.2-3200 environmental chamber. This allows the detector to operate at a stable temperature anywhere between  $-30^{\circ}\text{C}$  and  $+40^{\circ}\text{C}$ .

### 3.2.2 Large Volume Detectors

For a larger number of anode pixels (such as 121), having discrete preamplifiers for each pixel is unfeasible, so an Application Specific Integrated Circuit (ASIC) has been developed to replace the preamplifiers. This development started with analog ASICs (VAS-TAT4 series) for pixelated CZT which had integrated shaping circuits and only provided the amplitude and timing of each triggered pixel [44]. To improve the performance of the CZT detectors, a digital ASIC (VAD-UM series) has been developed by the collaboration between the UM group and Ideas, AS [45]. Due to the similarities between CZT and TlBr, the ASICs developed for CZT can also be applied to TlBr. Given the longer drift times in TlBr, however, some modifications were made in the second generation of the ASIC to allow for lower sampling frequencies.

Fig. 3.8 shows a basic layout of the digital ASIC system hardware. More information about the ASIC systems is presented in Chapter VI. The ASIC functions as the preamplifier for each channel and samples the output. The sampled waveforms are then sent as a differential current signal to the Espresso board which controls the ASIC and has the analog-to-digital converters (ADC). These digital signals are then sent to the computer through a field-programmable gate array (FPGA) controlled read out board which communicates with the controlling PC. Fundamentally, the signal the PC receives from the ASIC is the same as from the GaGe cards, though the waveforms are only 160 points and not as many sampling frequencies are available.



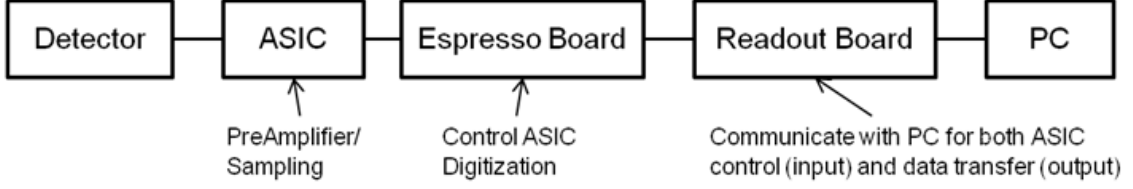


Figure 3.8: Basic layout of the digital ASIC systems, showing the important components.

### 3.3 Digital Signal Processing

Digital signal processing (DSP) is used to determine the amplitude of the recorded waveforms. Since the raw waveforms are saved, multiple different processing techniques can be applied to the same data to investigate the effects on performance. This can include various digital filters designed to mimic analog circuitry (such as CRRC shaping) or purely digital techniques such as simple subtraction.

#### 3.3.1 CRRC

Fig. 3.9 shows an example TlBr anode waveform and the waveform shaped with a four-stage CRRC digital filter with a  $15\ \mu\text{s}$  shaping time. A horizontal line in Fig 3.9 shows the determined amplitude. For this waveform, the CRRC4 shaping successfully calculates the amplitude. The effective shaping time can be varied measurement to measurement to ensure the amplitude is determined properly in each one.

#### 3.3.2 Simple Subtraction

For the majority of waveforms in this work, the amplitude is determined by simple subtraction. Fig. 3.10 demonstrates this process. A number of points (usually 100 in  $3\times 3$  waveforms) in the tail region are averaged and the baseline (also calculated as an average) is subtracted to determine the amplitude. This mimics a trapezoidal filter, and is not subject to the effects of ballistic deficit as long as the charge drift time is short relative to the total sampling time. The amplitude than can be calculated

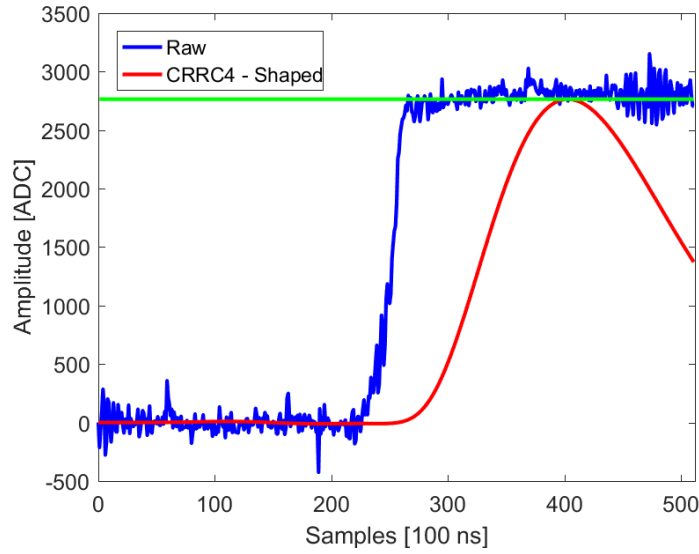


Figure 3.9: Example of CRRC4 digital shaping on an anode TlBr waveform showing the raw waveform (blue), shaped waveform (red) and determined amplitude (green).

correctly as long as the baseline and tail regions chosen do not include the drift of carriers or preamplifier decay.

The effects of electronic noise on the amplitude determined by simple subtraction depends on the number of points chosen in each region. A higher number of points typically reduces the effects of noise.

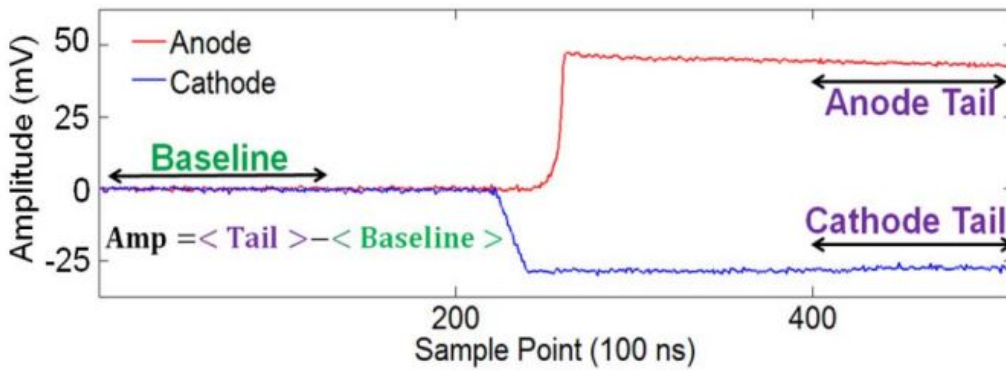


Figure 3.10: Example of 100-point simple subtraction used to determine the amplitude of a TlBr anode waveform.

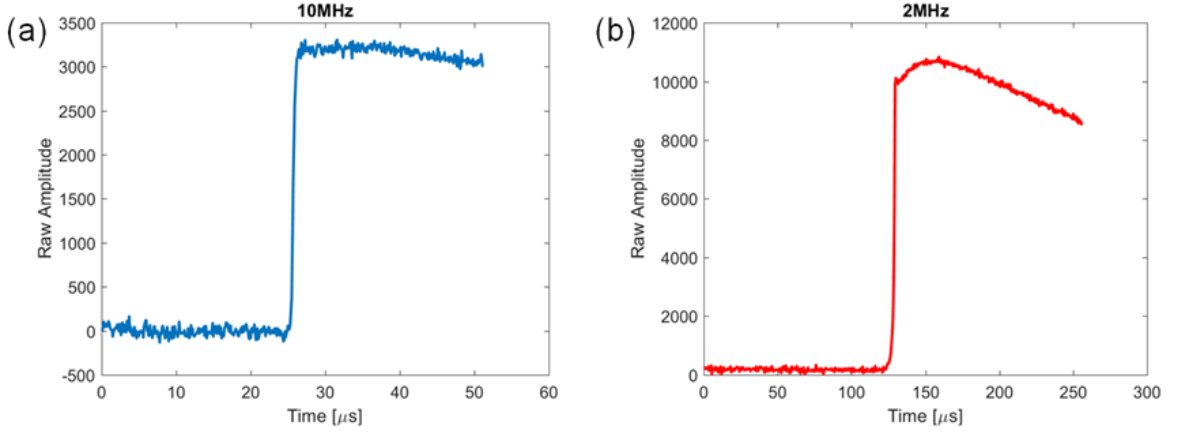


Figure 3.11: Example raw waveforms take at (a) 10MHz and (b) 2MHz showing the effects of preamplifier decay.

### 3.4 Decay Correction

For some detectors in this work, longer observation times were desired. This can be due to lower electric fields from high space charge in detectors or from operating the detectors in reverse bias (holes drifting towards anode) for material analysis due to the much lower mobility of holes than electrons. The longer collection time causes the recorded waveforms to suffer from preamplifier decay. Figure 3.11 shows a comparison between a typical TlBr waveform sampled at 10 MHz and one sampled at 2MHz. The preamplifier has decayed significantly in the 2 MHz case and simple subtraction will yield a poor estimation of the waveform amplitude. To mitigate these effects, a preamplifier decay correction was developed.

#### 3.4.1 Theory of Decay Correction

The decay from the preamplifier can be corrected for in digital waveforms by use of the Fourier transform. The preamplifier decay can be modeled as an exponential. So the preamplifier signal,  $f(t)$ , from an input charge,  $Q_0$ , is given by Eq. 3.1,

$$f(t) = Q_0 e^{-t/\tau} \quad (3.1)$$

where  $\tau$  is the decay constant. The measured waveform,  $Q(t)$ , can be expressed as a convolution of this decay function and the rate of charge arrival,  $q(t)$ , or

$$Q(t) = \int_0^t q(\Delta) e^{-\frac{t-\Delta}{\tau}} d\Delta = [q * f](t). \quad (3.2)$$

Using the Fourier transform, the unknown rate of charge arrival can be deconvolved from the measured waveform using the known preamplifier decay function.

$$q(t) = \mathcal{F}^{-1} \left\{ \frac{\mathcal{F}\{Q(t)\}}{\mathcal{F}\{f(t)\}} \right\} \quad (3.3)$$

The undecayed waveform,  $Q^*(t)$ , can then be reconstructed by integrating the rate of charge arrival. This is the same as applying a virtual preamplifier with a decay constant of infinity.

$$Q^*(t) = \int_0^t q(t') dt' \quad (3.4)$$

In discrete space, the decay correction can be done using the discrete-time Fourier Transform (DTFT). So given a measured waveform,  $Q[n]$ , and a preamplifier decay function,  $f[n]$ , the undecayed waveform  $Q^*[n]$  can be calculated as

$$Q^*[n] = \sum_{n=1}^N DTFT^{-1} \left\{ \frac{DTFT\{Q[n]\}}{DTFT\{f[n]\}} \right\}. \quad (3.5)$$

### 3.4.2 Validation on Simulated Waveforms

Figure 3.12 shows the application of the decay correction to a simple simulated cathode waveform where the preamplifier decay constant is small and only electrons drift. The resulting no decay waveform shows the proper flat tail region compared with the original waveform.

Figure 3.13 shows the application of the decay correction to a more complicated simulated cathode waveform. Here the drift of holes is considered, Gaussian noise is

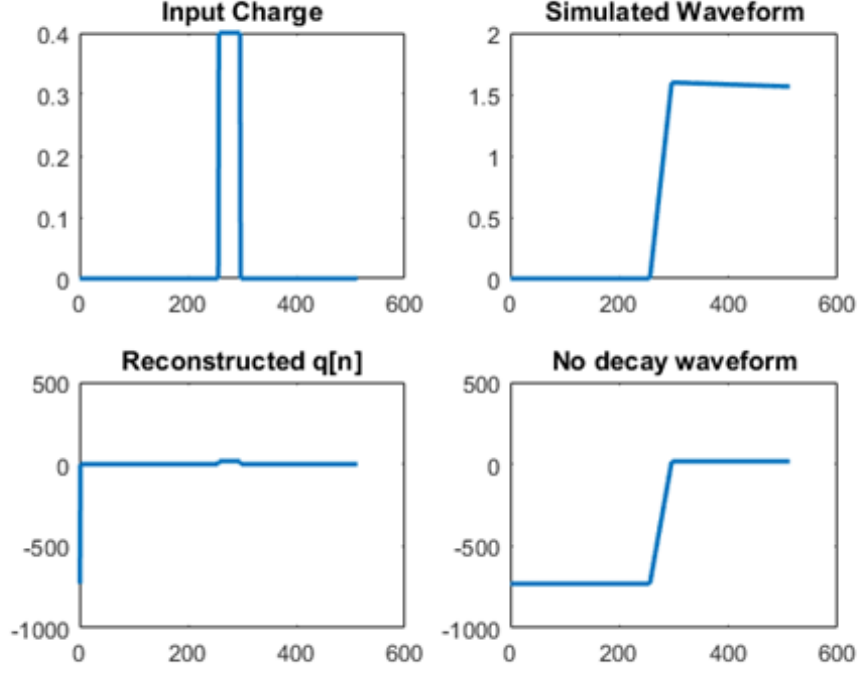


Figure 3.12: Decay correction examples using simple simulated data.

added to the simulated waveform, and the event occurs on a large baseline decay. The reconstructed charge drift,  $q[n]$ , is significantly effected by the Gaussian noise, but the no decay waveform shows similar noise performance to the simulated waveform.

The large preamplifier decay has been removed from the no decay waveform resulting in a flat baseline. The tail of the waveform also shows the correct positive slope from hole motion. This demonstrates the decay correction technique is robust against noise and also works in high count rate environments when the measured waveform may sit on a large decay from previous events.

### 3.4.3 Validation on Measured Waveforms

Figure 3.14 shows the decay correction performed on one measured anode waveform at 5 MHz. The decay correction successfully flattens the tail region of the waveform. Two regions are highlighted in the raw waveform (Fig. 3.14(a)) and the ratio of the green region to the red region was used to validate the quality of the

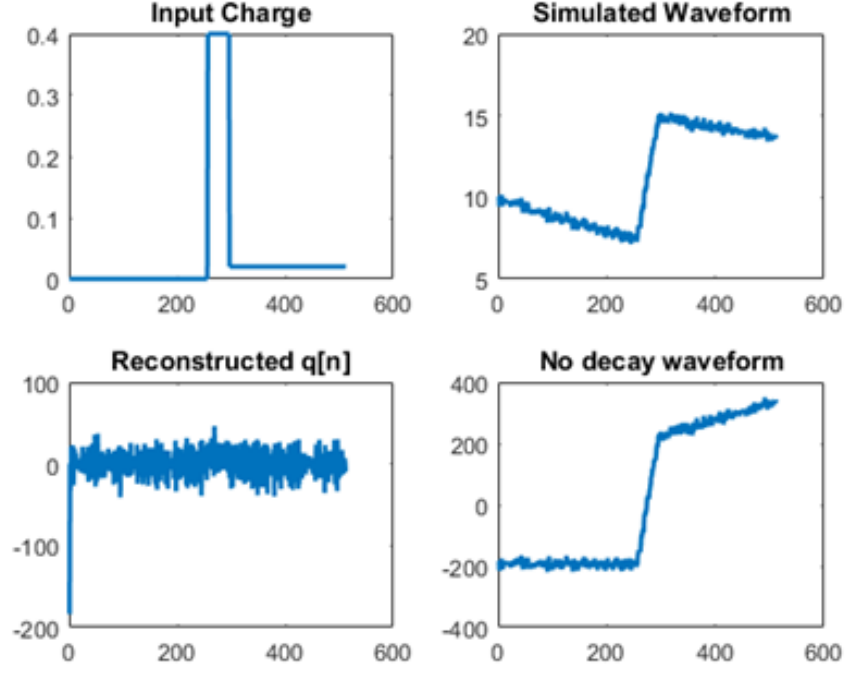


Figure 3.13: Decay correction examples using simulated data with hole drift, Gaussian noise, and a large baseline decay.

Table 3.2: Mean and median for the distributions shown in Fig. 3.15

5 MHz	Mean	Median
Before Correction	0.9089	0.9051
After Correction	0.9942	0.9900

correction on many waveforms.

Figure 3.15 shows the distribution of the ratio of the green region and red region in Fig. 3.14(a) for many waveforms with Table 3.2 showing the mean and median of each distribution. After the decay correction, the mean of the distribution is shifted to close to one, demonstrating that the preamplifier decay has been reduced from these waveforms. The decay constant of the preamplifiers was empirically determined by choosing the value that best shifted the mean and median of the distribution near unity.

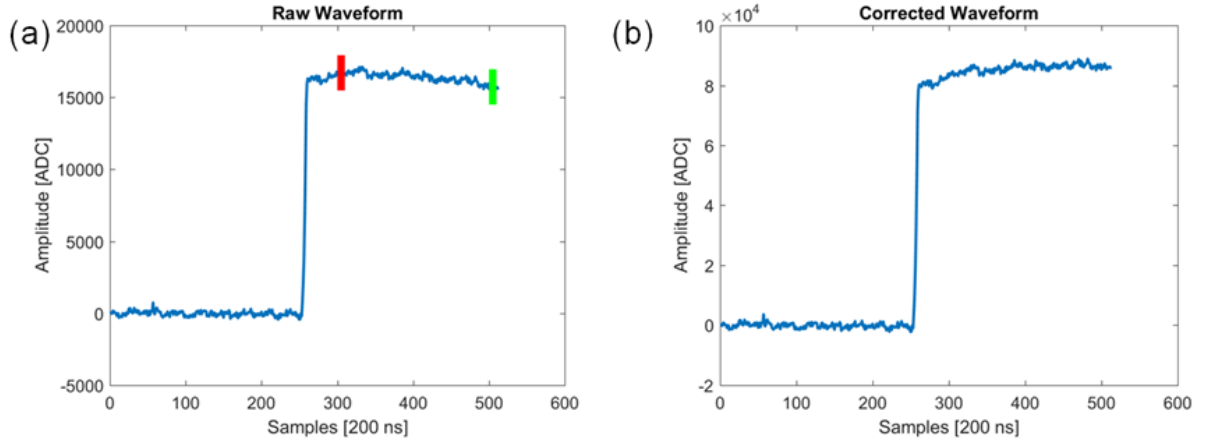


Figure 3.14: Example of decay correction on a measured waveform at 5MHz showing both the (a) raw and (b) corrected waveforms. Two regions are highlighted in the tail of the raw waveform which are used to measure the amount of decay in the waveform.

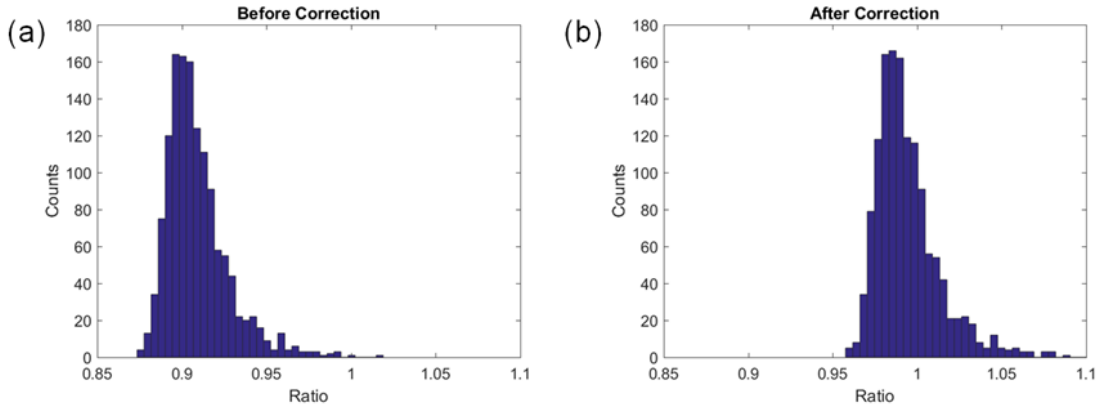


Figure 3.15: Distribution of tail decay in (a) raw and (b) decay corrected waveforms using the ratio of the green region to the red region in Fig. 3.14(a)

## CHAPTER IV

### Material Characterization

#### 4.1 Ionization Energy

As discussed in Section 2.2.1, the ionization energy determines the fundamental limit of the energy resolution in a semiconductor radiation detector, so accurately measuring it is important when comparing the potential performance of different materials.

For most semiconductors, the ionization energy is approximately 3 times the bandgap. This is described by Klein's semi-empirical relation shown in Eq. 4.1 [46]. Fig. 4.1 shows the ionization energy versus the bandgap for a number of semiconductor materials.

$$w = \frac{14}{5}E_{gap} + r(\hbar\omega_r), \quad 0.5 < r(\hbar\omega_r) < 1.0 \text{ eV} \quad (4.1)$$

As shown in Fig. 4.1, many materials (including Si, Ge, and CdTe) fall along the Klein relation, but TlBr is among a different class of materials which deviate from the Klein relation having an ionization energy less than that predicted by Eq. 4.1. The ionization energy value for the TlBr used in Fig. 4.1 is 6.5 eV (compared with  $\sim 8$  eV estimated by the Klein relationship) which was reported by Shah et al. in 1989 [47].

Because there are so few materials on the line with TlBr, and TlBr has the largest



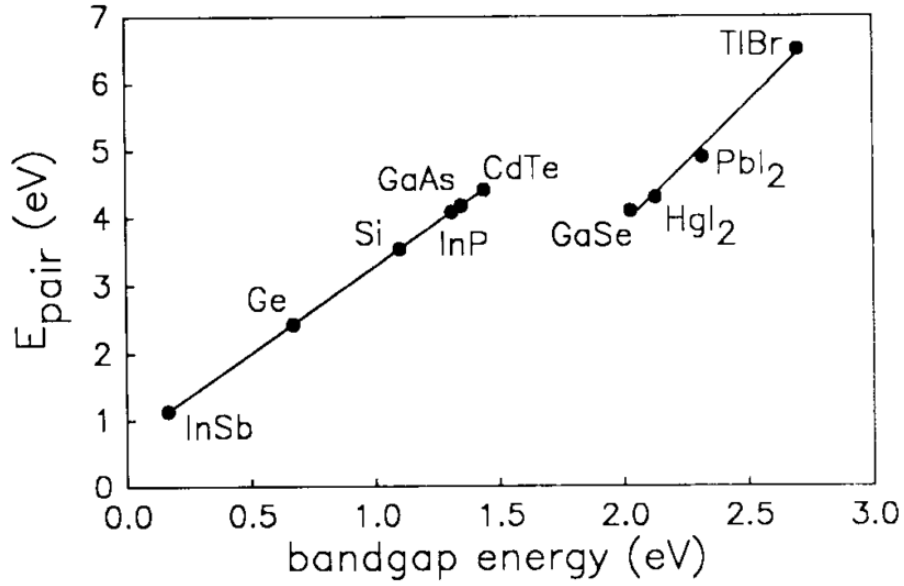


Figure 4.1: Ionization energy versus bandgap for many semiconductor materials from Ref [47], using their value of the ionization energy for TlBr. TlBr falls off the Klein relation on a line with a different slope.

bandgap of these materials, updating the ionization energy can have a drastic effect on the fit for the materials which fall off the Klein relation. Establishing an accurate fit for these non-Klein materials may be helpful in generating theory to explain their deviation from the traditional materials. Hitomi et al. reported a value of 5.50 eV in 2015 [48]. Using this values instead of the one used in Fig. 4.1 will drastically reduce the slope of the fit for the non-Klein materials.

Often, the measured ionization energy of semiconductors reduces as the growth processes are more refined. This is normally due to improvements in the material purity. Hitomi et al. proposed correcting the measured ionization energy by the charge collection efficiency to account for material purity and thus to better estimate the true material limit [48]. This caused Hitomi et al. to reduce their initial measurement from  $6.34 \pm 0.04$  eV, when trapping is not accounted for, to their reported value of  $5.50 \pm 0.05$  eV [48].

In their work, Hitomi et al. used the classic Hecht relation (Eq. 2.28) to cal-

culate the  $\mu\tau$ -product and the charge collection efficiency. This incorrectly reported the  $\mu\tau$ -product because they were using a pixelated detector and the classic Hecht relation only applies to planar electrodes. However, due to the low trapping in their detector, the calculated CCE is still appropriate and their results can be used. This is demonstrated in Section 4.1.4.1.

In this work, in order to better understand the limiting resolution of TlBr, validate the results of Hitomi, and find the best available modified Klein relation for materials not covered by the conventional one, the ionization energy of TlBr was measured. The measurement was done at  $-20^\circ\text{C}$  and room temperature by comparison with Si, using two different detectors. The results were corrected using the CCE determined from Hecht fitting and the updated two-bias method (with the corection factor for non-ideal weighting potential as discussed in Sec. 2.4.1).

#### 4.1.1 Comparison

The signal amplitude,  $A$ , from a semiconductor can be written as

$$A = \frac{E_\gamma}{w} CCE, \quad (4.2)$$

where  $E_\gamma$  is the energy deposited by the gamma ray,  $w$  is the material ionization energy, and  $CCE$  is the charge collection efficiency in the detector.

By comparing the ratio of the the amplitude from two materials irradiated by the same gamma rays, the ratio of the ionization energies can be calculated. For Si and TlBr, this yields,

$$\frac{w_{TlBr}}{w_{Si}} = \frac{(CCE)_{TlBr}}{(CCE)_{Si}} \frac{A_{Si}}{A_{TlBr}}. \quad (4.3)$$

The ionization energy of TlBr can then be determined by comparing the pulse height from  $^{241}\text{Am}$  in TlBr to that in Si and correcting for charge collection efficiency (CCE).

$^{241}\text{Am}$  gamma rays (59.5 keV) were chosen because they are low enough energy to

be stopped by Si with high efficiency and with cathode-side irradiation in TlBr all the events will occur very close to the cathode surface. This is because the mean free path of  $^{241}\text{Am}$  gamma rays in TlBr is only  $\sim 300 \mu\text{m}$  [33]. With all the events occurring at the cathode side, all collected charge will travel the full weighting potential. This implies no depth correction is needed, and all the assumptions in the various  $\mu\tau$ -product models are valid.

Due to the very high  $\mu\tau$ -product in Si, the CCE was assumed to be unity for Si. The ionization energy of TlBr,  $w_{\text{TlBr}}$ , can then be determined by Eq. 4.4.

$$w_{\text{TlBr}} = \text{CCE}_{\text{TlBr}} \frac{A_{\text{Si}}}{A_{\text{TlBr}}} w_{\text{Si}} \quad (4.4)$$

Where  $w_{\text{Si}}$  is taken to be  $3.67 \pm 0.02 \text{ eV}$  from Ref [49].

#### 4.1.2 Detectors

Two different TlBr detectors were used for measurements at  $-20^\circ\text{C}$  and room temperature. Detector 935-16B1R operated at  $-20^\circ\text{C}$  and detector 935-38AA2L operated at room temperature. Both detectors offered reproducible performance at their respective temperatures, but could not be operated at the other temperature stably. Detector 935-16B1R is an older detector fabricated using the standard process, and would likely polarize very quickly at room temperature leading the  $^{241}\text{Am}$  photopeak amplitudes changing rapidly (and non-reproducibly) with time.

Detector 935-38AA2L is newer material which is more stable at room temperature, but degrades with time at  $-20^\circ\text{C}$  (see Section 4.3.2 for discussion of the cooled performance of a similar detector, detector 935-38AA1R). Cooled results with this detector would not be repeatable. Detector 935-38AA2L is fabricated using the LLNL technique.

The silicon detector in this work was a Hamamatsu PIN diode (S1223) which was read out using the same detector testing board as the TlBr detectors. The diode

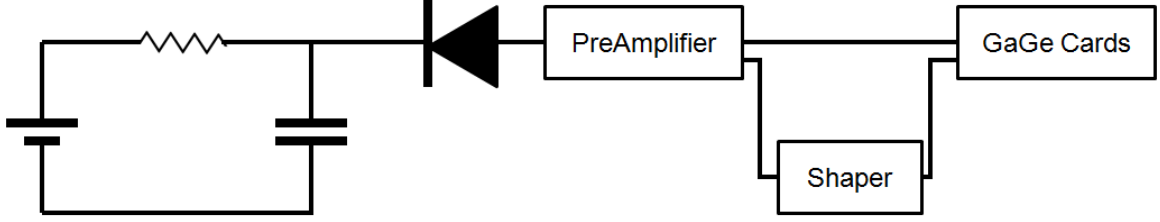


Figure 4.2: Block diagram of the Si detector measurement system showing the RC filter on the power supply, the PIN diode, and the shaping amplifier used for triggering.

was biased until full charge collection was achieved within  $10 \mu s$  ( $\sim 30$  V) and was irradiated with  $^{241}\text{Am}$  gamma rays. The Si detector bias was provided by an Aligent E3630A power supply, which was filtered through an RC circuit. Fig. 4.2 shows a block diagram of the measurement setup. Because the Si detector produced small-amplitude negative pulses, a shaping amplifier was used to trigger the GaGe cards. Fig. 4.3 shows an example Si pulse waveform, showing the full collection in the  $51.2 \mu s$  window. The pulse amplitudes were determined using 100-point simple subtraction, the same method applied to the TlBr detectors.

#### 4.1.3 Measurements

Detector 935-16B1R was cooled to  $-20^\circ\text{C}$  and operated for approximately a week to ensure it had reached stable operation after conditioning (see Ref [27] for a detailed explanation of the conditioning in TlBr detectors). Once stable operation was achieved, the spectrum from cathode-side irradiation with  $^{241}\text{Am}$  gamma rays was recorded. Due to noise issues and the exact placement of the source, usable spectra were recorded with six of the nine pixels. The  $\mu\tau$ -product was determined by operating the detector as two biases, 1000 V and 1500 V.

Detector 935-38AA2L was operated at room temperature and was also cathode-side irradiated with  $^{241}\text{Am}$  gamma rays. The detector operated at a range of biases from 200 V to 1000 V so the  $\mu\tau$ -product could be determined by Hecht fitting. Due

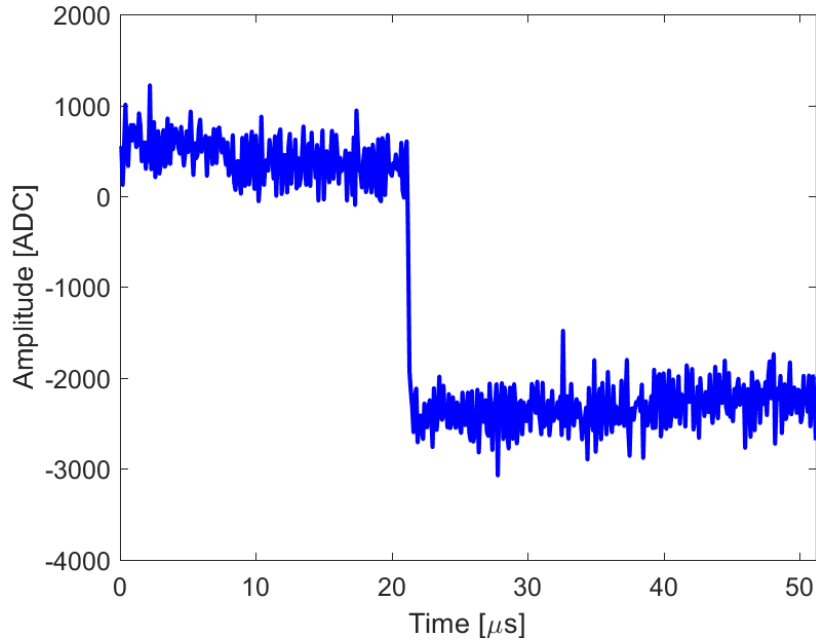


Figure 4.3: Example Si detector waveform showing full collection time in the  $51.2 \mu s$  window (512 samples at 10 MHz). The waveform is linear as expected for the planar PIN diode.

to problems with some of the pixels, usable spectra were only recorded by four of the nine pixels in detector 935-38AA2L.

The Si detector was plugged into each pixel on the detector testing board and a spectrum using each preamplifier was generated. The Si detector was also tested at both room temperature and  $-20^\circ\text{C}$  to ensure that any drift in the electronics was taken into account. Greater than 10,000 counts were recorded with each pixel to ensure the uncertainty in the Si photopeak centroid was very low.

#### 4.1.4 Results

##### 4.1.4.1 Comparison of Trapping Models

Fig. 4.4 shows the  $^{241}\text{Am}$  spectrum from an example pixel of detector 935-38AA2L at room temperature and multiple different biases. Fig. 4.5 shows the centroid versus bias fit by both the classic Hecht relation (Fit 1, Eq. 2.28) and the modified Hecht

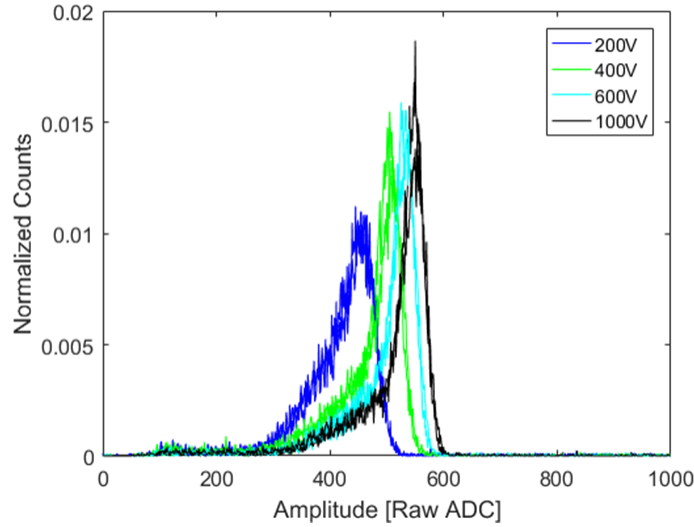


Figure 4.4:  $^{241}\text{Am}$  spectrum in detector 935-38AA2L (pixel 3) for multiple detector biases.

Table 4.1: Charge collection efficiency fit parameters for detector 935-38AA2L

Fit Type	$\mu_e\tau_e$ [ $10^{-3}$ cm <sup>2</sup> /Vs]	CCE at 1000 V
Perfect WP	4.0	0.954
Correct WP	3.6	0.954
Classic Hecht (Linear WP)	1.9	0.952

relation for pixelated detectors (Fit 2, Eq. 2.31). (Note: these fits are very similar and overlap in Fig. 4.5).

Table 4.1 shows the fit parameters for three different fits to the centroid versus bias for the detector. These are the two fits shown in Fig. 4.5 and a third one using the exact weighting potential of the pixelated detector (numerically evaluated using Eq. 2.29). These fits show very close values for the CCE, though they vary greatly in their calculated  $\mu_e\tau_e$ -product. The perfect weighting potential over estimates the  $\mu\tau$ -product by approximately 10% which is expected when the correction factor from the two-bias method is not used.

The roughly correct CCE determination even for the classic Hecht relation is because the trapping in the detector is low. As shown in Table 4.1, the determined  $\mu\tau$ -product for the classic Hecht relation is approximately  $\frac{1}{2}$  that of the perfect weighting

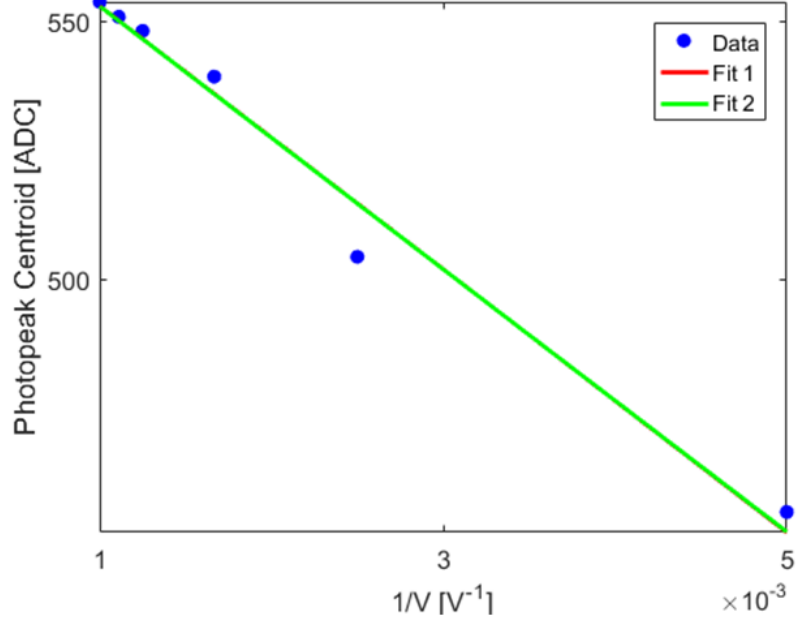


Figure 4.5: Photopeak centroid versus bias for detector 935-38AA2L showing fits for both the classic Hecht relation (Eq. 2.28) and the modified Hecht relation (Eq. 2.31). (Note: these fits are very similar and overlap in the figure).

potential. This is expected in the case of low trapping.

Eq. 4.7 shows the Taylor expansion of the classic Hecht relation (Eq. 2.28) when the trapping is small, with Eq. 4.10 showing the same for the pixelated Hecht relation (Eq. 2.31).

$$CCE_{planar} = \frac{\mu\tau V}{d^2} \left[ 1 - e^{-\frac{d^2}{\mu\tau V}} \right] \quad (4.5)$$

$$\approx \frac{\mu\tau V}{d^2} \left[ 1 - \left( 1 - \frac{d^2}{\mu\tau V} + \frac{1}{2} \left( \frac{d^2}{\mu\tau V} \right)^2 - \mathcal{O} \left( -\frac{d^2}{\mu\tau V} \right)^3 \right) \right] \quad (4.6)$$

$$\approx 1 - \frac{1}{2} \frac{d^2}{\mu\tau V} \quad (4.7)$$

$$CCE_{pixel} = e^{-\frac{d^2}{\mu\tau V}} \quad (4.8)$$

$$\approx 1 - \frac{d^2}{\mu\tau V} + \mathcal{O} \left( -\frac{d^2}{\mu\tau V} \right)^2 \quad (4.9)$$

$$\approx 1 - \frac{d^2}{\mu\tau V} \quad (4.10)$$

Table 4.2: Ionization energy in detector 935-38AA2L (room temperature

Pixel	$A_{Si}$ [ADC]	$A_{TLBr}$ [ADC]	CCE at 1000V	$w_{eff}$ [eV]	$w$ [eV]
1	767.06	541.1	0.948	5.20	4.93
3	768.03	553.94	0.954	5.09	4.85
4	754.99	556.84	0.960	4.98	4.78
6	752.02	549.95	0.948	5.02	4.76
Average:				5.07(10)	4.83(8)

When the trapping is low, to first order, both are in the form

$$CCE = 1 - a \frac{d^2}{\mu\tau V} \quad (4.11)$$

where  $a$  is  $\frac{1}{2}$  for a planar detector and unity for a pixelated detector. This implies that for the same  $\mu\tau$ -product, the CCE for a pixelated detector will be lower. This is expected because trapped charge induces some signal in the linear case, but induces none in the perfect pixelated weighting potential case.

However, if the classic Hecht relation is applied to a pixelated detector with low trapping, the fit will result in an under reporting of the  $\mu\tau$ -product by approximately a factor of 2, but a good estimate of the CCE.

Hitomi et al. reported a  $\mu\tau$ -product of  $1.34 \times 10^{-3} \text{ cm}^2/\text{Vs}$ . This implies the true  $\mu\tau$ -product for their detector was actually closer to twice that, but their estimation of the CCE was accurate to within 1%, as demonstrated in the results from detector 935-38AA2L shown in Table 4.1.

#### 4.1.4.2 Detector 935-38AA2L - Room Temperature

Table 4.2 shows the calculation of the ionization energy from 4 pixels of detector 935-38AA2L at room-temperature. Where  $w_{eff}$  is the uncorrected ionization energy, and  $w$  is the true ionization energy as calculated using Eq. 4.4, corrected with the CCE determined using the true weighting potential fit.

The ionization energy in detector 935-38AA2L was determined to be  $4.83 \pm 0.08 \text{ eV}$



Table 4.3: Ionization energy in detector 935-16B1R ( $-20^{\circ}C$ )

Pixel	$A_{Si}$ [ADC]	$A_{TlBr}$ [ADC]	$\mu_e\tau_e$ [ $10^{-3} \text{ cm}^2/Vs$ ]	CCE at 1000 V	$w_{eff}$ [eV]	w [eV]
1	256.7	161.0	4.2	0.94	5.85	5.51
3	254.1	165.9	10	0.97	5.62	5.49
4	248.9	165.0	6.4	0.96	5.53	5.32
6	256.0	170.9	12	0.98	5.58	5.47
8	259.8	169.0	12	0.98	5.64	5.53
9	250.2	158.9	11	0.98	5.78	5.64
Average:					5.67(12)	5.49(10)

at room temperature.

#### 4.1.4.3 Detector 935-16B1R - Cooled ( $-20^{\circ}C$ )

Table 4.3 shows the calculation of the ionization energy from six pixels in detector 935-16B1R. The  $\mu\tau$ -product was calculated using the two-bias method (Eq. 2.26) and was quite high with a number of pixels achieving greater than  $1 \times 10^{-2} \text{ cm}^2/Vs$ . (Note: a different ADC dynamic range was used for the two different detectors resulting in the large difference of the raw amplitudes in the two cases.)

The ionization energy in detector 935-16B1R was determined to be  $5.49 \pm 0.10 \text{ eV}$  at  $-20^{\circ}C$ .

#### 4.1.4.4 Comparison of Results

The two measurements of the ionization energy do not agree within error, though each detector showed stable signal amplitudes and reproducible results. This implies it is possible that the ionization energy of TlBr can change with temperature.

It is also possible that difference in the growth and fabrication of the materials also effects the ionization energy. Since the growth of boule 935-16, RMD has changed their growth process to improve the room temperature stability of the detectors. This may account for some of the differences between the samples.

Additionally, detector 935-38AA2L (the room temperature detector) also showed

strange properties with apparent charge multiplication (see Sec. 4.2) and this may also account for its measured ionization energy being lower. This detector was used for the ionization energy measurements despite its odd behavior because it produced the most reproducible results at room-temperature.

In the determination of the cooled ionization energy, the room-temperature ionization energy of Si was used under the assumption that the ionization energy is constant with temperature. The ionization energy does increase very slightly as the temperature decreases, increasing by 4% between room temperature and 77 K [1]. This would indicate that the cooled ionization energy could be slightly higher than reported here, but this does not account for the large difference observed between the two temperatures.

Given the odd behavior of detector 935-38AA2L and the agreement between the cooled results and those reported by Hitomi et al. in Ref [48], it is very likely that the ionization energy of TlBr is 5.5 eV.

#### 4.1.5 Prediction of Limiting Energy Resolution

As shown in Eq. 2.5, the ionization energy can be used to estimate the theoretical limiting energy resolution. This requires knowledge of the Fano factor in the material. Though the Fano factor is often take to be  $\sim 0.1$  for all materials, the Fano factor depends on the exact phonon energy levels in the material and thus can vary between different detector materials [46]. Without measuring phonon levels, the Fano factor can still be estimated by comparing the ionization energy to the band gap [50], this is shown in Eq. 4.12.

$$F_{Theory} \approx \frac{1}{6} \left( \frac{w - E_{gap}}{w} \right)^2 \quad (4.12)$$

Using Eq. 4.12, the Fano factor of Si is estimated to be 0.07 and Ge is 0.09. These are reasonably close to reported measured values of the Fano factor which validates the accuracy of Eq. 4.12 at determining the Fano factor.

Table 4.4: Comparison of theoretical limit of resolution in TlBr and CZT at 662 keV

Material	CZT	TlBr
Band Gap [eV]	1.64	2.68
W [eV]	4.6	5.49
$F_{theory}$	0.069	0.044
$R_{limit}$ at 662 keV	0.16%	0.14%

Table 4.4 shows a comparison of the theoretical limiting energy resolution of TlBr to CZT at 662 keV using the CZT ionization energy reported in Ref [51] and the cooled (higher) ionization energy from this work, with the material specific Fano factor determined by Eq. 4.12. Because the ratio of the ionization energy to band gap in TlBr is much lower, the predicted Fano factor is lower and therefore the limiting energy resolution is better in TlBr than in CZT even with its wider band gap.

Even assuming the same conservative Fano factor of 0.1 for both materials, the predicted limiting energy resolution at 662 keV is 0.19% and 0.21% for CZT and TlBr respectively. This shows that the fundamental limiting performance of TlBr is very similar to that of CZT, although neither material has achieved this performance.

Both materials are currently limited by material non-uniformity and electronic noise. A detailed study of the phonon modes in both TlBr and CZT is needed to more accurately estimate their Fano factors, but these results demonstrate that TlBr could be capable of comparable energy resolution to that of CZT as the material uniformity continues to improve.

#### 4.1.6 Conclusions

The ionization energy of two TlBr detectors was measured and found to be  $4.83 \pm 0.08$  eV at room temperature and  $5.49 \pm 0.10$  eV at  $-20^\circ\text{C}$  when corrected for charge collection efficiency. The higher value agrees with the previously reported value by Hitomi et. al. [48], and the variation between the two measurements may be due to both material differences and temperature.

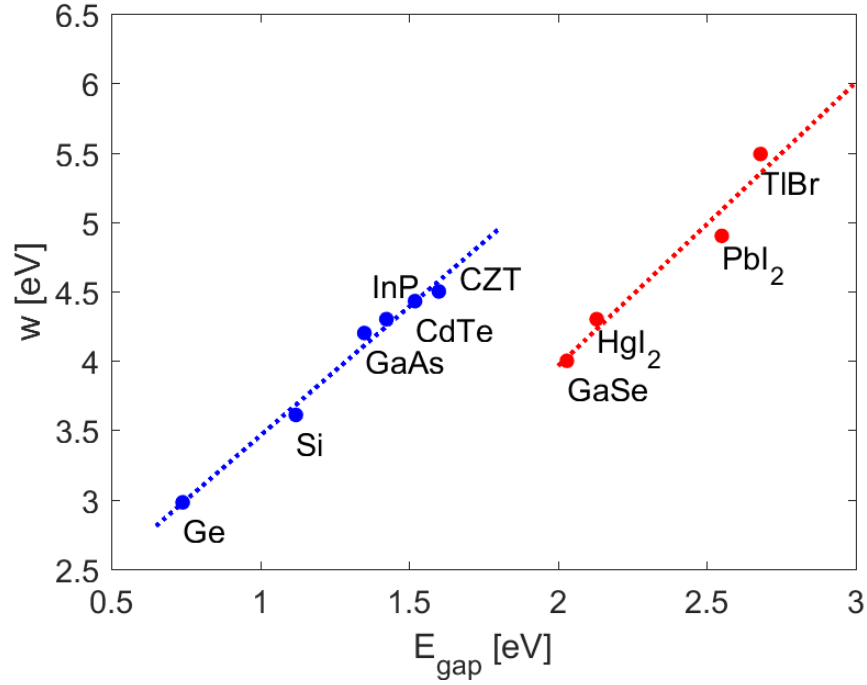


Figure 4.6: Ionization energy versus bandgap for many semiconductor materials using the value for TlBr obtained in this work. Other materials ionization energies from Refs [1] and [12].

The charge collection efficiency was determined both by Hecht fitting and the two-bias method with the correction factor for non-ideal weighting potentials. Due to the low trapping in these detectors, the charge collection efficiency was demonstrated to not be a strong function of the trapping model, though using the proper trapping model is important for precise determination of the  $\mu\tau$ -product.

The ratio of the ionization energy to the band gap in TlBr is much lower than with many other semiconductor materials (at  $\sim 2$  to 1, instead of  $\sim 3$  to 1), and this causes the theoretical limiting energy resolution of TlBr to be similar to that of CZT even though it has a much wider band gap.

Fig 4.6 shows the updated version of Fig 4.1 using the results from this work and the most recently published values of the ionization energy for the other non-Klein materials. With the updated TlBr ionization energy, the slope of the fit for non-Klein materials is reduced by  $\sim 10\%$ .

## 4.2 Anode Slopes

Some of the recently grown TlBr detectors have shown high-energy tails in their photopeaks. Fig 4.7 shows an example of a spectrum from detector 935-38AA2L showing this tailing. The high energy tail appears in the corrected spectra and in the raw spectra in the individual depth bins (as shown in Fig. 4.7(b)). This indicates that the high-energy tailing is not an effect that can be corrected by aligning peaks from each voxel like with the trapping correction. However, it is a part of the response of the detector at the voxel level.

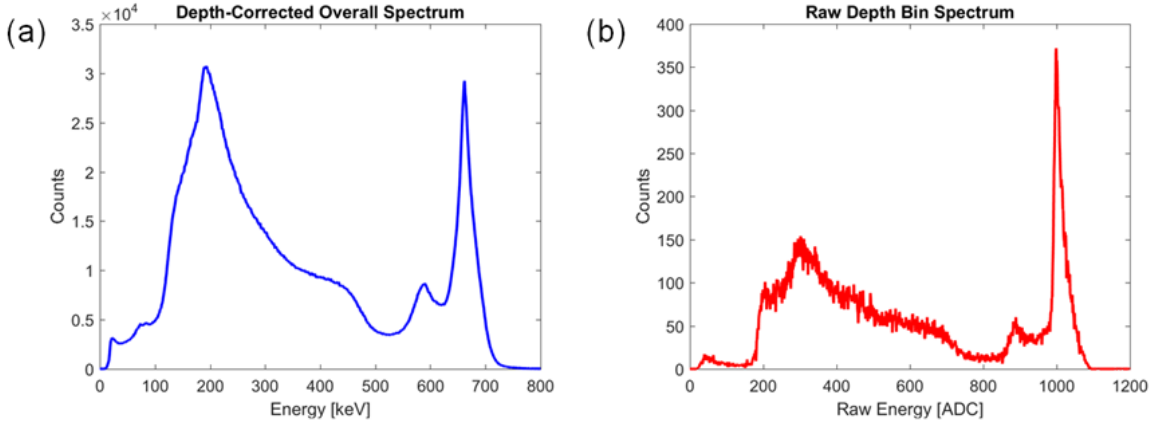


Figure 4.7: (a) Depth-corrected spectra for detector 935-38AA2L using simple subtraction to determine the pulse amplitudes showing the high-energy tailing on the photopeak and (b) raw spectrum in a single depth bin showing the high energy tail is present on the voxel level.

Similar high-energy tailing has been previously reported in mercuric-iodide ( $\text{HgI}_2$ ) [52]. Gerrish proposed that Auger recombination was responsible for this effect [53]. Auger recombination is the process where drifting holes can be trapped and in the process free additional electrons, increasing the overall signal.

In this work, I investigate the causes of this high-energy tailing by analyzing the digitized waveforms and conclude that there is strong evidence that the cause is charge multiplication by drifting holes.

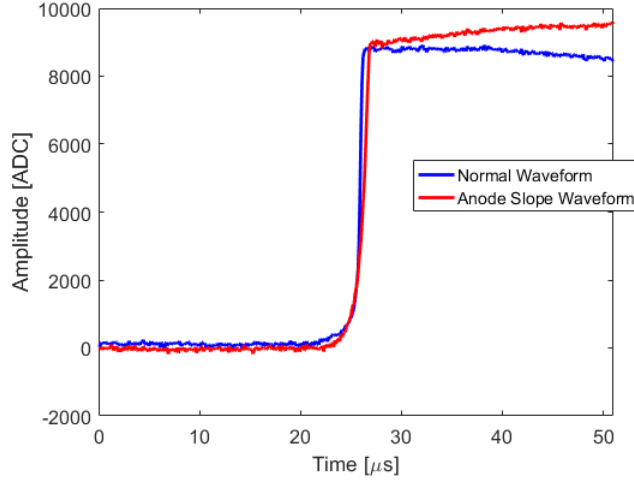


Figure 4.8: Comparison between a typical TlBr anode waveform (blue) and one showing an anode slope (red).

#### 4.2.1 Causes of High Energy Tails

The high-energy tails in the photopeaks are caused by slopes in the anode waveforms after the primary charge collection. Fig. 4.8 shows a comparison between a normal TlBr anode waveform sampled at 10 MHz and one demonstrating a positive anode slope. Typically anode waveforms show no rise after the primary charge collection and therefore have a flat tail. The first obvious explanation of this non-flat tail could be the motion of holes.

Sometimes cathode waveforms show a slope after electron collection which is due to hole motion. Fig. 4.9 shows an example of a typical (flat) cathode waveform and one with hole motion.

The tail in Fig. 4.9(b) looks similar to that in Fig. 4.8, however due to the different anode and cathode weighting potentials, the signal on the anode cannot be a result of hole motion. For events in most of the detector volume, the holes contribute very little signal to the anode. This is demonstrated in Fig. 4.10 for an event in the middle of the detector. Only holes which drift very near the anode contribute a significant amount of signal.

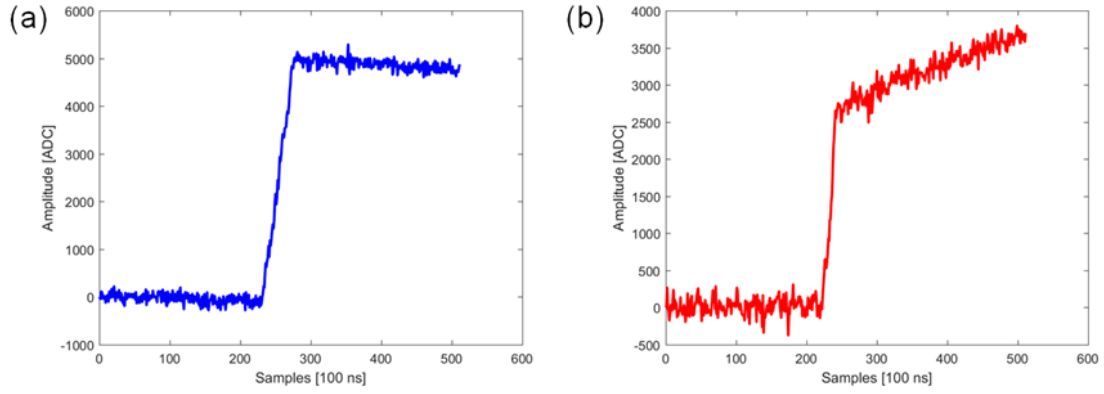


Figure 4.9: Comparison of (a) typical flat cathode waveform (blue) and (b) one showing hole motion (red).

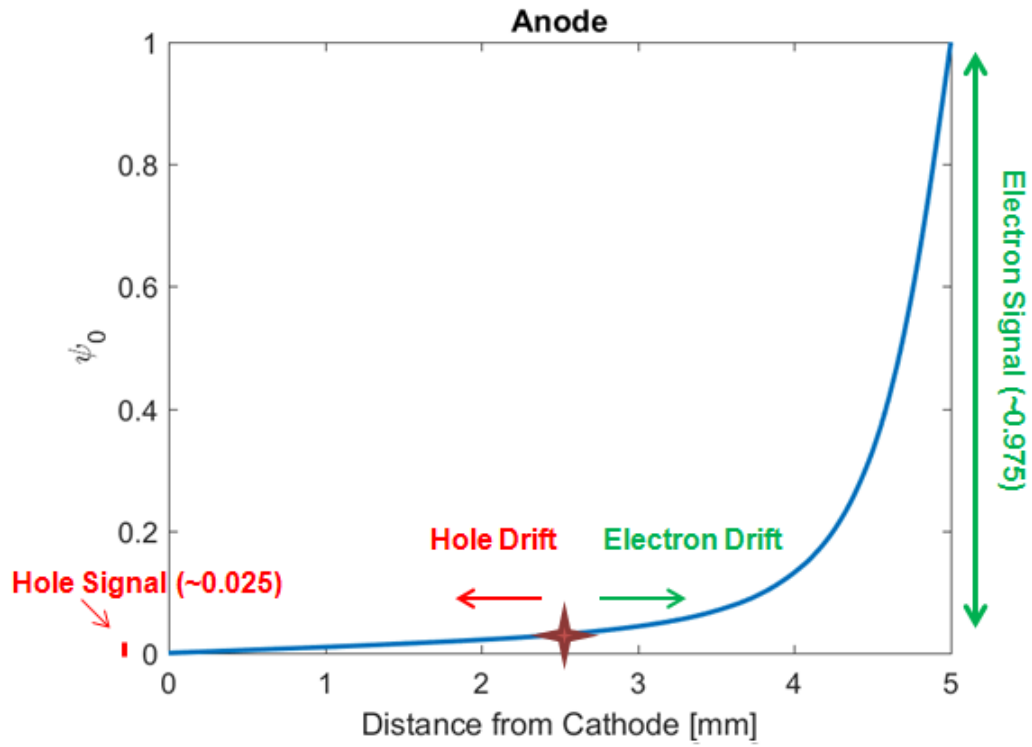


Figure 4.10: Anode weighting potential, demonstrating the small amount of signal holes contribute to the anode signal for an event in the middle of a 5 mm thick detector with a 1 mm pitch.

Non-zero anode slopes are both observed at all depths and are larger in magnitude than would be predicted at high depth by the weighting potential. Therefore the post primary electron-collection anode slopes cannot be signal induced by holes. This leaves as the only explanation that this signal is generated by electrons which arrive much later than the primary charge cloud.

The most obvious reason for electrons to be lagging behind the primary charge cloud is trapping and detrapping. That is, these electrons are from the primary event, but have been trapped out of the primary cloud and then released after some amount of time. If this were true, it would lead to the following predictions:

1. Integrating the charge in the tail would more faithfully recreate the charge generated by the gamma ray leading to better energy resolution.
2. The amount of extra charge would increase with electron drift distance (due to more opportunities for trapping and detrapping).
3. Increasing the bias would decrease this effect (lower overall electron trapping will lead to less detrapping).

Each of these predictions will be compared with the observed waveforms.

#### **4.2.2 Analysis Tools**

To analyze the anode slope waveforms two tools were developed: prompt subtraction and mean waveform generation.

##### **Prompt Subtraction**

Normally the amplitude of waveforms is determined by simple subtraction (see Section 3.3.2), but to investigate the effects of ignoring the waveform tail, the prompt subtraction method was developed.



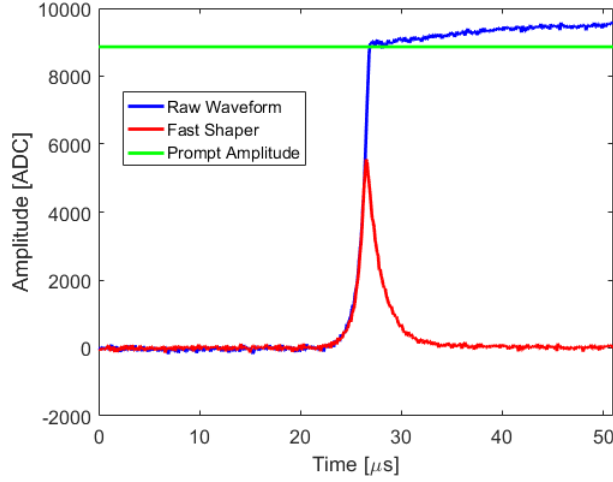


Figure 4.11: Example of prompt subtraction shaping. The raw waveform is shown in blue and the fast shaper is shown in red. The horizontal green line shows the amplitude determined from prompt subtraction.

In prompt subtraction, a fast shaper is applied to the waveform to find the turning point where the primary charge collection occurs. Then 15 points after this turning point are averaged to find the tail amplitude. The baseline amplitude (the average of the first 100 points) is then subtracted to find the amplitude. This is demonstrated in Fig 4.11.

As shown in Fig. 4.11, the prompt subtraction technique gets the amplitude without the tail, where simple subtraction would integrate all the charge in the tail as well. Notably, the prompt subtraction technique uses less points for the tail amplitude than simple subtraction and is therefore more affected by electronic noise.

### Mean Waveform Generation

To analyze the properties of the anode slope waveforms, the mean waveforms were generated. This allows for the analysis of the waveforms with lower noise and without waveform to waveform variation. The mean photopeak anode and cathode waveforms were generated for each pixel in multiple depth windows. The amplitude of each waveform was determined by prompt subtraction and the depth from CAR.

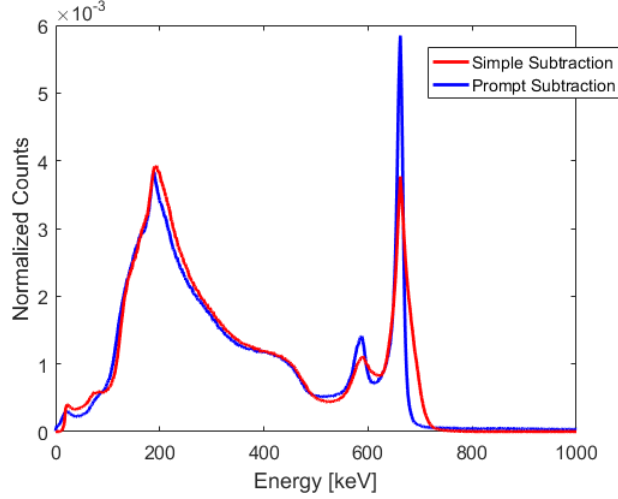


Figure 4.12: Depth-corrected spectra for detector 935-38AA2L using both simple subtraction (red) and prompt subtraction (blue) to determine the pulse amplitude. With the removal of the tail, the resolution improves from 4.59% FWHM at 662 keV to 2.21%.

Each anode and cathode waveform was then normalized by its corresponding anode amplitude, and all waveforms in a CAR bin were averaged.

#### 4.2.3 Analysis of Detrapping Hypothesis

Fig. 4.12 shows a comparison of the depth-corrected single-pixel spectrum when the amplitude is determined by simple subtraction and the prompt subtraction method. The photopeak has a large high-energy tail when simple subtraction is used, but it is removed with prompt subtraction.

When the prompt subtraction technique is used, the charge in the tail of the waveform is ignored and the resolution improves. This directly contradicts prediction 1 of the detrapping hypothesis. Furthermore, the noise has a higher impact on the prompt subtraction amplitude, so the improvement of the resolution despite the increase in noise is also unexpected. This seems to indicate the signal in the tail of the anode waveform is from charge not from the primary event, but generated by some other process during the drift of electrons and holes.

Fig. 4.13 shows the average (a) anode and (b) cathode waveforms for the cathode

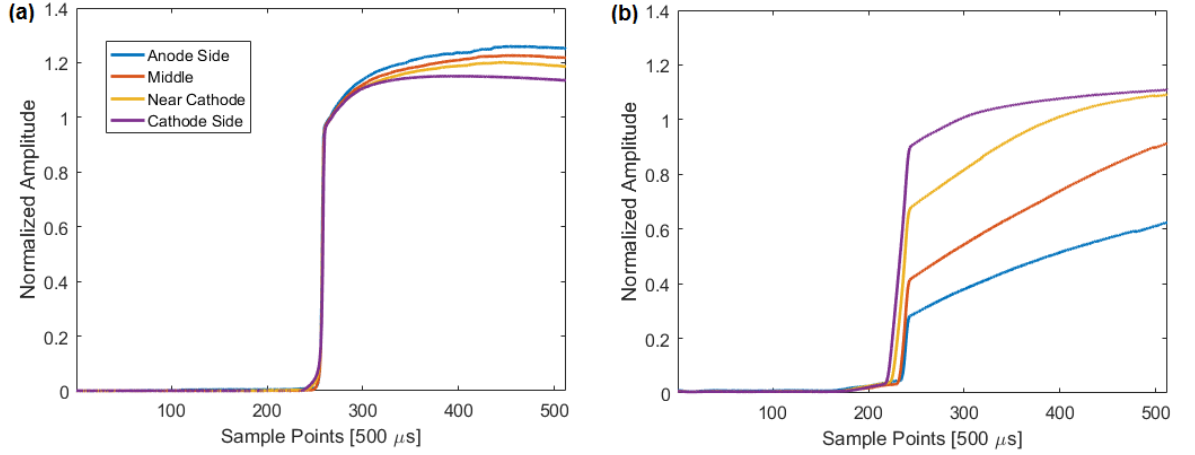


Figure 4.13: Mean (a) anode and (b) cathode waveforms for the cathode side, near cathode side, middle, and anode side of detector 935-38AA2L at 1000 V and 2 MHz.

side ( $0.9 < \text{CAR} < 1.0$ ), near cathode side ( $0.7 < \text{CAR} < 0.85$ ), middle ( $0.45 < \text{CAR} < 0.55$ ), and anode side ( $0.25 < \text{CAR} < 0.35$ ) of the detector at 2 MHz sampling. Each waveform has been corrected for preamplifier decay as discussed in Section 3.4.

In this time window, the full anode charge is collected, but the full cathode signal is only collected in the larger two depth ranges. As shown in Fig. 4.13(a), the relative amount of charge in the anode tail increases towards the anode side. This contradicts prediction 2 of the detrapping hypothesis.

Fig. 4.14 shows a comparison of the average waveforms from the middle of the detector at two different biases (-800V and -1000V). At the higher bias, there is relatively more charge in the anode tail. This contradicts prediction 3 of the detrapping hypothesis.

From the results shown in Figs. 4.12 - 4.14, the detrapping hypothesis can be rejected. This leaves the hypothesis that the charge in the anode tail is extra charge generated not from the primary photoelectron slowing down process, but during the drift of the carriers. This extra charge could be generated by either the drift of electrons or holes.

If this extra charge was generated by the drift of the electrons by some other

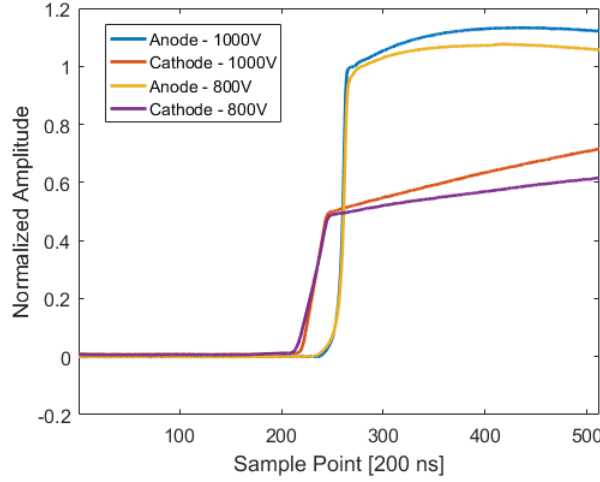


Figure 4.14: Comparison of the average waveforms from the middle of the detector at two different biases.

mechanism than trapping, it would likely increase with increasing electron drift distance. This was not observed. Instead, the amount of extra charge increases with increasing hole drift distance, as the amount of extra charge increases towards the anode side in Fig. 4.13. This is also shown by the increase with increasing bias, as this also increase the distance traveled by holes in the collection time.

Therefore, the most consistent explanation for the observed waveform tails is extra charge which originates from holes generating electrons as they drift towards the cathode. Physically this could be caused by Auger recombination as proposed by Gerrish for explaining a similar behavior in  $\text{HgI}_2$  [53].

#### 4.2.4 Quantification of Extra Charge

Investigation of the characteristics of the anode tails shows that it is likely the drift of holes giving rise to the extra charge, but does not indicate whether the hole must be trapped to free an electron, or if one hole can produce multiple extra electrons. Quantitative investigation of the extra charge can be used to address this question.

The final cathode amplitude is the sum of the signal induced by the electrons,

holes, and the extra charge, or

$$C_T = Q_0 + C_{extra} = C_{electron} + C_{hole} + C_{extra} \quad (4.13)$$

where  $Q_0$  is the initial charge created by the gamma ray, assuming the trapping is negligible. The electron component of the cathode signal is the normalized depth times the initial charge.

$$C_{electron} = \frac{Z}{D} Q_0 \quad (4.14)$$

Where  $Z$  is the depth of interaction and  $D$  is the detector thickness. The electron component of the cathode waveform can be estimated using the prompt subtraction shaping method, and from this the signal generated on the cathode by the extra charge can be estimated.

$$C_{extra} = C_T - \frac{D}{Z} C_{electron} \approx C_T - \frac{D}{Z} C_{prompt} \quad (4.15)$$

Where  $C_{prompt}$  is the cathode amplitude calculated by prompt subtraction. Since trapping has been neglected, this should be seen as a conservative estimate of the extra charge. The true value of the extra charge would be this estimate plus the amount of trapping.

The signal from the extra charge on the anode can similarly be estimated by subtracting the prompt-shaped amplitude from the final anode amplitude,  $A_F$ .

$$A_{extra} = A_F - A_{prompt} \quad (4.16)$$

Table 4.5 shows the estimated signal from the extra charge on both the anode and cathode for the two fully collected cathode waveforms from Fig. 4.13. As demonstrated in Section 4.2.3, the amount of extra charge decreases with increasing electron drift distance (see Fig. 4.13). Also, the extra signal on the cathode is less than the

Table 4.5: Estimated signal from extra charge on anode and cathode

CAR Range	Mean Z/D	$C_T$	$C_{prompt}$	Extra Charge	
				$C_{extra}$	$A_{extra}$
0.9-1.03	0.965	1.083	0.942	0.107	0.156
0.7-0.85	0.775	1.067	0.704	0.158	0.239

Table 4.6: Comparison of estimated and measured cathode signal from extra charge

CAR Range	Measured	Predicted		Measured
	$A_{extra}$	$C_{extra1}$	$C_{extra2}$	$C_{extra}$
0.9-1.03	0.159(25)	0.153(24)	0.156(12)	0.133(27)
0.7-0.85	0.218(40)	0.169(31)	0.194(20)	0.175(43)

extra signal on the anode. This is expected as the cathode extra charge can be expressed as the average drift distance times the anode extra charge.

$$C_{extra} \approx \frac{\bar{Z}}{D} A_{extra} \quad (4.17)$$

Where  $\bar{Z}$  is the mean depth at which the extra charge is generated. Table 4.6 shows a comparison of the measured cathode extra charge to the predicted cathode extra charge (calculated using Eq. 4.17) under two different assumptions.

$C_{extra1}$  assumes the extra charge is generated at the same location as the primary charge and  $C_{extra2}$  assumes the charge is generated uniformly along the drift of the holes towards the cathode.  $C_{extra1}$  can be viewed as a minimum signal induction on the cathode by the extra charge. This is because electrons generated by holes at the primary interaction location have the shortest drift path to the anode and therefore induce the least amount of signal.  $C_{extra2}$  takes the mean generation depth to be the average of the primary interaction position and the cathode surface. This represents a reasonable upper bound for the drift distance (and thus the induced signal) of the extra charge.

The measured and predicted values for  $C_{extra}$  do not differ beyond uncertainty. Due to the high uncertainty in these values, no conclusion can be made about which

charge generation model is more appropriate. Without knowledge of the correct charge generation model we cannot conclude whether the holes have to be trapped to free an electron, or if one hole can generate more than one electron.

#### 4.2.5 Positive Bias

To determine if holes have to be trapped in order to free an electron (thus requiring a one to one conversion) the hole trapping was estimated by operating the detector in positive bias.

Under positive bias, the holes drift towards the pixelated electrode. With the holes drifting to the pixelated electrode, the depth cannot be reconstructed by the classic CAR. This is because the electrons are collected before the holes and the planar electrode waveform always shows full charge collection when the pixelated electrode triggers. This results in the CAR to be 1 for all waveforms.

Fig. 4.15 shows an example planar electrode waveform under positive bias. The planar electrode has contributions from both electrons and holes, with the initial fast rise due to electrons. Prompt subtraction was used to estimate the electron-only component of the planar electrode waveform, so that the depth could be estimated using a modified CAR. Since the electron component of the planar waveform is analogous to the cathode waveform in the regular (negative bias) case, the depth can be calculated using Eq. 4.18.

$$\frac{Z}{D} = \frac{\textit{Electron Planar Component}}{\textit{Pixelated Amplitude}} \quad (4.18)$$

Fig. 4.16 shows the pixelated amplitude (hole signal) versus drift distance as calculated by Eq. 4.18. The expected signal amplitude,  $N$ , versus depth is given by Eq. 4.19.

$$N = N_0 e^{-\mu\tau z/E} \quad (4.19)$$

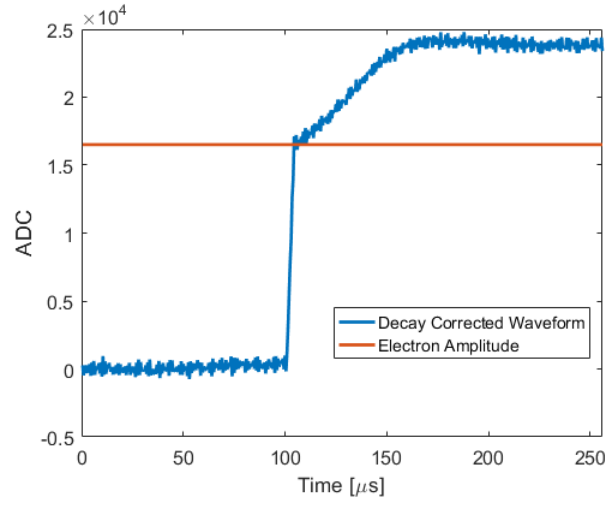


Figure 4.15: Planar electrode waveform in positive bias (+2000V), with the red line showing the amplitude from electrons determined by prompt subtraction.

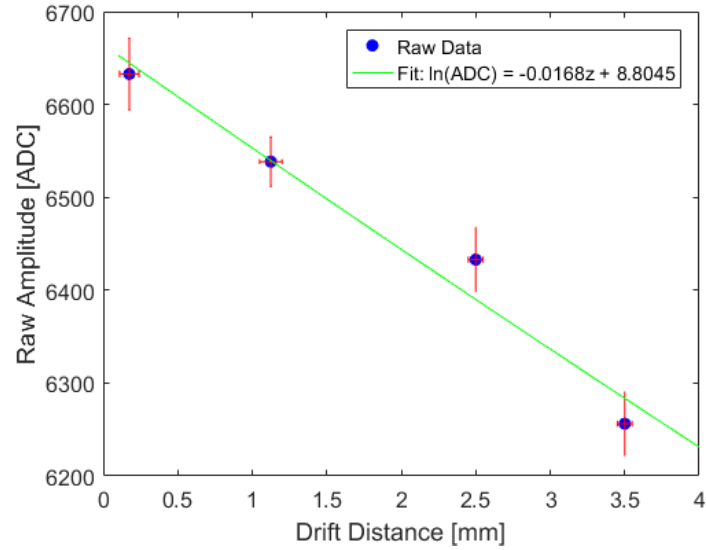


Figure 4.16: Trapping on planar electrode (holes) in reverse bias (+2000V) with an exponential fit.



Table 4.7: Comparison of estimated hole trapping and anode extra charge

CAR Range	<u>Relative</u>	
	Predicted Hole Trapping	Anode Extra Charge
0.9-1.03	0.003	0.156
0.7-0.85	0.0187	0.239

where  $N_0$  is the initial number of carriers,  $\mu\tau$  is the mobility-lifetime product of holes in the detector, and  $E$  is the electric field.

The data is fit using Eq. 4.19 and the  $(\mu\tau)_h$  was estimated to be  $1.49 \times 10^{-3} \text{ cm}^2/(\text{Vs})$ . Using this estimate of the  $(\mu\tau)_h$ , the trapping of holes in the fully collected waveforms from Fig. 4.13 can be estimated.

Table 4.7 shows a comparison of this estimated hole trapping with observed anode extra charge (from Table 4.5). The amount of anode extra charge is significantly higher than the number of trapped holes, so not enough holes are trapped to account for the amount of extra charge observed on a one-for-one basis. Therefore it must not be necessary for the hole to be trapped in order to free an electron.

#### 4.2.6 Conclusions

Delayed charge collection has been observed on anode waveforms in some TlBr detectors resulting in high-energy tails on photopeaks. Through digital signal processing, this delayed charge can be ignored and the detector performance improves, indicating this charge is not from the primary gamma ray interaction. The amount of observed extra charge is correlated to hole drift distance and is therefore likely generated from the drift of holes.

By operating the detector in reverse bias, the  $(\mu\tau)_h$  was estimated. The amount of hole trapping is significantly less than the amount of observed extra charge on the anode, therefore it is likely that the holes can generate extra electrons through drifting without requiring trapping. Auger recombination is a poor explanation for the physical mechanism because it only accounts for extra charge on a one-for-one

Table 4.8: Performance of TlBr arrays over time

Detector Name	Best Day Resolution [%FWHM at 662 keV]	Testing Date
935-16B1R	0.97%	May 2011
	2.25%	August 2013
	2.80%	March 2014
	4.23%	December 2015
935-16B1L	1.42%	July 2014
	1.64%	August 2014
	1.96%	September 2015
58A3L	1.62%	July 2013
	1.64%	September 2013
	1.46%	December 2013
	4.13%	October 2015
935-38AA1R	1.74%	November 2014
	1.99%	September 2015
935-35AA1R	1.69%	September 2014
	2.47%	December 2014
	3.10%	September 2015

basis, therefore, the exact mechanism for this release of extra charge is unknown at this time. This extra charge generation is limited to only a few TlBr detectors and consequently is likely caused by impurities rather than intrinsic material properties.

### 4.3 Storage Effects

Through the testing of multiple detectors over many years, it was observed that many TlBr detectors degrade from storage. Table 4.8 shows the energy resolution and testing date for many TlBr detectors. All data sets were processed with simple subtraction and the reported resolution is the best day at  $-20^{\circ}\text{C}$  and -1000 V.

This degradation appears to be caused by storage and not operation at  $-20^{\circ}\text{C}$ . Figure 4.17 shows the energy resolution for each bias of detector 58A3L versus the time since the first testing. The performance did not degrade over multiple biases in 2013, but degraded between 2014 and 2015 when the detector was not tested. This indicates that it is the storage of the detectors which cause the degraded performance,

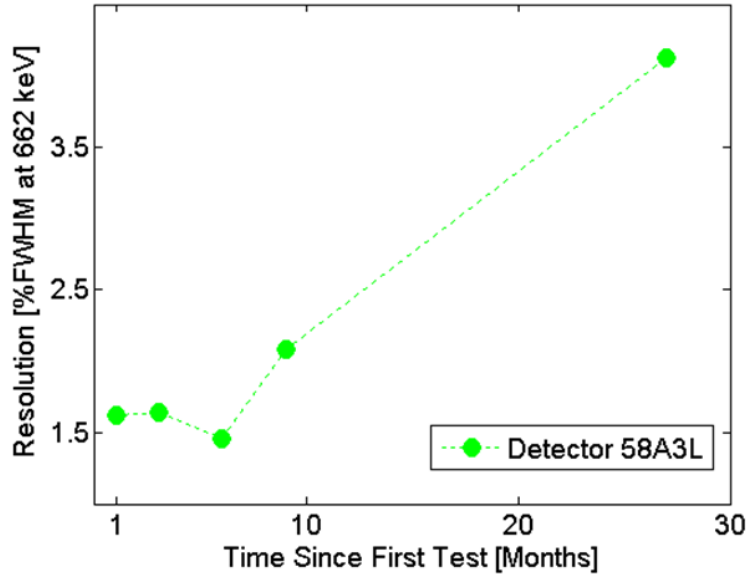


Figure 4.17: Resolution for each testing for detector 58A3L showing the degradation with storage time.

not the operation at  $-20^{\circ}\text{C}$ . When not under bias, the TlBr detectors are stored in a desiccator at room temperature with regularly changed desiccant.

#### 4.3.1 Cause: Surface Effect

Figure 4.18 shows the energy resolution versus depth for multiple testings of detector 935-16B1L. The overall energy resolution degrades from 1.42% in July 2014 (black) to 1.96% in September 2015 (red), and this degradation appears to be uniform in depth, implying that the degradation is caused by a surface effect.

Bulk effects have an increasing effect with electron drift distance and therefore generally show worsening performance towards the cathode side. Surface effects, however, effect all depths the same and therefore have a uniform effect with depth like that shown in Fig 4.18.

Additionally, detector 935-16B1L shows very little trapping even in the worse (September 2015) testing. This is shown in Fig. 4.19 where the photopeak centroid does not decrease towards the cathode side. This further confirms that the degra-

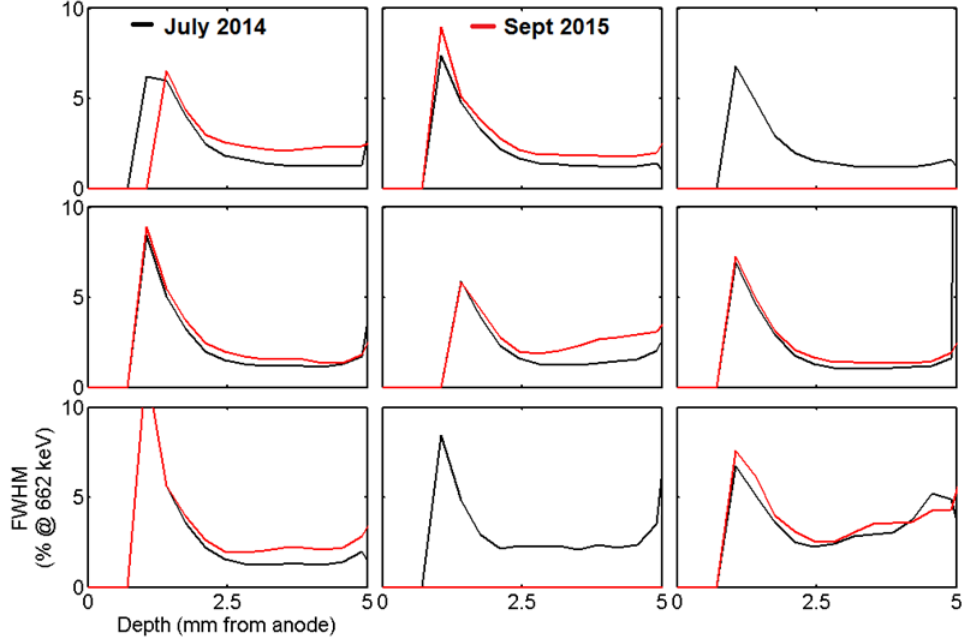


Figure 4.18: Resolution (%FWHM at 662 keV) versus depth for two testings of detector 935-16B1L.

dation which occurred between July 2014 and September 2015 was due to a surface effect.

Unlike with polarization, where there is a visible change to the contact; no change can be observed on the surface of these detectors with the naked eye. It is likely that some chemical reaction has occurred (possibly oxidation) which has caused this degradation in performance, but the exact cause is unknown.

#### 4.3.2 Refabrication

Five degraded TlBr detectors were refabricated; that is, their electrodes were removed, they were re-etched and new electrodes were deposited. Their performance after refabrication is summarized in Table 4.9. Four detectors showed improved energy resolution compared with their last testing before refabrication. This confirms the observation that the degradation is a surface effect, as the refabrication has no effect on the bulk and establishes that refabrication is an effective way to mitigate the

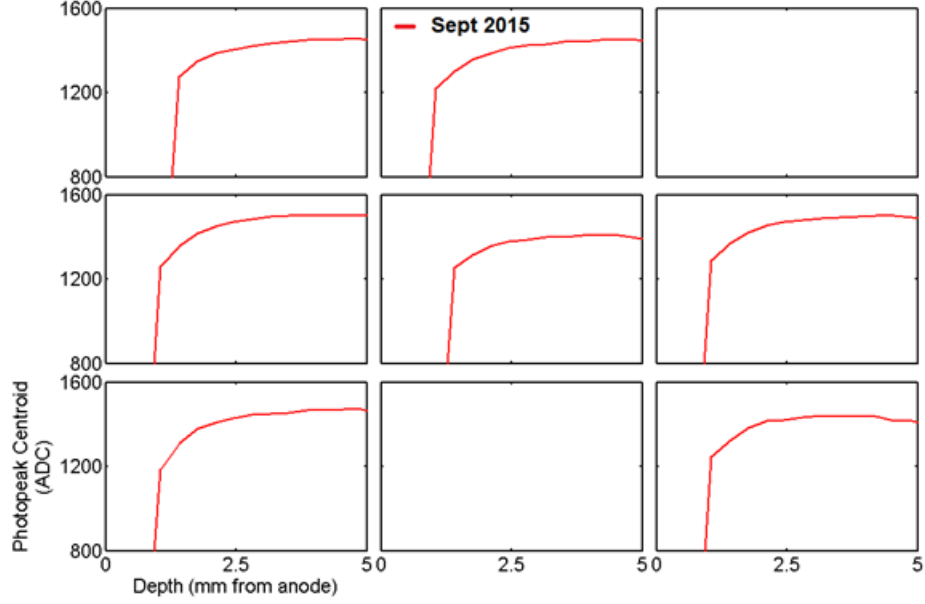


Figure 4.19: Photopeak centroid versus depth for the September 2015 testing of detector 935-16B1L. The photopeak centroids do not decrease towards the cathode side indicating very low trapping.

observed degradation.

Figure 4.20 shows the energy resolution versus time for each testing of detector 935-38AA1R which did not show improved energy resolution after refabrication. This detector is from newer material which is optimized for room temperature performance. These detectors do not condition at  $-20^{\circ}\text{C}$ ; they instead get worse with time when cooled. As shown in Fig. 4.20, the degradation from storage in detector 935-38AA1R manifested as a quickening of this worsening processes at  $-20^{\circ}\text{C}$ . Originally (in November 2014), the detector operated for 20 days with performance of around 3% FWHM at 662 keV, but after approximately one year of storage it was worse than 3% within the first five days of operation. After refabrication, the performance again was better than 3% over 20 days of testing. Since after refabrication detector 935-38AA1R showed improvement in the form of a slowed worsening process, all five detectors showed improvement from refabrication.

After refabrication, detector 935-38AA1R still got worse with time (indicating this

Table 4.9: Refabricated performance of TlBr detectors

Detector Name	Rebfabricated Resolution (% FWHM at 662 keV)	Old Resolution (% FWHM at 662 keV)
935-16B1R	1.68%	4.23%
935-16B1L	1.70%	1.96%
58A3L	1.55%	4.13%
935-38AA1R	2.64%	1.99%
935-35AA1R	1.74%	3.10%

is an intrinsic material property), but the rate was reduced to similar to its original performance. This indicates the rate of worsening is affected by the surface status which should be investigated further.

### 4.3.3 Conclusions

TlBr detectors degraded from storage in desiccators at room temperature. This degradation is caused by a surface effect that can be mitigated by refabrication. It is likely that it is caused by oxidation or some other chemical reaction with the air (it is unlikely due to water, because the detectors were stored with regularly changed desiccant). Investigating sealants to protect the detector from the air is crucial to having stable high-performance TlBr detectors, though using current fabrication techniques, detectors can achieve good performance through regular refabrication.

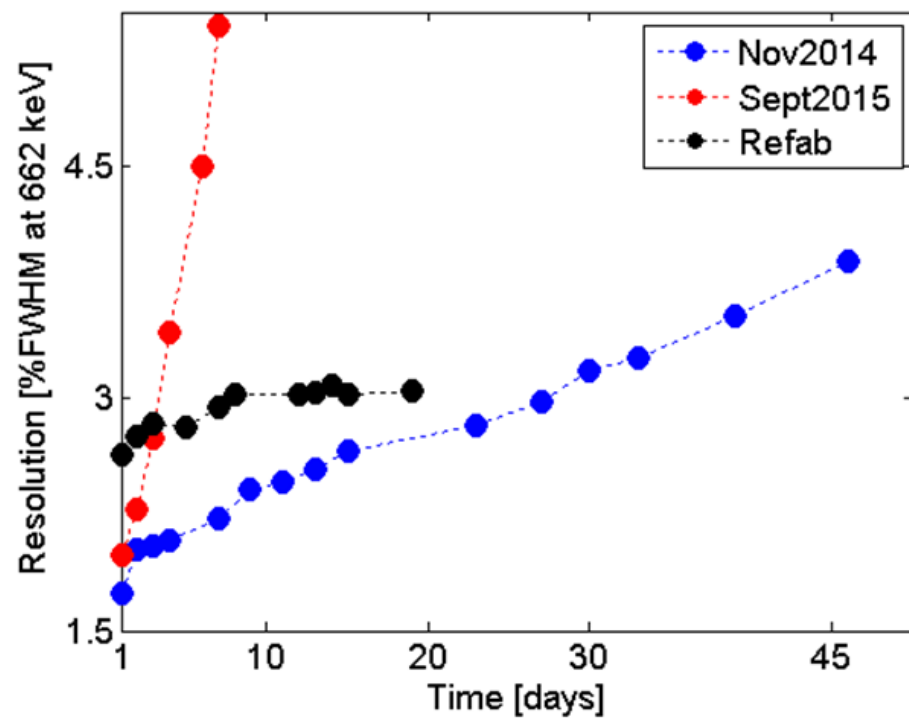


Figure 4.20: Energy resolution versus time for each testing of detector 935-38AA1R at  $-20^{\circ}\text{C}$ .

## CHAPTER V

### Extending Detector Lifetime

Achieving a long lifetime, or operational time before polarization, in TlBr detectors is a major focus of TlBr development. The room-temperature lifetime of TlBr detectors have been varied, but generally short. Table 5.1 shows the lifetimes of four typical TlBr detectors, all older material and using the standard fabrication technique. The lifetimes for these detectors range from four days to three months, with most detectors having lifetimes under two weeks.

Detector 47AR(R) previously held the record for the longest room-temperature lifetime and in years of testing multiple detectors, no detector had come close to this lifetime. Though this lifetime is much better than others, field deployable detectors require both longer lifetimes and more reliability in the detector lifetime.

Fundamentally, the polarization process is driven by ionic conduction [24], though device failure is due to degradation of the contacts as shown by Koehler [25]. This leads to two different approaches for mitigating polarization: limiting the ionic con-

Table 5.1: Example room-temperature lifetime of TlBr detectors

Detector	Lifetime
935-35AA1L	4 days
935-34AA1L	11 days
935-29AA1-3	15 days
47AR(R)	3 months



duction and slowing the interactions between vacancies and the contact. Both approaches are considered in this work.

## 5.1 Ionic Conduction Mitigation (2 °C Operation)

### 5.1.1 Leakage Current and Lifetime

The leakage current in TlBr has two components: thermal leakage and ionic conduction. The thermal leakage in a semiconductor depends on its band gap energy ( $E_{gap}$ ) and the temperature. Eq. 5.1 shows the probability of thermal carrier generation (proportional to the thermal leakage current) versus the temperature [1].

$$p = CT^{3/2}e^{-\frac{E_g}{2k_bT}} \quad (5.1)$$

Where  $T$  is the temperature,  $k_b$  is the Boltzman constant, and  $C$  is a proportionality constant which depends on the electron mobility and effective mass in the material. Since the bandgap of TlBr is so large (2.68 eV) compared to room temperature ( $k_bT = 0.025$  eV at 20 °C), the exponential term is quite small, therefore the thermal component of the leakage current is small. This means that ionic conduction makes a significant contribution to the leakage current, suggesting a correlation between the leakage current and polarization.

Fig 5.1 shows the leakage current versus time for a typical anode pixel in detector 935-34AA1L during polarization. As shown in Fig. 5.1, it is very typical for the leakage current to dramatically increase as the device nears failure. This confirms the correlation between leakage current and polarization implying that reducing the leakage current will reduce ionic conduction and therefore slow polarization.

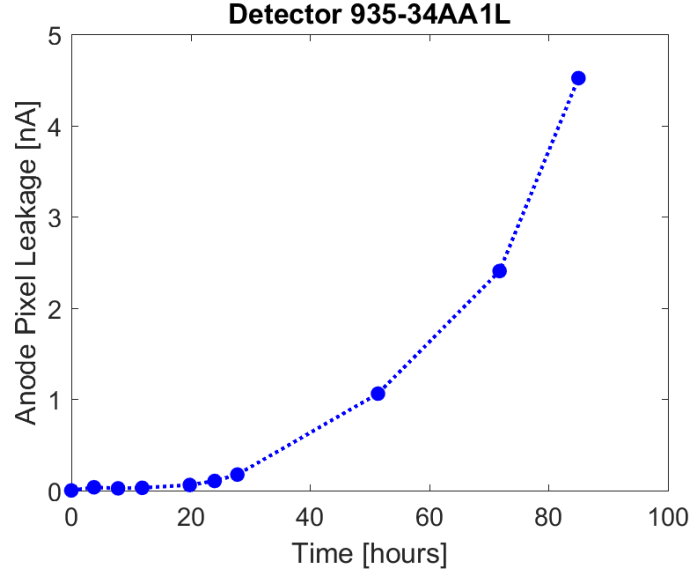


Figure 5.1: Leakage current versus time for one anode pixel of detector 935-34AA1L during polarization, showing the increase as the device fails.

### 5.1.2 Leakage and Temperature

Fig. 5.2 shows the leakage current from detector 935-29AA1-3 versus temperature from  $-20^{\circ}\text{C}$  to  $20^{\circ}\text{C}$ . The leakage current stays very low until around  $0^{\circ}\text{C}$ , and then begins to increase dramatically. Assuming the leakage current and lifetime are inversely proportional, this would predict a lifetime more than 50 times greater at  $-20^{\circ}\text{C}$  than at room-temperature. This has been previously reported [26]. Functionally infinite lifetimes have been observed at  $-20^{\circ}\text{C}$ , though no significant testing has been done at time greater than 3 months.

Since the leakage current does not dramatically increase until above  $0^{\circ}\text{C}$ , this would predict that TlBr detectors do not need to operate as low as  $-20^{\circ}\text{C}$  in order to achieve very long lifetimes. Historically,  $-20^{\circ}\text{C}$  was chosen somewhat arbitrarily because it was the temperature a deep freezer was capable of achieving. Operation at a higher temperature is desirable for limiting the time required to cool the system down and the cooling power required (see Fig. 6.5, where raising the operating temperature to  $0^{\circ}\text{C}$  reduces the cooling power required by  $\sim 6$  times).

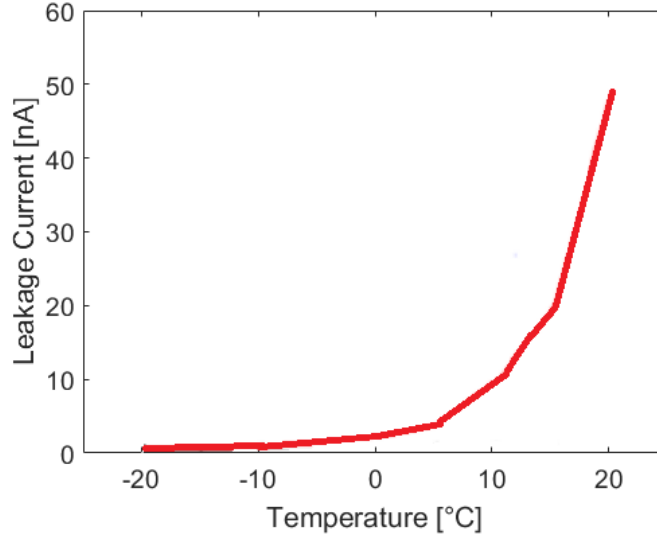


Figure 5.2: Leakage current versus temperature for detector 935-29AA1-3.

Ultimately, true room-temperature (or even higher than room-temperature) operation is desirable, but if stable operation can be achieved closer to room temperature, this can be very beneficial to the field deployability of systems. For this study, 2 °C operation was chosen to keep the detectors above freezing in an attempt to limit ice formation from condensation in the system.

### 5.1.3 Detectors and Experimental Design

To test the performance of TlBr detectors at 2 °C, two measurements were performed. The first was with two newly fabricated detectors from beside each other in a boule in an attempt to check for conditioning at 2 °C, controlling for any effects from −20 °C operation prior to testing at 2 °C. These two detectors are 935-43BA1L and 935-43BA1R which operated at 2 °C and −20 °C, respectively. Though material variation in TlBr is wide, previous work has shown detectors from beside each other in boules do perform similarly, especially in the case of detectors 935-16B1L and 935-16B1R which both showed very good performance.

The second measurement was a long-term test of a single detector (935-16B1L)

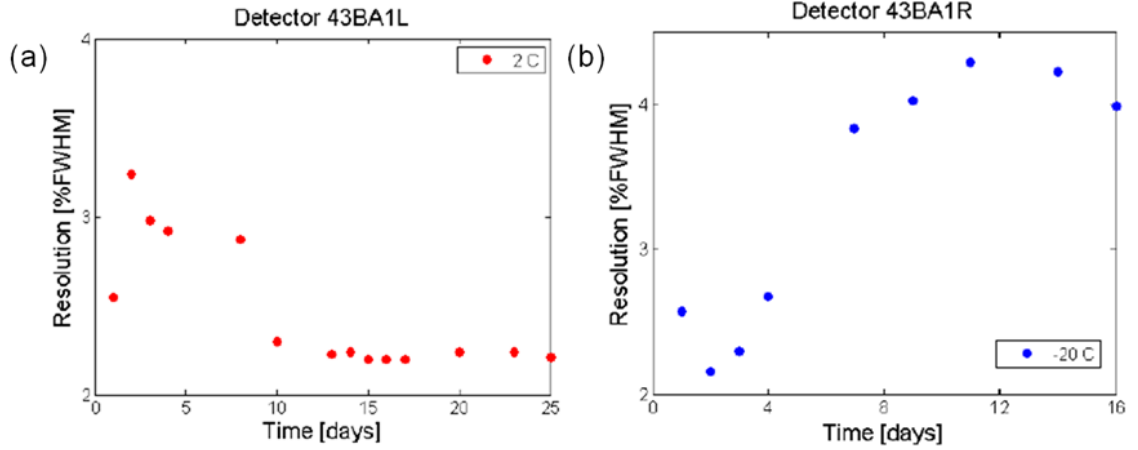


Figure 5.3: Depth-corrected single-pixel energy resolution versus time for detectors (a) 935-43BA1L at 2°C and (b) 935-43BA1R at -20°C.

where the detector first operated at -20°C, was raised to 2°C for a time, and then cooled again in an attempt to check for damage or any other signs of polarization.

All three detectors used in these measurements were fabricated using the standard process.

#### 5.1.4 Results: Detector Pair

Fig. 5.3 shows the energy resolution versus time for the two detectors 935-43BA1L and 935-43BA1R at 2°C and -20°C respectively. Detector 935-43BA1L showed an initial worsening of performance before improving to ~2.2% FWHM at 662 keV where it stayed stable until the end of the measurement (26 days).

Detector 935-43BA1R, on the other hand, showed a slow worsening with time over most its operation, with its worst performance coming on day 11. After this, it improved slightly. The worst day performances of the two detectors are comparable at ~3.5% FWHM for detector 935-43BA1L and ~4.3% FWHM for detector 935-43BA1R, and they both started with similar performance of ~2.5%. It is possible that with a much longer testing time, the performance of detector 935-43BA1R could have improved to a similar level as 935-43BA1L, but this likely would have taken more than 50 days based on the time it took each to reach their worst day.

Fig. 5.4 shows a comparison of the photopeak centroids versus depth for different days between the two detectors. Detector 935-43BA1R shows monotonically increasing trapping (decreasing cathode-side amplitude) which is expected during its worsening performance. Detector 935-43BA1L shows an initial worsening (from red to magenta) then some moderate improvement in trapping, which is similar to its performance in energy resolution. This corroborates the idea that these two detectors are undergoing the same processes but at different rates due to the different temperatures.

Detector 935-43BA1R is one of the newer detectors which do not condition the same at  $-20^{\circ}\text{C}$  as older detectors. These devices have been optimized for room-temperature performance. Generally these detectors get worse with time at  $-20^{\circ}\text{C}$ , but, as shown in Fig. 5.3(b), the resolution does start to improve near the end of the measurement. This and the behavior of detector 935-43BA1L indicate that detector 935-43BA1R may still be conditioning but at a much slower rate.

The older material generally showed high instability on the first day of operation, but then improved over the course of the next few days. The instability on the first day could encompass this worsening observed in newer material and the later improvement is not observed in cooled operation because of how much longer the process takes. However, at  $2^{\circ}\text{C}$ , the conditioning process is faster and can be observed as it is in detector 935-43BA1L.

Since the newer material has a longer room-temperature lifetime, this would imply a correlation between polarization and conditioning rates. These two effects seem very different, but a relationship between them is not entirely unexpected. Koehler demonstrated that the conditioning phase is a result of the drift of charged impurities in the detector [27] and polarization is due to the drift of components of the lattice. Therefore any mechanism which reduces the mobility of large ions or vacancies in the detector will slow the rate of both processes. This has the double sided effect

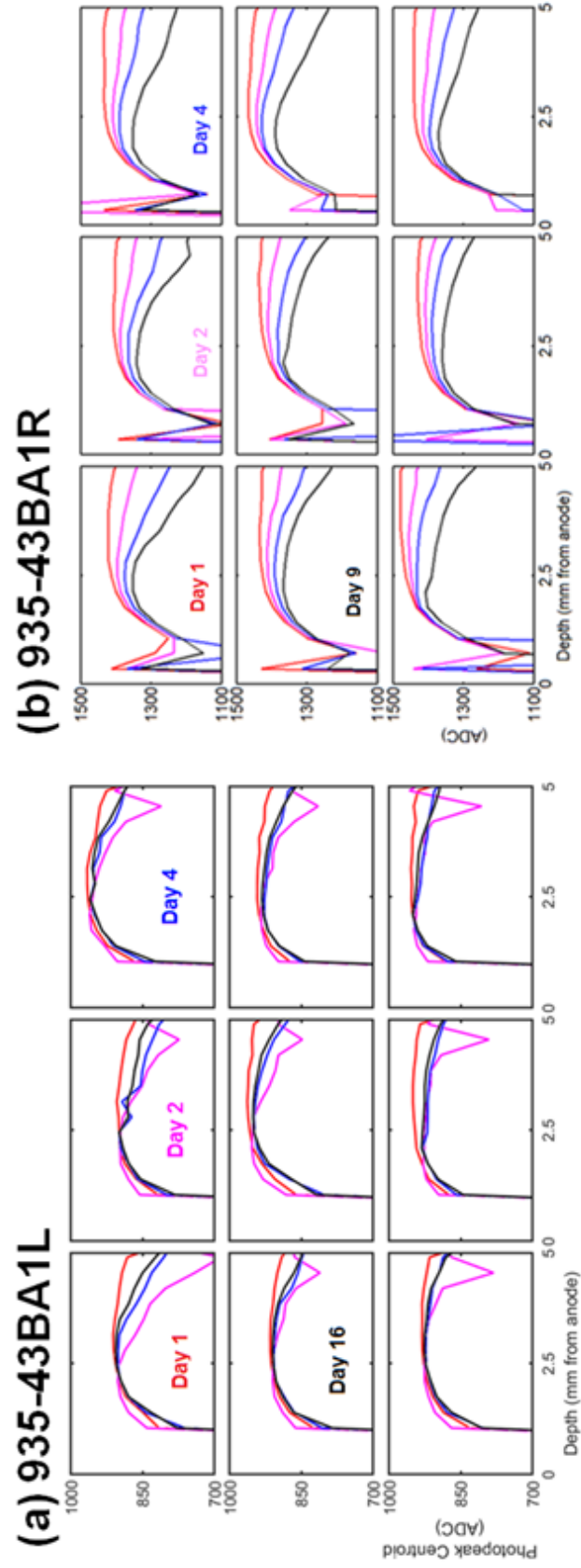


Figure 5.4: Comparison of the photopeak centroids versus depth for detector (a) 935-43BA1L at 2 °C and (b) 935-43BA1R at -20 °C

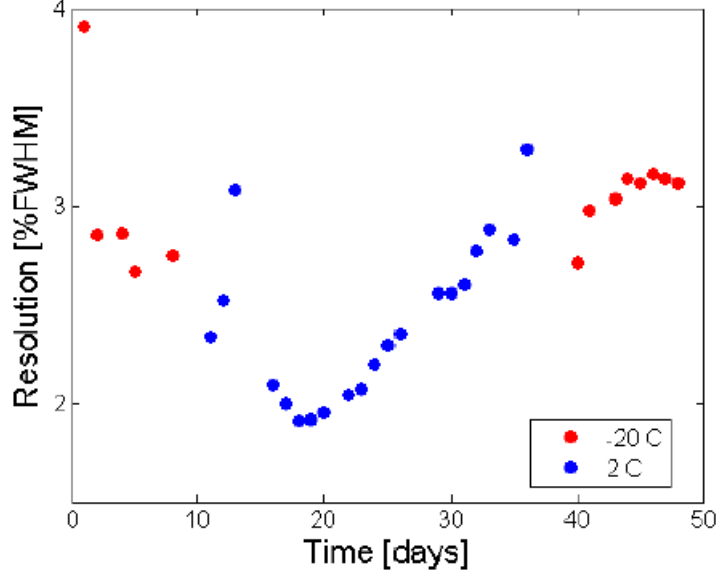


Figure 5.5: Resolution versus time for detector 935-16B1R at both  $-20^{\circ}\text{C}$  and  $2^{\circ}\text{C}$ . After 43 total days of testing, the device polarized in less than one day at room temperature.

of increasing the lifetime, but creating a long “burn-in” period before the device can achieve its best performance.

### 5.1.5 Results: Long-term Operation

Fig. 5.5 shows the resolution versus time for detector 935-16B1R. The detector operated initially at  $-20^{\circ}\text{C}$  for 8 days to establish a baseline performance. Then at  $2^{\circ}\text{C}$  for 26 days to check for stability at this temperature. Then back at  $-20^{\circ}\text{C}$  for 9 days to check for degradation from the  $2^{\circ}\text{C}$  operation. Finally, the detector operated at room temperature for less than one day (about 18 hours) before polarization.

Detector 935-16B1R shows initial conditioning at  $-20^{\circ}\text{C}$  where it achieved a best resolution of 2.7% FWHM. At  $2^{\circ}\text{C}$ , the performance initially improved, but then began to degrade. In the second testing at  $-20^{\circ}\text{C}$ , the performance stabilized at 3.1% FWHM, worse than the initial performance, suggesting the  $2^{\circ}\text{C}$  operation may have damaged the detector.

Fig. 5.6 shows the photopeak resolution versus depth from two characteristic

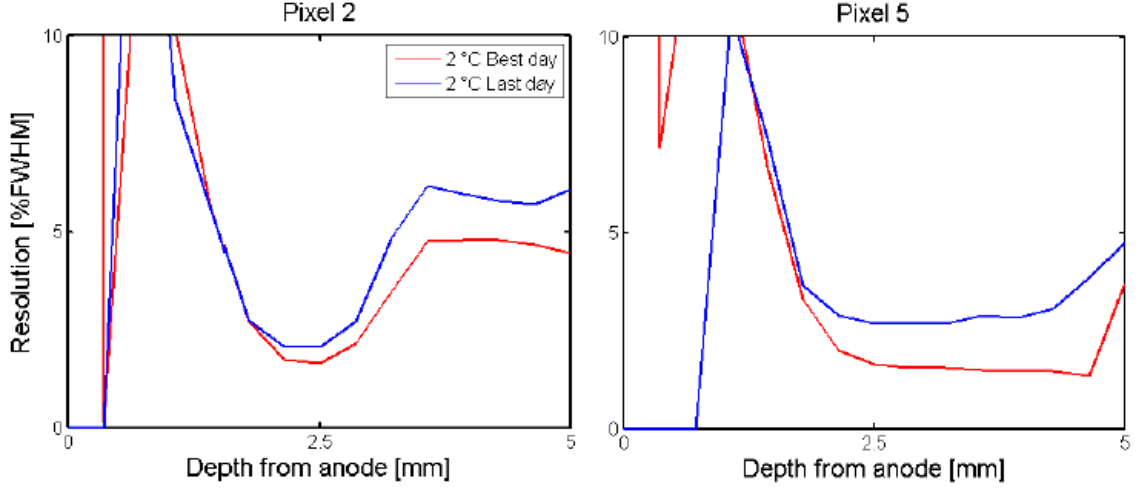


Figure 5.6: Resolution versus depth for two characteristic pixels of detector 935-16B1R comparing the performance on the best and worst day at 2 °C.

pixels comparing the performance on the best and worst (last) days at 2 °C. Pixel 2 shows a characteristic bad region at  $\sim 3.5$  mm from the anode where the performance gets significantly worse. This is indicative of a material problem and demonstrates the power of the 3D depth-sensing technique at identifying and localizing these bad regions in detectors.

Both pixels show a relatively systematic degradation in resolution with depth after 2 °C operation. This implies that the degradation is dominated by an anode side effect as the shape (including the bad region in pixel 2) is mostly preserved. Polarization is an anode effect, so this type of degradation would be expected if polarization has begun.

Fig. 5.7 shows the drift velocity versus depth for the two pixels from Fig. 5.6. The drift velocity is determined from an average cathode waveform as described in Ref [54]. During the time at 2 °C, a high electric field region (or “fast region”) develops near the anode. This stays during the cooled performance as well, indicating it represents an irreversible change to the detector. A fast anode region is another characteristic of polarization, so this confirms that the polarization process had begun in detector 935-16B1R at 2 °C.



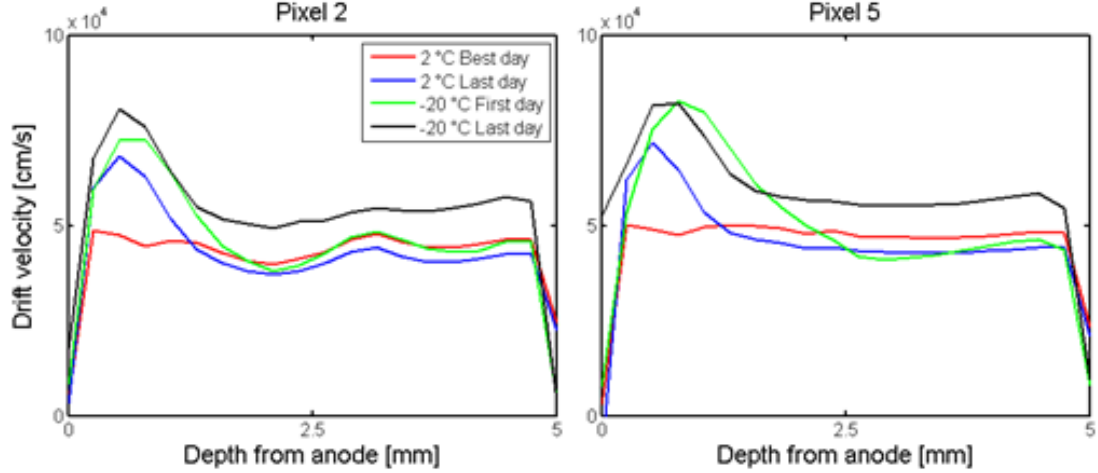


Figure 5.7: Drift velocity versus depth for two characteristic pixels of detector 935-16B1R showing the fast region which develops on the anode side during 2 °C operation.

After the testing at both temperatures, the device was polarized. No usable spectra are available because the device polarized so quickly (less than one day). Since the 2 °C operation did begin the process of polarization, this one day lifetime cannot be taken to be the expected detector lifetime. However, the detector operated reasonably at 2 °C for 26 days indicating the polarization process is significantly slower (as expected) at 2 °C. Detector 935-16B1R is older material and the expected room-temperature lifetime would be relatively short (less than 1 week) implying that the polarization rate at 2 °C is probably on the order of at least four times slower than at room temperature.

### 5.1.6 Conclusions

From operating detectors at 2 °C, the expected slower rate of polarization was observed and there exists strong evidence that polarization and conditioning rates are correlated. The polarization still appears to occur at 2 °C in older material, but may be effectively stopped at this temperature in newer material. It is possible that these long room-temperature lifetime detectors will require “burn-in” periods to achieve their best performance, unless the source of the charged impurities which

leads to conditioning is removed.

## 5.2 Surface Preparation

The second method for extending the lifetime of TlBr detectors is by surface preparation techniques which slow the interactions between the detector and the electrode material. Previous work has shown that etching with hydrochloric acid (HCl) can improve the room-temperature lifetime of planar detectors [32]. Presented here are the results of similar processing on three large volume pixelated detectors which show long room-temperature lifetimes. These detectors also show improvement with time which looks similar to conditioning.

### 5.2.1 Detectors

Two detectors were fabricated by LLNL using their updated method: detector 935-38AA2L which had Pd contacts and detector 935-38AA3L which had Pt contacts. Both detectors came from the same boule which was grown for optimal room-temperature stability.

A third detector, 125ABA2R, was fabricated by RMD, Inc. using the LLNL process and Pt contacts. This detector is also from a boule optimized for room-temperature lifetime.

### 5.2.2 Results - Detector 935-38AA2L

Detector 935-38AA2L initially operated at room-temperature for 34 days and showed very stable performance. Fig. 5.8 shows the depth-corrected single-pixel resolution versus time for room-temperature operation in the initial testing. The detector performance initially improved over the first 10 day of operation and then stayed very stable at 1.8% FWHM at 662 keV. After 35 days of room-temperature

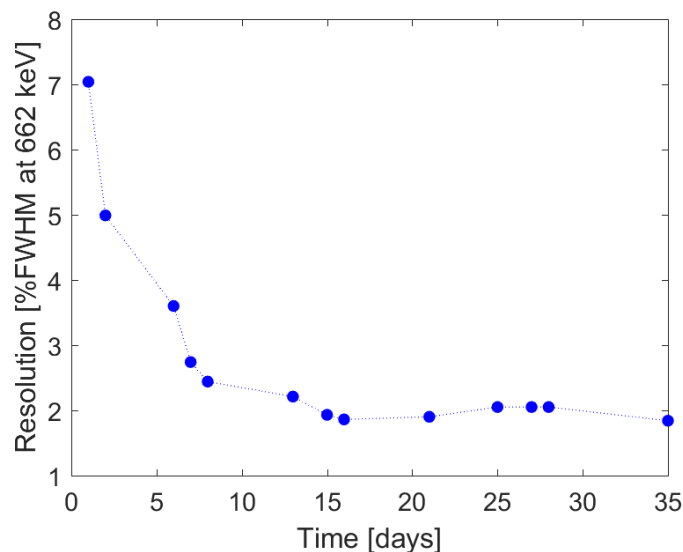


Figure 5.8: Depth-corrected single-pixel resolution versus time for the first room-temperature operation of detector 935-38AA2L.

operation the detector was biased down, it showed no sign of degradation and the measurement was only stopped so that other detectors could be tested.

Fig. 5.9 shows the raw photopeak centroids versus depth for different days of room-temperature operation of detector 935-38AA2L. The cathode side photopeak amplitude increases with time. This implies that the improving energy resolution was caused by a decrease in bulk trapping. This appears to be “conditioning,” even though conditioning is not normally observed at room temperature.

This approximately two week conditioning phase is very long compared with normal conditioning phase lengths at  $-20^{\circ}\text{C}$ . Normally conditioning takes between two and ten days. Additionally the mobility of the charged impurities whose drifts causes the conditioning should be higher at room-temperature than  $-20^{\circ}\text{C}$  implying that conditioning at room temperature should be expected to be quicker than at  $-20^{\circ}\text{C}$ . This longer room-temperature conditioning phase is consistent with the observations from the  $2^{\circ}\text{C}$  study that the longer room-temperature lifetime detectors show lower mobility of ions in the material.

After the initial testing, detector 935-38AA2L was stored for  $\sim 1$  year before retest-

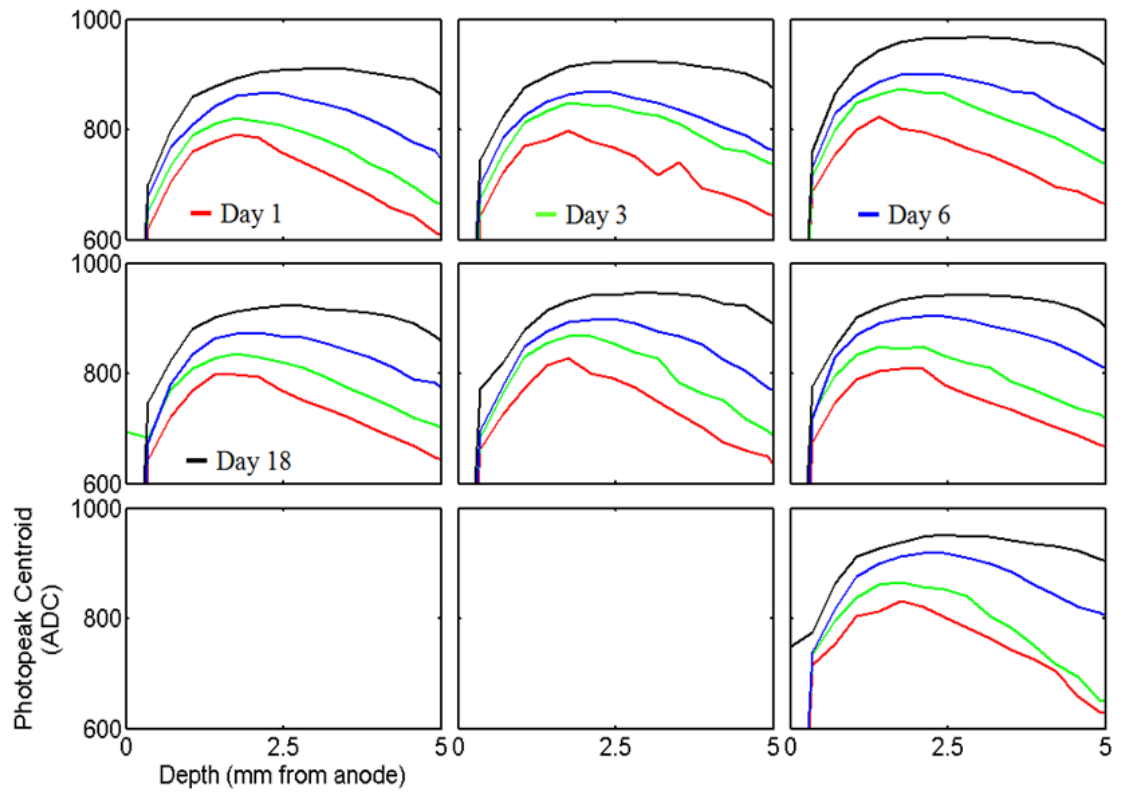


Figure 5.9: Photopeak centroids versus depth for detector 935-38AA2L at different days showing increases in the cathode side amplitude with time, indicating a reduction in overall trapping.

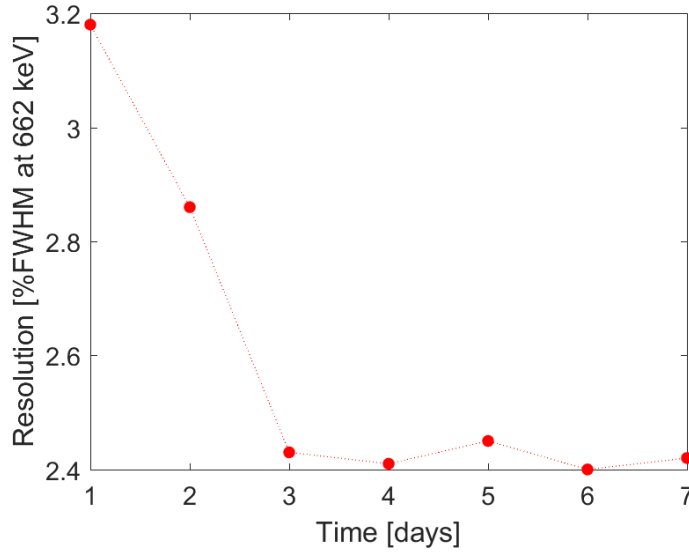


Figure 5.10: Resolution versus time for the second testing of detector 935-38AA2L at room-temperature about one year after the initial testing.

ing. Fig 5.10 shows the energy resolution versus time for the second testing of detector 935-38AA2L. The detector improves with time again, which is expected after storage of a conditioning detector [54]. Additionally, the resolution plateaus at a worse performance showing degradation from storage. This confirms that this problem (discussed in Sec. 4.3) is present in TlBr detectors regardless of their fabrication technique. Between the two testings shown in Figs. 5.8 and 5.10 and a few other short tests, detector 935-38AA2L operated for more than 50 days at room-temperature and showed no signs of polarization.

### 5.2.3 Results - Detector 935-38AA3L

Figure 5.11 shows the depth-corrected single-pixel energy resolution versus time for detector 935-38AA3L. Detector 935-38AA3L operated for more than 100 days at room temperature but experienced cathode breakdown four times throughout the measurement. This breakdown resulted in no measurable signals above noise. This kind of breakdown is not typical of the polarization process in previous detectors.

Biasing down the detector and letting it sit overnight removed the cathode break-

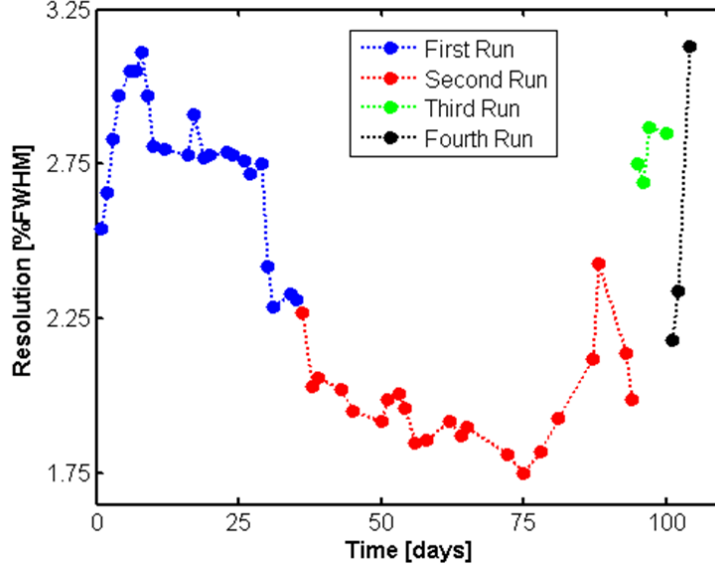


Figure 5.11: Depth-corrected single-pixel energy resolution versus time for room-temperature operation of detector 935-38AA3L. The detector experienced breakdown multiple times; each run represents continuous operation between breakdown events.

down and normal performance resumed. The performance of detector 935-38AA3L is highly varied, but does show some improvement, achieving a best day similar to that of 935-38AA2L. However detector 935-38AA3L started at a much better resolution and took much longer to achieve its best day.

Figure 5.12 shows the raw photopeak centroid versus depth for different days of operation for detector 935-38AA3L. The cathode side photopeak centroids show both an initial increase with time (shown as red to green) and then some later degradation (green to blue then black). This suggests that the improvement was similar to conditioning at room-temperature like in detector 935-38AA2L, but then after a month of operation it began to degrade slightly.

#### 5.2.4 Failure Mechanism

Testing of detector 935-38AA3L was stopped because of the breakdown. As shown in Fig. 5.11, the time between breakdown events was reducing as the device aged, making testing difficult.

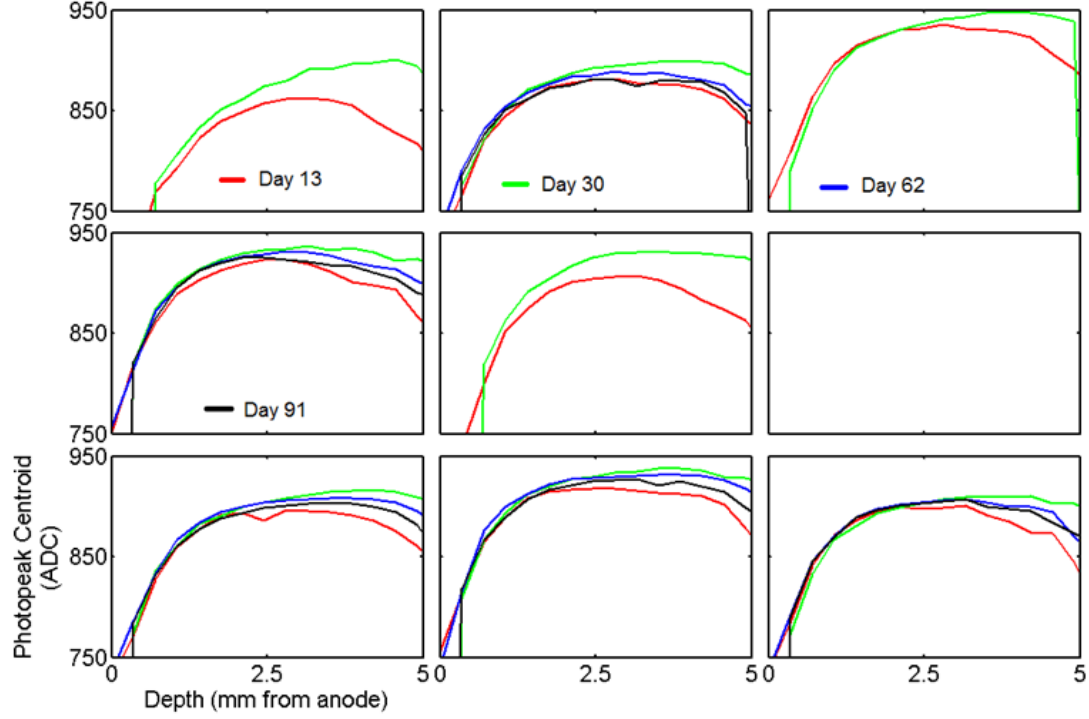


Figure 5.12: Photopeak centroids versus depth for detector 935-38AA3L at different days showing both increasing and decreasing centroids with time.

Fig. 5.13 shows photographs comparing a typical detector (detector 58A3R) and detector 935-38AA3L after room-temperature operation (similar surface discoloration is also present on detector 935-38AA2L). The room-temperature operation resulted in discoloration of the detector surface. The white compound on the surface is thallium oxide, and likely leads to the increased surface leakage current during operation and caused the sporadic cathode breakdown. There is a small brown region in one corner of the detector (shown in Fig. 5.13(a)) which is a thallium rich region. These thallium rich regions are referred to as “dentrites” and are responsible for the failure of detectors tested by LLNL. This is different from the classic polarization, where the contact enters the material.

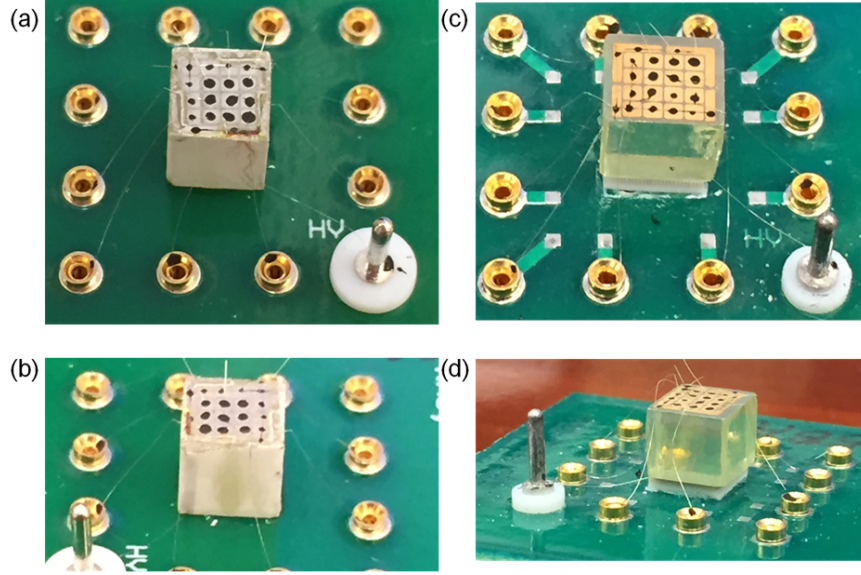


Figure 5.13: Picture of the (a) top and (b) side of detector 935-38AA3L after greater than 100 days of operation at room-temperature compared with the (c) top and (d) side of a normal TlBr detector. The side surfaces are covered in a  $\text{TlO}_x$  coating, with one corner showing a brown spot which is likely Br.

### 5.2.5 Detector 125ABA2R

One additional detector was fabricated by RMD using the LLNL processing technique and operated at room-temperature. Fig. 5.14 shows the single-pixel energy resolution versus time for this detector, 125ABA2R.

Detector 125ABA2R showed similar characteristics to the other two detectors processed by the LLNL technique. The detector went into breakdown after 8 days, and there were some issues with high leakage current which caused some pixels to be disabled during the measurement. The general trend in the six good pixels of the detector is improvement of the energy resolution over around 20 days of room-temperature operation.

Long-term testing was planned for detector 125ABA2R, but unfortunately a power flicker and a failure of the battery backup system caused the detector bias to cycle from -1000 V to 0 V and then quickly back up to -1000 V. This appears to have damaged the detector and no more testing was possible after this incident.



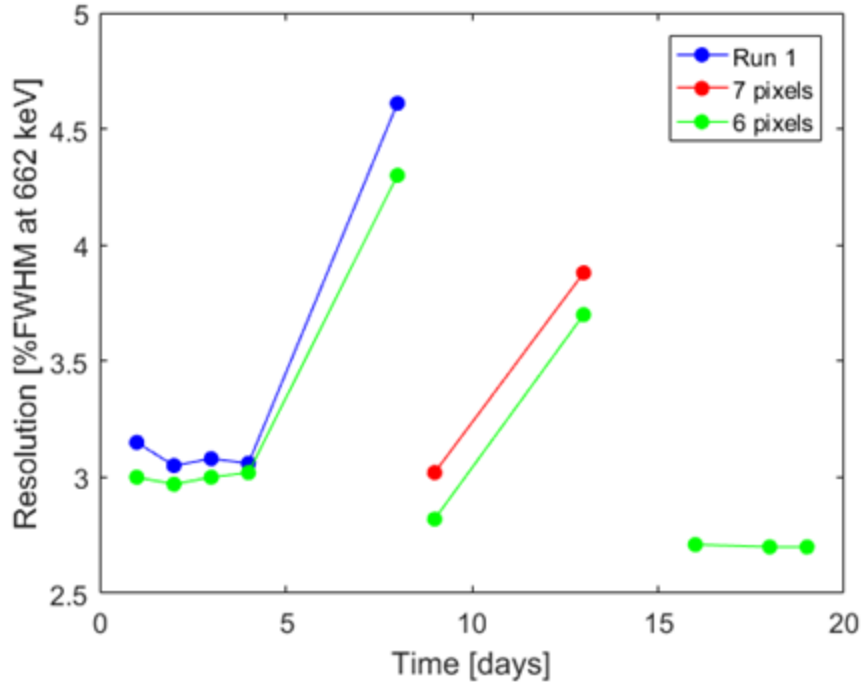


Figure 5.14: Single-pixel energy resolution versus time for detector 125ABA2R.

### 5.2.6 Conclusions

The lifetime of pixelated TlBr detectors do seem to be extended with the new processing technique with all detectors achieving near record lifetimes and detector 935-38AA3L setting a new room-temperature lifetime record. This indicates the power of the technique as well as its reliability.

All these measurements are performed under near continuous bias, and lifetimes of greater than 100 days have been observed. If the detector is only used sporadically, the lifetime could be much greater. For example, assuming use during a full-time work day (40 hrs/wk), this corresponds to 60 weeks of operation. This is much better than previously observed lifetimes, but still not to the point where commercial systems are feasible.

## CHAPTER VI

### ASIC Systems

Increasing the size of TlBr detectors is crucial for making them competitive with CZT. Currently, systems with large volume ( $20 \times 20 \times 15 \text{ cm}^3$ ) CZT crystals are commercially available [19]. Though TlBr is  $\sim 3$  times as efficient per unit volume as CZT, the  $5 \times 5 \times 5 \text{ mm}^3$  detectors are so much smaller they have significantly less total stopping power than these commercially available detectors. Additionally, larger detectors allow for better material study. It is difficult to conclude if there are bad regions in the pixelated plane with only nine pixels; whereas with a larger number of pixels, trends in the performance across the detector are much more meaningful.

As discussed in Section 3.2.2, a digital ASIC has been developed for CZT. It has 128 channels allowing for use with an  $11 \times 11$  pixelated detector. Fig. 6.1 shows a picture of the VAD-UM v2.2 digital ASIC showing its small physical size compared to the eV-509 preamplifiers used for each channel in the  $3 \times 3$  read out system.

The challenge with the VAD-UM ASIC is that many of the parameters are more fixed than with the GaGe card system. All waveforms have 160 samples and a narrower range of sampling frequencies are available. The lowest sampling frequency available on the v1.2 system is 10 MHz. This is only  $16 \mu\text{s}$  of observation time compared with the standard  $51.2 \mu\text{s}$  time used in the GaGe card system. This short collection time means that the noise will affect the waveforms more and that some-

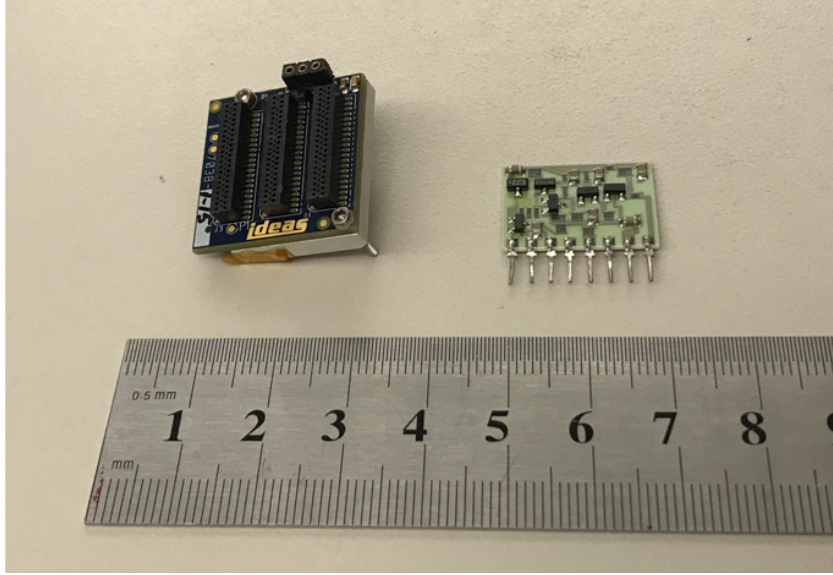


Figure 6.1: Picture of the VAD\_UM v2.2 digital ASIC capable of reading out 121 pixels compared with the eV-509 preamplifier used for reading out a single pixel in the 3x3 readout system.

times full cathode collection will be difficult or impossible. Additionally the observation time cannot be extended to quantify material effects such as hole drift or charge multiplication.

In this work, systems based on the VAD\_UM digital ASIC are developed and operated with TlBr detectors. Section 6.1 discusses the first system based on the VAD\_UM v1.2 ASIC. Section 6.2 discusses the system with the updated VAD\_UM v2.2 system which should have lower electronic noise and is capable of a lower sampling frequency. Finally, Section 6.3 discusses the prototype hand-held system developed using the VAD\_UM v2.2 ASIC and University of Michigan designed read out electronics.

## 6.1 v1.2 System

### 6.1.1 System Overview

Fig. 6.2 shows a picture of the system based on the VAD\_UM v1.2 ASIC with Fig. 6.3 showing a block diagram of the system.

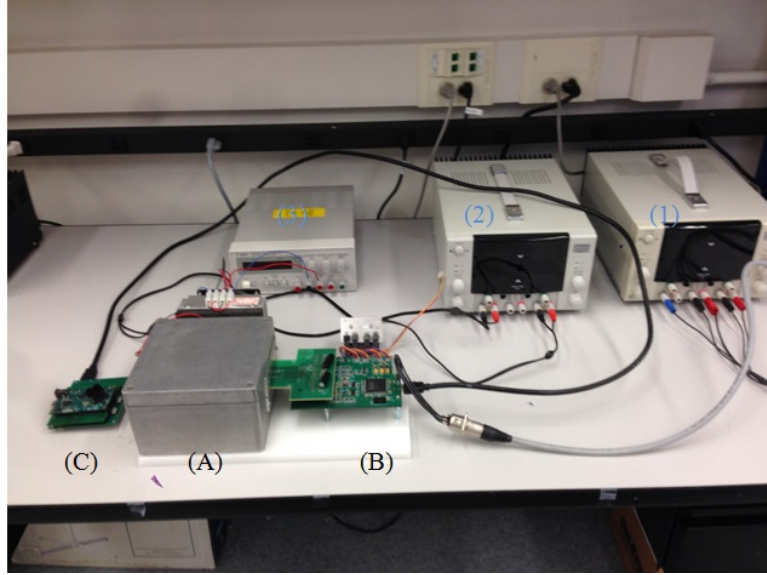


Figure 6.2: Picture of the first generation system based on the VAD\_UM v1.2 ASIC. Showing the (a) Faraday cage, (b) Espresso board, and (c) UMROB. The power supplies are also labeled based on their numbers in Fig. 6.3, with the computer and high voltage power supply off screen.

The detector is mounted on the ASIC which is connected to a carrier board to take the signals out of the Faraday cage. The carrier board is connected to the ADC board (called the Espresso board) which also powers the ASIC. The Espresso board receives +5V and -5V from a Topward 63060-10 dual tracking power supply and is connected by HDMI to an FPGA read out board called the UMROB. The UMROB receives +5V from an Aligent E3630A power supply and is connected by USB to a computer for system control and data recording.

The system has a two-stage Peltier TEC cooler which is capable of cooling the ASIC and detector to  $-18^{\circ}\text{C}$ . Fig. 6.4 shows a diagram of the cooling system. A large heat sink and fan are mounted to the outer TEC and the inner TEC is connected to a copper cold finger cools the detector and ASIC through the metal ASIC cover. Each TEC and the fan require separate power.

Both TECs are controlled by a Topward 63060-10 dual tracking power supply and the fan by the Aligent E3630A power supply (which also powers the UMROB).

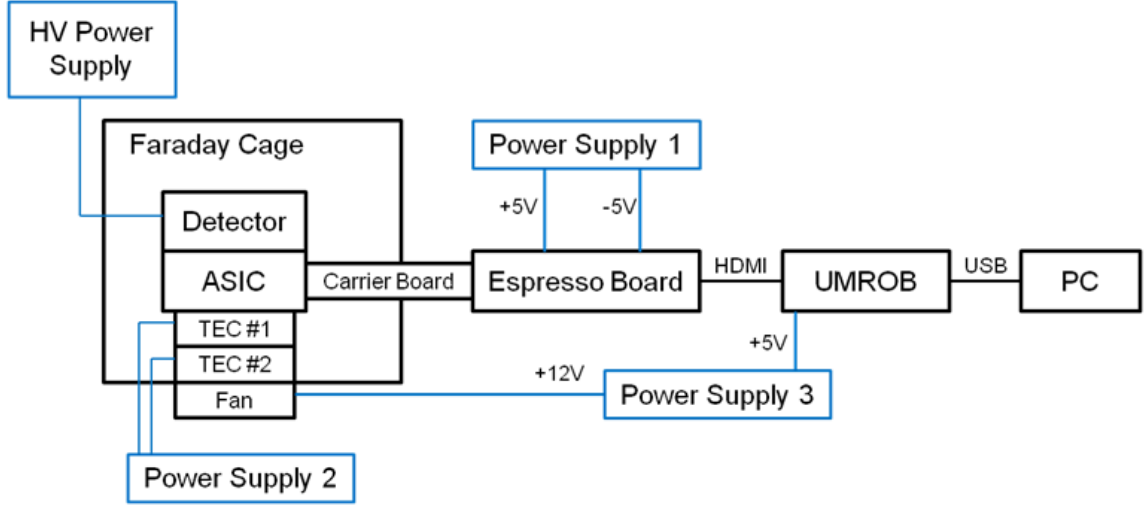


Figure 6.3: Block diagram of the v1.2 ASIC system. Power supplies and power lines shown in blue.

Additionally, the detector receives high voltage from an external Kethley Model 248 high voltage power supply. In total the system requires 3 two-channel low voltage power supplies and one high voltage power supply to operate. All these power supplies are indicated in Fig. 6.3 in blue and are connected to the parts of the system they power.

### 6.1.2 Cooling Performance

Fig. 6.5 shows the total Peltier cooling power versus ASIC temperature for the system. To cool the ASIC to  $-18^{\circ}\text{C}$ , the system requires 17 W. This is a reasonable power requirement, especially for a benchtop system. The cooling power could be reduced to only  $\sim 3$  W if the detector temperature was increased to  $2^{\circ}\text{C}$  (as discussed in Sec. 5.1).

With the initial testing of the cooling system, significant condensation occurred on the cold finger. Fig. 6.6(a) shows this condensation. The system was sealed with silicone grease and beeswax along the box lid and Drierite was placed inside the sealed box. A humidity sensor was used inside the system to monitor the humidity level. The desiccant took around two hours to reduce the humidity in the box to a very low

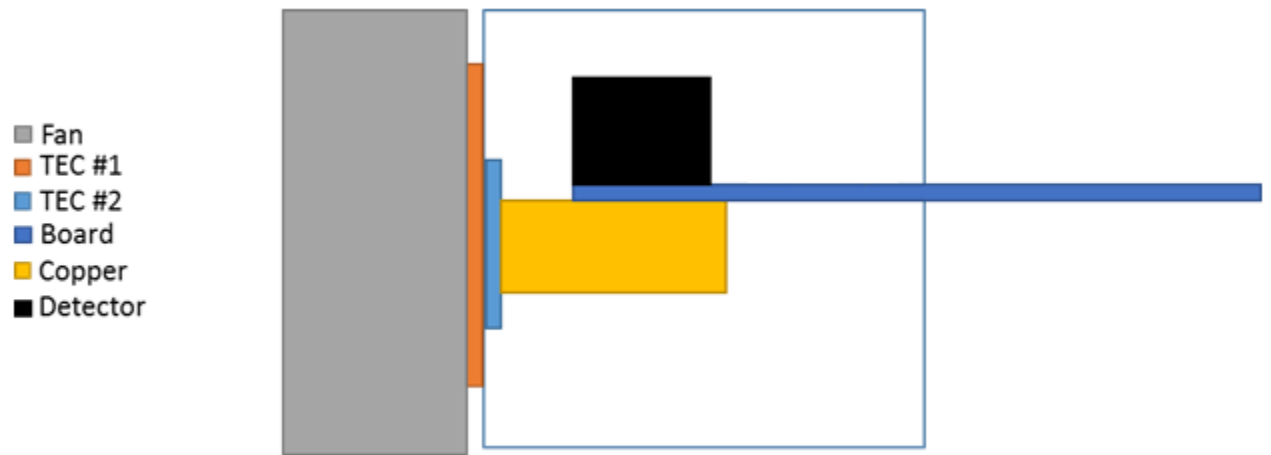


Figure 6.4: Diagram of the two-stage TEC cooling system showing the copper cold finger connected to the ASIC.

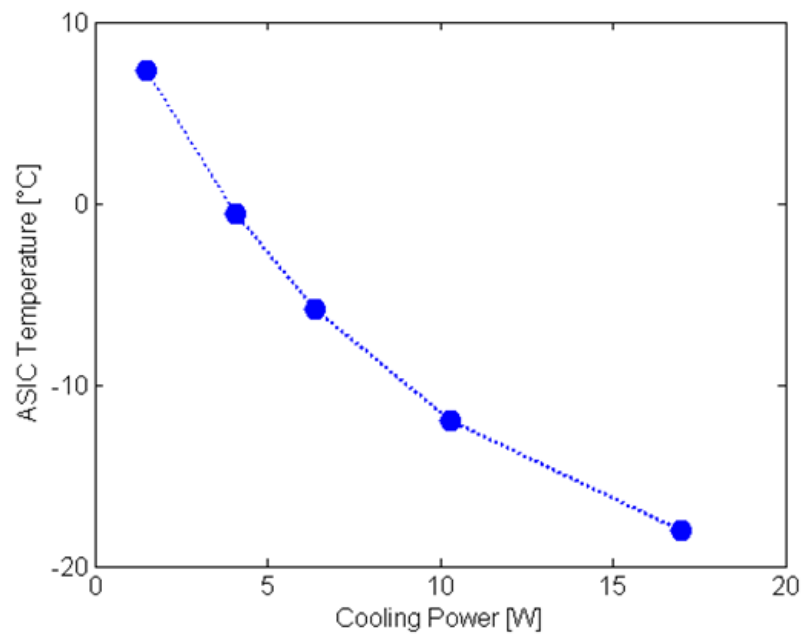


Figure 6.5: Total TEC power versus ASIC temperature for the VAD\_UM v1.2 ASIC system.

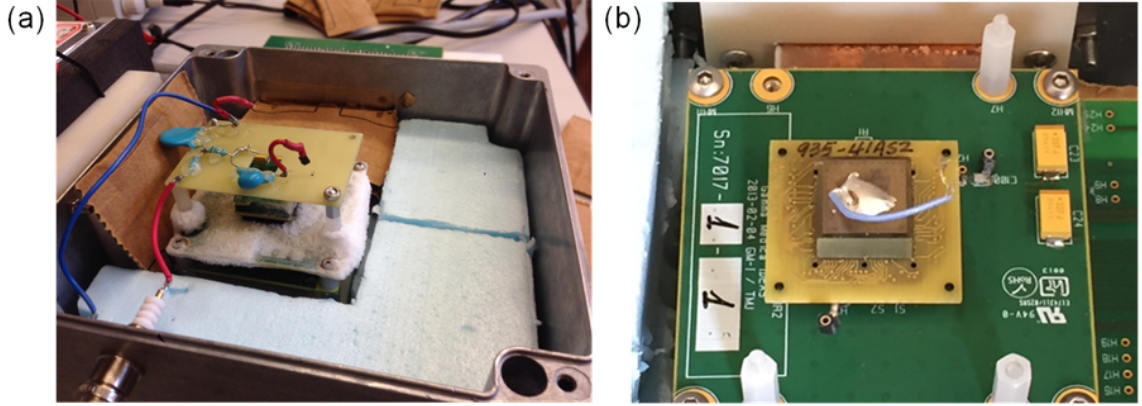


Figure 6.6: Pictures of the (a) condensation in the system and (b) the system after two weeks of operation showing the effectiveness of the condensation mitigation.

level and the sealant prevented any additional moisture from getting into system.

By sealing the system and waiting the two hours for the desiccant to work before cooling, the system could operate for greater than two weeks without any condensation. Fig. 6.6(b) shows the system after two days with no visible condensation demonstrating the effectiveness of the sealing. The condensation was effectively mitigated, but increasing the operating temperature would help reduce the cause of the problem making it easier to change detectors.

### 6.1.3 Results

#### 6.1.3.1 Waveforms

Fig. 6.7 shows a number of photopeak waveforms from detector 935-43AS6 in the v1.2 digital ASIC system. Full cathode collection is shown by the fact that even on the cathode side the waveform is not cut off in the sampling window. However only about 15 points of the baseline are recorded leading to a strong effect of noise on the amplitude determination (more than 40 points are typically used for amplitude determination in CZT waveforms [8]). The waveform tail has more points for amplitude determination, so the triggering cell was shifted to equalize the length of the baseline and tail regions. This is important especially for detectors which show

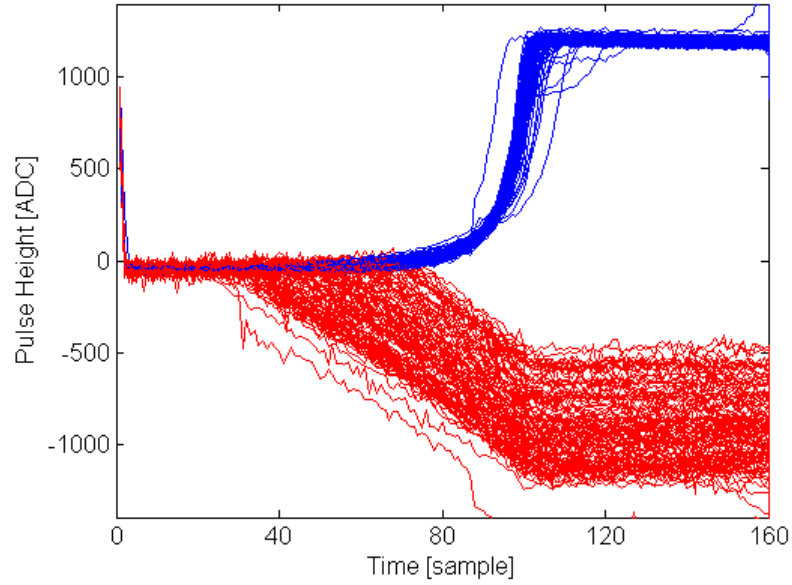


Figure 6.7: Photoppeak waveforms showing the anode (blue) and cathode (red) in the v1.2 system showing full collection on the cathode side.

conditioning, as the electric field tends to be weaker in the start leading to longer cathode waveforms. Fig. 6.8 shows this shifted triggering cell which allows for full cathode waveform collection in detector 935-40AS2 which showed a lower electric field than detector 935-43AS6.

#### 6.1.3.2 Detector Performance

Fig. 6.9(a) shows an example overall depth-corrected spectrum for cooled operation of detector 935-43AS6 with Fig. 6.9(b) showing the pixel-by-pixel resolutions. (Note: in the substrate board design, two pixels were mis-routed into connector pins which are not connected to the ASIC input channels, these pixels are shown as white boxes without resolutions in Fig. 6.9(b).)

The detector is reasonably uniform with no clear indication of bad material regions. A few pixels showed high leakage current and were disabled, this is denoted by black 0.00s in the pixel map; however, these do not show a clear trend. The best pixel achieved 1.70% FWHM with most pixels showing performance between 2.0%



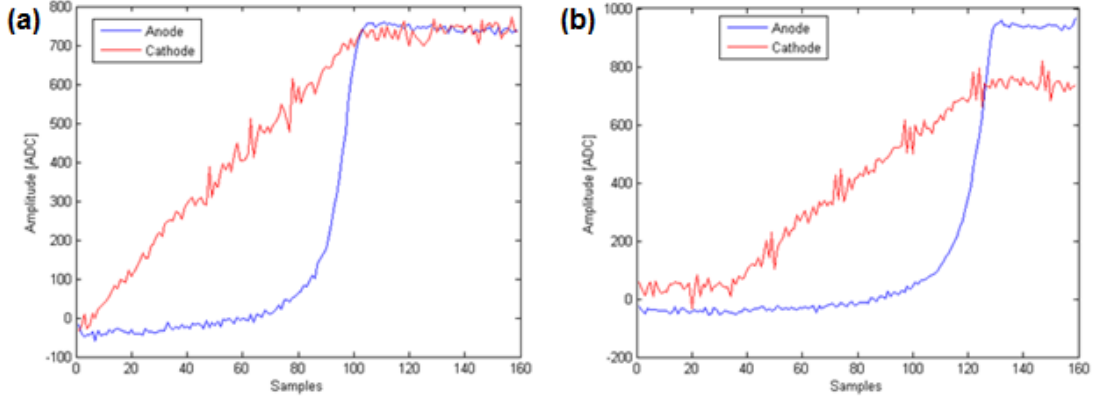


Figure 6.8: Anode (blue) and cathode (red) waveforms from the (a) standard trigger cell and (b) shifted trigger cell showing the improved ability to find the cathode amplitude for a low electric field detector (935-40AS2).

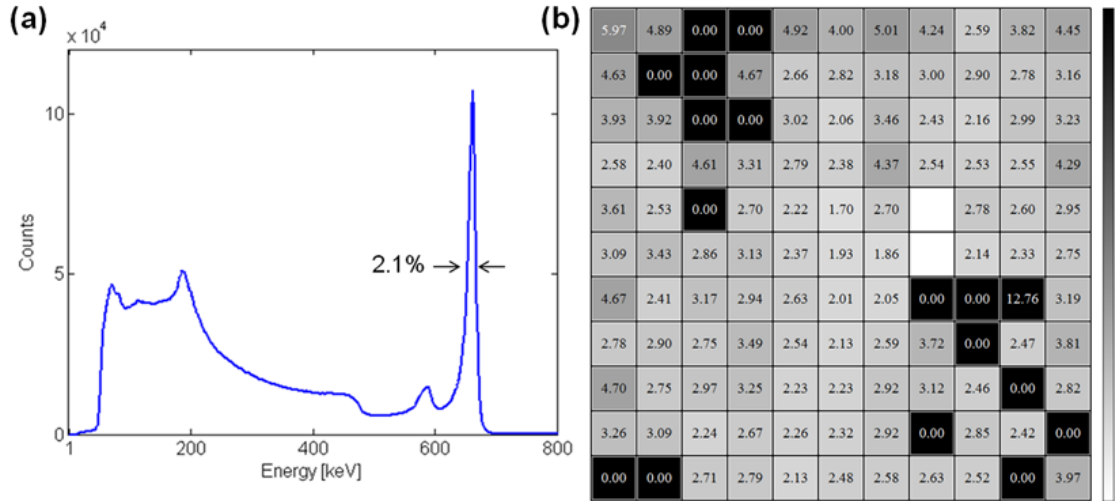


Figure 6.9: (a) Overall depth-corrected single-pixel spectra for cooled operation of detector 935-43AS6 and (b) pixel-by-pixel single-pixel energy resolution.

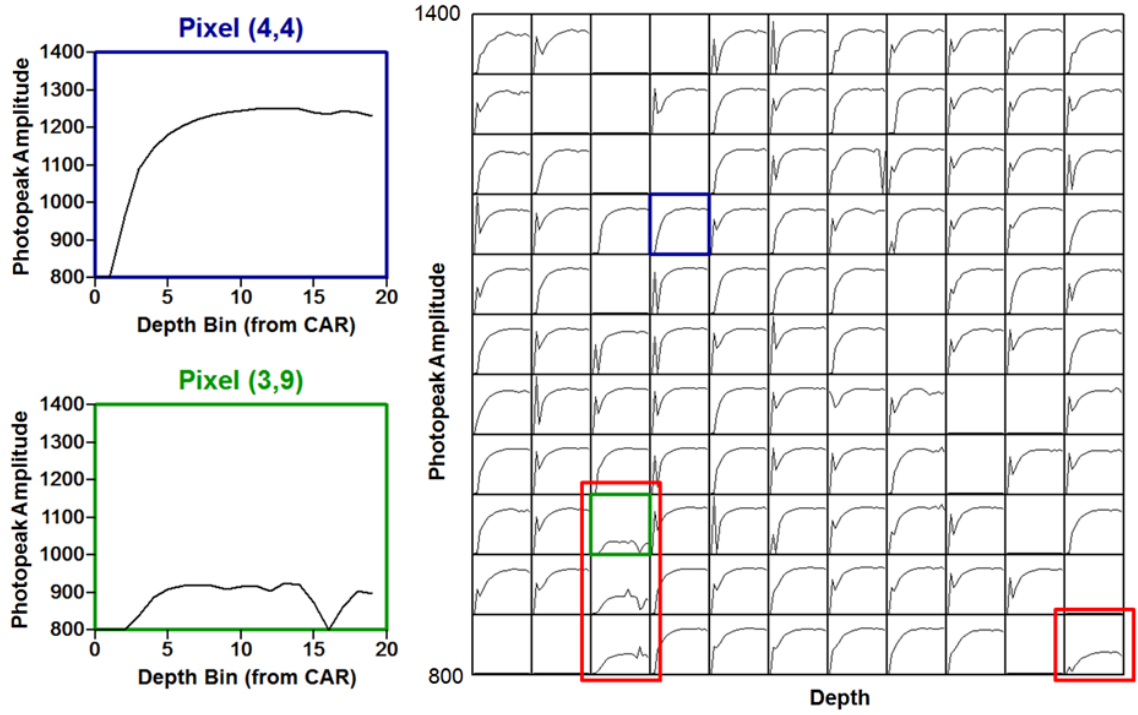


Figure 6.10: Photopeak centroids versus depth for detector 935-43AS6 showing both the low detector trapping (example highlighted in blue) and poor surface charge collection (highlighted in red).

and 2.8% FWHM. The pixels around the edge showed noticeably worse performance, but this is expected. Edge pixels tend to have more leakage current and not as uniform electric fields and thus show worse performance in CZT as well [16].

Fig. 6.10 shows the photopeak centroids versus depth for all pixels in detector 935-43AS6. In general the detector shows very little trapping. This is demonstrated by the flat profile in most pixels, with a typical pixel (4,4) shown in the top left. Four pixels show depressed amplitudes at all depths. This implies poor charge collection at the anode and is likely an indication of attachment issues in the detector. An example pixel of this type (3,9) is shown in the bottom left. The disabled pixels show no centroids in Fig. 6.10, it is possible that their high leakage was also caused by a fabrication problem. In general, the attachment was reasonable in the measured detectors, but there is still room for improvement.

Table 6.1: Summary of 11x11 detectors tested with the v1.2 digital ASIC system.

Detector	Best Resolution
<b>935-38AS3</b>	3.44%
<b>935-38AS4</b>	2.53%
<b>935-34BS3</b>	2.36%
935-43AS6	2.10%
935-40AS2	5.12%
935-41AS2	>7%
935-39BS5	3.91%

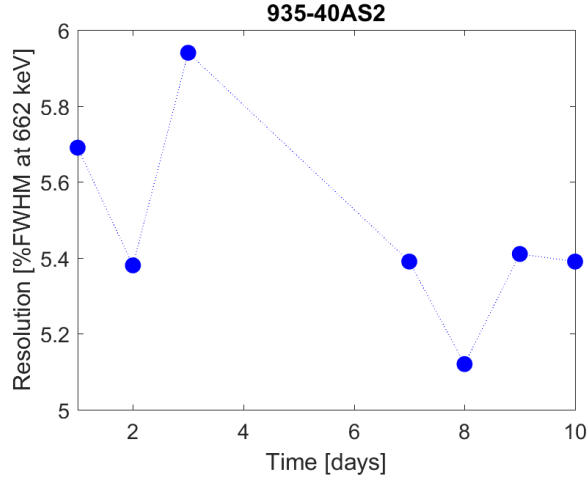


Figure 6.11: Overall single-pixel resolution in detector 935-40AS2 for cooled operation under continuous bias showing no significant improvement.

A total of seven detectors were tested with the v1.2 system and Table 6.1 shows these detectors and their best performances. Detector 935-38AS3, 935-38AS4, and 935-34BS3 are newer material and operated at room temperature. These detectors are bold in Table 6.1. Detectors 935-39BS5, 935-40AS2, 935-41AS2, and 935-43AS6 are older material and operated cooled.

Detector 935-40AS2 initially showed a weaker electric field, indicating it might condition. Consequently, it was operated for ten days at  $-18^{\circ}\text{C}$ . Fig 6.11 shows the resolution versus time for this testing. The resolution may have improved slightly during the testing, but the detector never showed great performance and did not show the strong improvement expected of conditioning material. It is likely this material is simply poor.

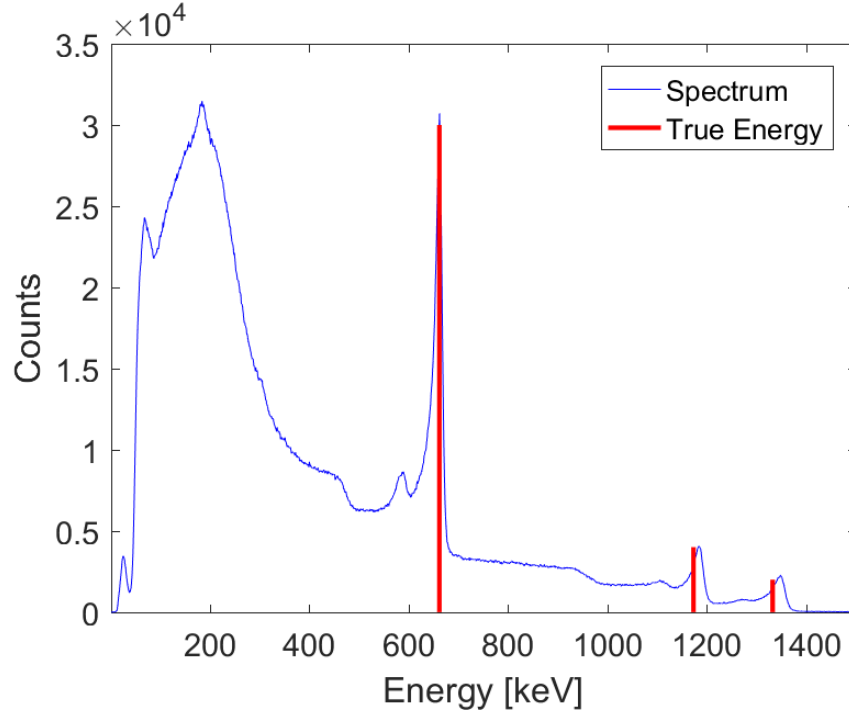


Figure 6.12: Spectrum from detector 935-43AS6 irradiated with both  $^{137}\text{Cs}$  and  $^{60}\text{Co}$ . Vertical lines indicate the true energy of each gamma-ray line.

Table 6.2: Energy non-linearity in TlBr measured in the v1.2 System

True Energy [keV]	Measured Centroid [keV]
661.7 keV	661.8 keV
1173 keV	1184 keV
1332 keV	1348 keV

### 6.1.3.3 Non-linearity

An energy non-linearity correction is required in CZT with ASIC systems. This is true for both the analog [15] and the digital [16] ASIC based systems. For CZT, the system non-linearity is dominated by non-linearity in the electronics [55]. For this reason, it should be expected that TlBr will also show some energy non-linearity which needs to be corrected.

Fig. 6.12 shows a spectrum from detector 935-43AS6 irradiated by both  $^{137}\text{Cs}$  and  $^{60}\text{Co}$ . The spectrum is energy calibrated using the 662 keV  $^{137}\text{Cs}$  peak and Table 6.2 shows the centroids of all three peaks compared with their true energy.

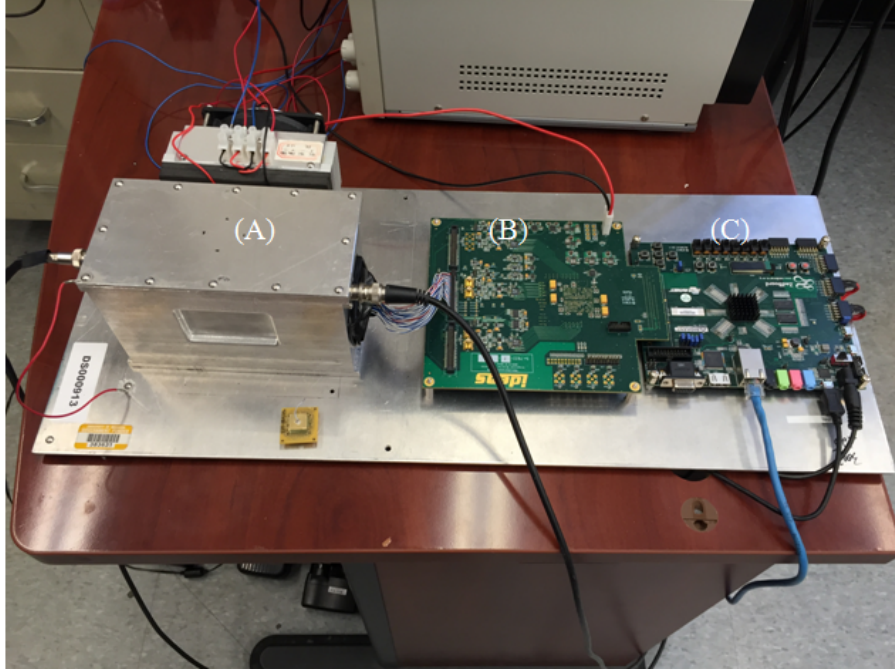


Figure 6.13: Picture of the benchtop system using the VAD\_UM v2.2 digital ASIC. Showing the (a) Faraday cage, (b) Espresso board, and (c) Zedboard. The power supplies and computer are not included. An 11x11 detector is included for scale.

The  $^{60}\text{Co}$  centroids are slightly over estimated by 11 keV and 16 keV for the 1173 keV and 1332 keV lines respectively. This is slightly higher than the non-linearity observed in CZT where the  $^{60}\text{Co}$  peaks are generally off by approximately 6 keV [8]. Previous results with 3x3 detectors have shown good linearity in TlBr, so this non-linearity should be correctable but it may be more significant in TlBr than in CZT when using the VAD\_UM ASIC electronic read out system.

## 6.2 v2.2 Benchtop System

### 6.2.1 System Overview

Fig. 6.13 shows a picture of the benchtop system based on the VAD\_UM v2.2 ASIC with Fig. 6.14 showing a block diagram of the system.

A few significant changes were made in the VAD\_UM v2.2 ASIC which affect the system design. First, the ASIC only requires positive voltages (+1.5V and +3.3V

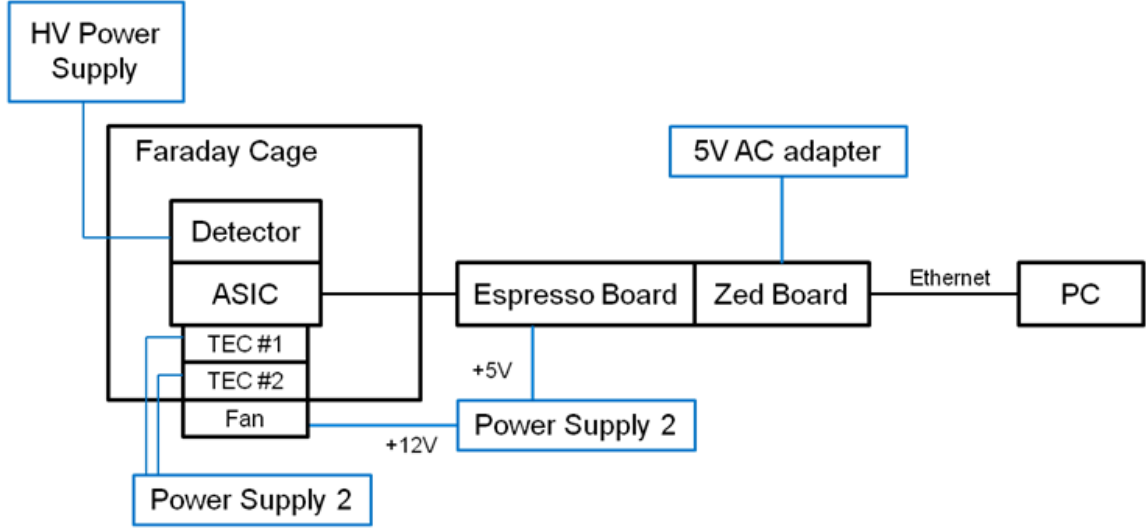


Figure 6.14: Block diagram of the benchtop system using the VAD\_UM v2.2 digital ASIC. Power supplies and power lines are shown in blue.

instead of  $+1.5$  and  $-2.0\text{V}$ ) so the Espresso board can generate the ASIC biases with only a single  $+5\text{V}$  input. This is supplied by an Aligent E3630A power supply. Secondly, the FPGA readout board was changed from the UMROB using an Opal Kelly FPGA to the ZedBoard. This board receives its power through an AC adapter, and the communication with the PC is now via Ethernet instead of USB.

The v2.2 system uses the same cooling system as the v1.2 system with only a slight redesign of the Faraday Cage, but the same thermoelectric coolers and cold finger. The two TECs are powered by a Topward 63060-10 dual tracking power supply, and have the same cooling power requirements as the v1.2 system.

The sampling frequency in the VAD\_UM ASIC is determined by both an ASIC parameter and the Espresso board master clock. The ASIC can be set to sample at the clock frequency or a fraction of the Espresso clock frequency. The available fractions are  $\frac{1}{2}$ ,  $\frac{1}{4}$ , or  $\frac{1}{8}$  of the clock frequency. In the v1.2 system, the Espresso clock is fixed at  $80\text{ MHz}$ , yielding sampling frequencies of  $10$ ,  $20$ ,  $40$ , and  $80\text{ MHz}$ . The VAD\_UM v2.2 ASIC has the capability to reduce the master clock frequency from  $80\text{ MHz}$  to  $40$ ,  $20$  or  $10\text{ MHz}$ . This allows for more sampling frequency options, with a

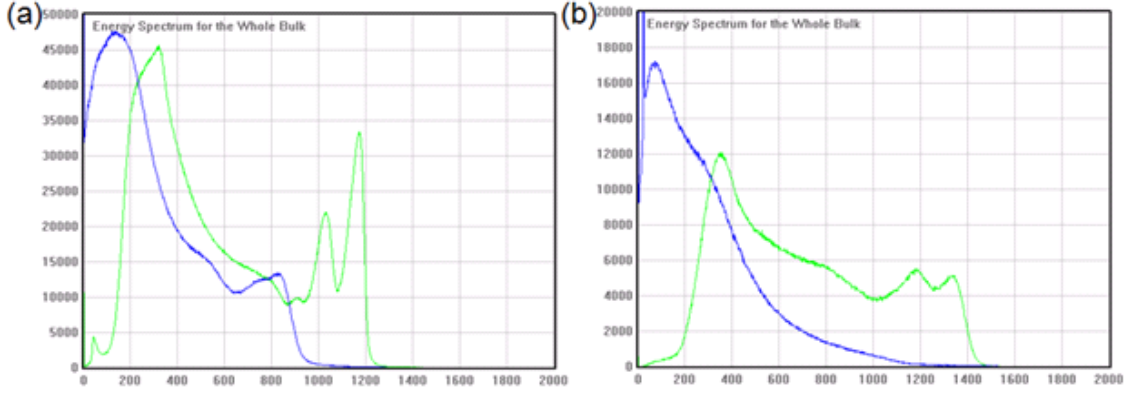


Figure 6.15: Comparison of the raw performance of detector 935-38AS4 in the (a) v1.2 system compared with the (b) v2.2 system without updated trigger settings. Data taken on subsequent days.

lowest setting of 2.5 MHz (or a  $64 \mu\text{s}$  collection time). Reducing the Espresso clock frequency, however, slows the read out time and consequently reduces the maximum count rate significantly.

### 6.2.2 Triggering

Initial testing with the VAD\_UM v2.2 ASIC showed poor performance from TlBr detectors. Fig. 6.15 shows a comparison between the performance of detector 935-38AS4 in the v1.2 (Fig. 6.15(a)) and v2.2 (Fig. 6.15(b)) systems taken on subsequent days showing the worse performance in the v2.2 system. This poor performance was coupled with a lower than expected count rate.

As indicated by the low count rate, the cause of the poor performance came from the triggering circuitry. The ASIC manufacturer made a change to the triggering system between the ASIC generations. Because the TlBr waveforms are so much slower than the CZT ones, the new fast shaper was too quick to properly trigger the system. A new default setting for TlBr was identified, slowing the fast shaper and lowering the trigger threshold and the system achieved good performance. Fig. 6.16 shows the performance of detector 935-38AS4 with the updated trigger settings.

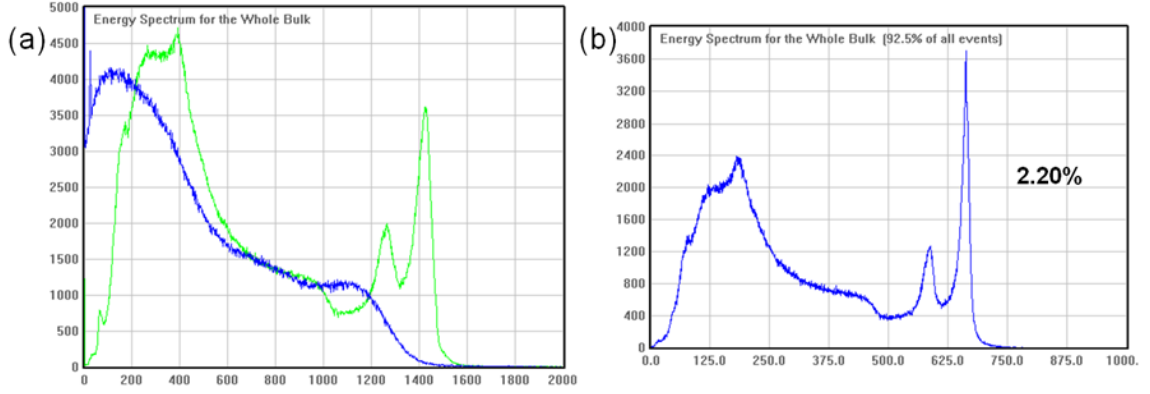


Figure 6.16: (a) Raw and (b) depth-corrected spectrum from detector 935-38AS4 showing the return to good performance after optimizing the trigger settings for TlBr.

With the updated trigger settings the new raw spectrum (Fig. 6.16(a)) shows very similar performance to the performance in the v1.2 system (Fig. 6.15(a)) taken just a day earlier.

### 6.2.3 Sampling Frequency Effects

Fig. 6.17 shows 100 photopeak waveforms from detector 935-38AS4 at 5 MHz sampling (achieved with a 40 MHz Espresso clock). With the longer 32  $\mu$ s sampling window in the v2.2 system, more points are available for amplitude determination which should lead to a decrease in the noise effect on the determined waveform amplitude.

The effects of the lower sampling frequency can also be observed in the raw cathode spectrum. Fig. 6.16(a) shows the raw cathode spectrum (blue) with a higher maximum amplitude than in Fig. 6.15(a) from the v1.2 system. The cathode spectrum in the v1.2 system seems to have a peak, but because it is at a lower amplitude, it is likely caused by incomplete charge collection. In events where the cathode waveform is not fully recorded, the amplitude is always the same causing a peak. With the lower sampling frequency (5 MHz in the v2.2 system versus 10 Mhz v1.2 system), the maximum cathode amplitude is higher and there is no longer a peak.



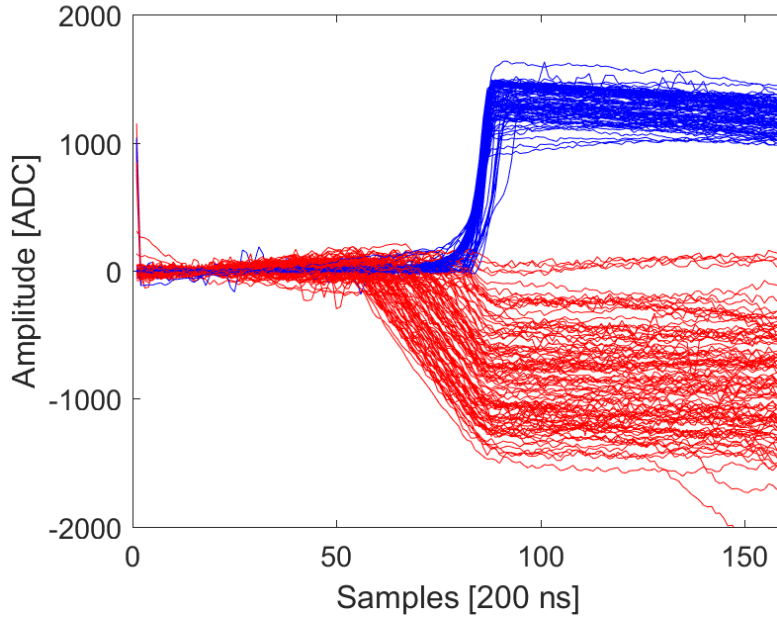


Figure 6.17: Photoppeak waveforms from detector 935-38AS4 at 5 MHz showing the ability to use more points for amplitude determination compared with the v1.2 system.

5 MHz sampling is used as default for TlBr in the v2.2 system. At high bias for good detectors, 10 MHz can be used to obtain a higher maximum count rate.

#### 6.2.4 Degradation

All of the 11x11 detectors were retested in the v2.2 system with the optimized trigger settings. Table 6.3 summarizes their performance in this system.

As discussed in Sec. 4.3, it is common for TlBr detectors to degrade from storage.

Table 6.3: Summary of 11x11 detectors tested with the v2.2 digital ASIC system.

Detector	v2.2 Resolution	Old Resolution (v1.2 System)
Testing Date:	August 2016	July 2015
935-38AS3	>7%	3.44%
935-38AS4	2.20%	2.53%
935-34BS3	>7%	2.36%
935-43AS6	2.29%	2.10%
935-40AS2	>7%	5.12%
935-41AS2	>7%	>7%
935-39BS5	4.22%	3.91%

This was also observed with the 11x11 detectors. In some of the detectors, the degradation appears to be very severe with 4 detectors showing no ability to resolve the photopeak and escape peak (denoted by  $>7\%$  resolution in Table 6.3). One detector (935-38AS4) showed improvement which was likely due to both it operating at a higher bias (2000 V) in the v2.2 system versus the previous result (1000 V) and a better depth correction from the lower sampling frequency. Two others showed very slight degradation. This significant degradation in many of the detectors during approximately one year of storage is quite unexpected.

A partial refabrication was attempted on one of the 11x11 detectors. Because it would be very difficult to separate the anodes from the substrate board without damaging the crystal, refabrication of only the cathode was attempted. The old cathode was etched off and a new electrode was deposited.

This partial refabrication did not improve the detectors performance. This is not unexpected. The degradation observed in the 3x3 detectors was uniform with depth indicating it was an anode side problem, and cathode refabrication will not improve anode degradation. The degraded performance of the 11x11s is significant because it occurred even though the anodes were somewhat sealed against substrate board. This indicates that the degradation is unlikely caused by air, though it could be caused by chemical reactions with the underfill material used to reinforce the bonding. Work is on going at RMD, Inc. to understand what changes occurred on the surface and new underfill materials are being investigated by both RMD and Polymer Assembly Technologies.

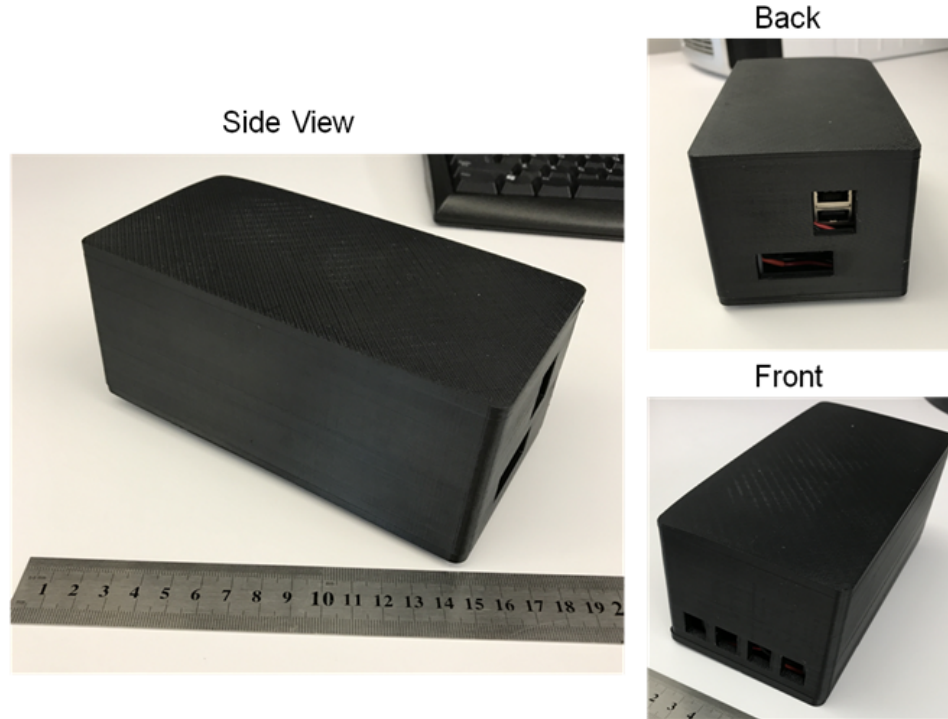


Figure 6.18: Picture of the outside of the EspressoUM handheld system. The front is where the detector is mounted and the back has openings for the power and data connectors.

### 6.3 Espresso UM Hand-held System

### 6.4 System Overview

Fig. 6.18 shows a picture of the hand-held system built with the VAD.UM v2.2 digital ASIC and the EspressoUM read out board, with Fig. 6.19 showing the interior of the system. The system requires only a single +5V power supply which could in principle be supplied by a smart phone battery backup. A computer is required for operation of the detector with the system control and data output performed over an Ethernet connection.

The miniaturization of the system was achieved by the redesign of the Espresso board. The Espresso board used in the v2.2 benchtop system was designed by Ideas, AS. and has the capability to read out up to nine ASICs. UM designed a replacement

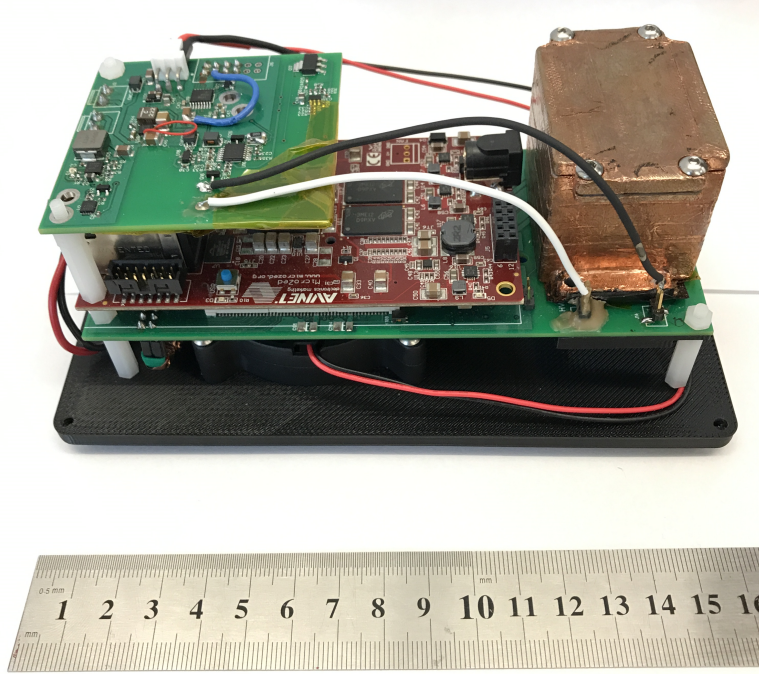


Figure 6.19: Inside of the handheld system showing the circuit boards and Faraday cage with the detector inside.

for this board (called the EspressoUM) which is designed to read out only a single ASIC and is thus optimized for a hand-held detector.

The system is enclosed in a 3D printed plastic box with exterior dimensions of  $16.5 \times 7.5 \times 8.5 \text{ cm}^3$ . The back of the enclosure has two openings for data and power, with the front having a grated opening for exhaust from the interior fan. Without any battery the system weighs less than one pound (430 g).

Fig. 6.20 shows a diagram of the handheld system. The system consists of three circuit boards. The EspressoUM, a smaller version of the ZED board (microZED) and a power board. The Faraday cage (shown as the copper box in Fig. 6.19) is mounted onto the EspressoUM board and is designed to fit a full CZT-sized detector ( $2 \times 2 \times 1.5 \text{ cm}^3$ ). The power board takes the 5V input and generates the high voltage for the detector and powers the single Peltier cooler in the system.

This hand-held system is not designed to be capable of actually cooling the detec-

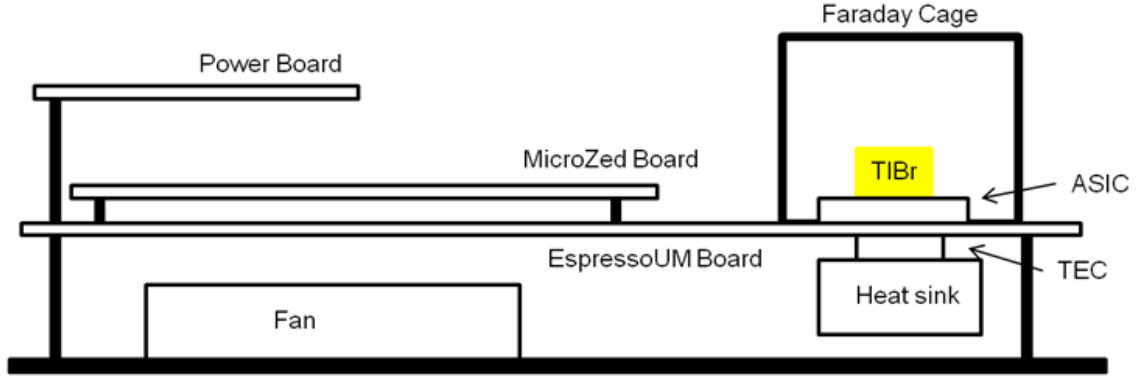


Figure 6.20: Diagram of the handheld ASIC system.

tor significantly below room temperature. The Peltier cooler is simply for removing the heat generated by the ASIC ( $\sim 0.5\text{W}$ ), to keep the detector at room temperature. A temperature sensor is located inside the Faraday cage and PID control is used to regulate the power to the cooling system to achieve this goal.

The system requires less than 0.8 A of current when the fan and Peltier are engaged, giving the system a power requirement of around 4 W. Large 5V batteries are readily available for recharging of cell phones and have capacities exceeding 8000 mAh. Using one of these for power, the system could operate for approximately 10 hours on a single charge.

#### 6.4.1 Results

Fig. 6.21 shows the raw spectrum from detector 935-38AS4 taken with the EspressoUM hand-held system. The performance is not as good as it was previously in the v2.2 benchtop system. This is due to more degradation which has occurred in the detector since the last testing ( $\sim 1$  year prior).

The performance shown in Fig. 6.21 is similar to its current performance in the v2.2 benchtop system, confirming that the electronics in the hand-held system are working properly and with better crystals good performance should be achievable.

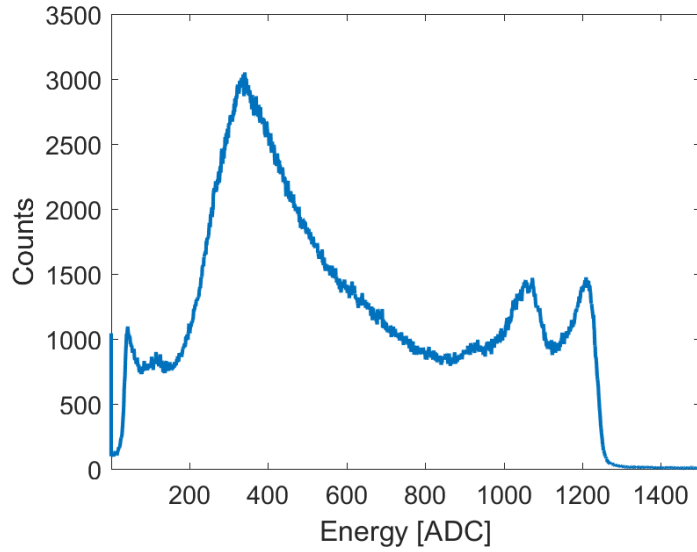


Figure 6.21: Raw spectrum from detector 935-38AS4 taken with the hand-held system.

## 6.5 Conclusions

Systems based on the VAD-UM digital ASIC have been designed and tested. The electronics for the systems show good performance. The best observed performance with TlBr was 2.2% FWHM at 662 keV for all single-pixel events. A total of seven detectors were tested and their performance degraded significantly since their original fabrication around three years ago.

A hand-held prototype system was designed and constructed, and is working well and is ready for testing more detectors as they become available.

## CHAPTER VII

# Conclusions and Future Work

### 7.1 Conclusions

Significant progress in TlBr development has been achieved in both material understanding and engineering deployment. Results with the largest ( $12 \times 12 \times 5 \text{ mm}^3$ ) detectors to date has been reported. A prototype hand-held system has been designed and tested, showing a promising for the future of TlBr based systems.

A new record lifetime for pixelated TlBr detectors of greater than 100 days was achieved using the latest advances in material growth and contact fabrication. Importantly each of the three detectors fabricated in this way all showed good room-temperature performance with long lifetimes and some improvement of energy resolution with time, indicating the reproducibility of this technique.

Intermediate temperature operation, at  $2^\circ\text{C}$ , was shown to extend the lifetime of TlBr detectors by an estimated four times. This implies that systems with only moderate cooling power requirements ( $\sim 3 \text{ W}$ ), and currently available TlBr detectors, should be able to show multi-year operational lifetimes if they are only used during working hours (2000 hrs/yr).

Improvement at both room temperature and  $2^\circ\text{C}$  similar to classic conditioning has been observed and seems to indicate that newer material optimized for room-temperature operation may still condition, but do so at a much slower rate. This

implies an important correlation between conditioning and polarization rates.

The ionization energy of TlBr was measured and shown to be conservatively  $5.49 \pm 0.10$  eV. This implies that the fundamental limiting energy resolution in TlBr is either very similar to CZT or can possibly be better depending on the Fano Factor in each material.

Degraded performance was observed in many TlBr detectors after they were stored at room temperature in a desiccator for many months or a few years. This was observed on both the small ( $5 \times 5 \times 5$  mm<sup>3</sup>) detectors and the large-volume ( $12 \times 12 \times 5$  mm<sup>3</sup>) detectors. This degradation was shown to be an anode effect and refabrication mitigated this degradation.

Finally, the cause of anode slopes on some TlBr waveforms was investigated. For this work, a digital preamplifier decay correction was developed and implemented. These anode tails were shown to correlate with hole drift distance and the energy resolution improved when they were ignored. This indicates these tails are caused by charge multiplication by drifting holes.

Numerical analysis of the amount of extra charge versus the hole trapping (calculated by operating the detector in reverse bias), shows that not enough holes are trapped to account for the anode extra charge on a one for one basis. This implies that drifting holes can free more than one electron in some TlBr detectors.

## 7.2 Future Work

Significant work remains in TlBr development including increasing detector size, reliability, and mitigating their flaws. RMD has recently fabricated even larger TlBr arrays with a size of  $12 \times 12 \times 8$  mm<sup>3</sup>. Fig. 7.1 shows a comparison of one of these detectors with both a 3x3 array and a thinner 11x11 array. These detectors show both some promising signs and indicate some ongoing challenges.

Fig. 7.2 shows the overall single-pixel spectra from the thicker detector 125BB1



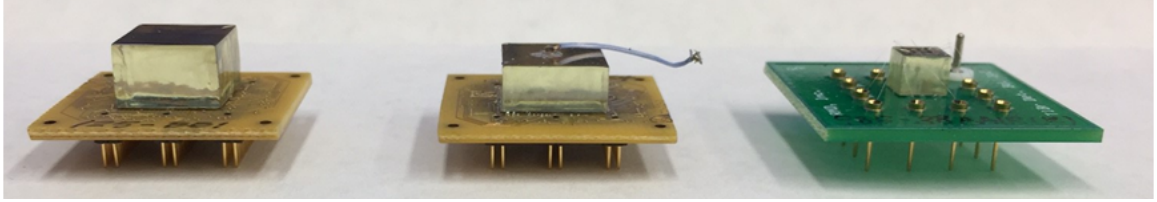


Figure 7.1: Comparison of new thicker 11x11 array with an older 11x11 array and a 3x3 detector.

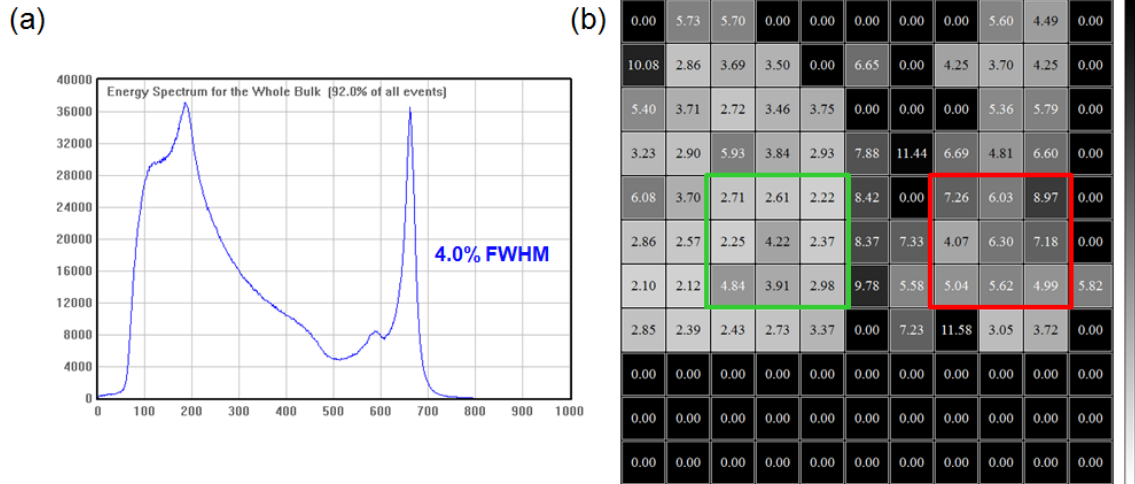


Figure 7.2: (a) Overall single-pixel spectrum from the thicker detector 125BB1 and (b) the pixel-by-pixel FWHM. The material on the left side shows significantly better energy resolution than on the right. The equivalent of a good 3x3 detector is shown highlighted in green and a bad 3x3 detector is shown in red.

and the pixel-by-pixel FWHM. The bottom three rows of pixels had to be disabled due to noise from a fabrication issue. The overall performance is marginal at  $\sim 4\%$  FWHM at 662 keV and the pixel map shows both a good region (indicated in green) where the resolution is better (about  $2\%$  FWHM) and a poor region (indicated in red). Both of these regions are the size of the active volume of a  $3\times 3$  array indicating the large variation in the performance of TlBr across even a single slice of a boule. More large detectors will allow for better feedback to the crystal growers to help improve this issue.

Performance of better than  $1\%$  FWHM at 662 keV has been achieved by multiple TlBr detectors at  $-20^\circ\text{C}$ , but no larger or room-temperature detectors have achieved this performance. The best results for large-volume detectors is about  $2\%$  FWHM overall with the best pixel achieving  $1.7\%$  FWHM. At room-temperature for the smaller arrays, the best performance is  $1.7\%$  FWHM for all single-pixel events. Both more detectors and more reliability across detectors is needed for future TlBr detectors. This can be achieved through continued growth and testing in partnership with RMD, Inc.

Several problems in TlBr, such as polarization, have already been mitigated in many ways, but other problems remain. Sealants or other techniques to help prevent degradation from storage need to be investigated. Additionally, attempts to remove the impurities which give rise to conditioning should be tested. This is especially important now that conditioning appears to happen at room temperature, with a long “burn-in” phase required before the best performances is achieved.

Finally, more digital ASIC based systems should be developed as more large volume detectors are available. Future systems should have more than one detector, seek to possibly include minor cooling, and move the computation and control of the system on board (or done through a tablet) removing the need for a computer to operate in the field.

TlBr has an exciting future and could challenge CZT in many applications if developmental progress continues.

## BIBLIOGRAPHY

- [1] Glen F. Knoll. *Radiation Detection and Measurements*. John Wiley & Sons, Inc., New York, fourth edition, 2010.
- [2] John E. M. Goldsmith, Mark D. Gerling, and James S. Brennan. A compact neutron scatter camera for field deployment. *Review of Scientific Instruments*, 87(8):083307, 2016.
- [3] Alexis Poitrasson-Rivire, Michael C. Hamel, J. Kyle Polack, Marek Flaska, Shaun D. Clarke, and Sara A. Pozzi. Dual-particle imaging system based on simultaneous detection of photon and neutron collision events. *Nuclear Instruments and Methods in Physics Research Section A: Accelerators, Spectrometers, Detectors and Associated Equipment*, 760:40 – 45, 2014.
- [4] M.C. Hamel, J.K. Polack, A. Poitrasson-Rivire, M. Flaska, S.D. Clarke, S.A. Pozzi, A. Tomanin, and P. Peerani. Stochastic image reconstruction for a dual-particle imaging system. *Nuclear Instruments and Methods in Physics Research Section A: Accelerators, Spectrometers, Detectors and Associated Equipment*, 810:120 – 131, 2016.
- [5] C. G. Wahl and Z. He. Gamma-ray point-source detection in unknown background using 3d-position-sensitive semiconductor detectors. *IEEE Transactions on Nuclear Science*, 58(3):605–613, June 2011.
- [6] E. V. D. van Loef, P. Dorenbos, C. W. E. van Eijk, K. Krmer, and H. U. Gdel. High-energy-resolution scintillator: Ce<sup>3+</sup> activated labr3. *Applied Physics Letters*, 79(10):1573–1575, 2001.
- [7] Canberra Industires Inc. NAIS-2x2 NaI(Tl) LED Temperature-Stabilized Scintillation Detector. <http://www.canberra.com/products/detectors/pdf/NAIS-2x2-SS-C38656.pdf>, 2011. [Online; accessed June 2015].
- [8] Michael Striecher. *Applications of Digitized 3-D Position-Sensitive CdZnTe Spectrometers for National Security and Nuclear Nonproliferation*. PhD Thesis, University of Michigan, 2017.
- [9] Joseph B. McCabe. *Characterization of Mechanically Cooled High Purity Germanium (HPGe) Detectors at Elevated Temperatures*. PhD Thesis, University of Tennessee, 2015.

- [10] N. J. Cherepy, S. A. Payne, S. J. Asztalos, G. Hull, J. D. Kuntz, T. Niedermayr, S. Pimputkar, J. J. Roberts, R. D. Sanner, T. M. Tillotson, E. van Loef, C. M. Wilson, K. S. Shah, U. N. Roy, R. Hawrami, A. Burger, L. A. Boatner, W. S. Choong, and W. W. Moses. Scintillators with potential to supersede lanthanum bromide. *IEEE Transactions on Nuclear Science*, 56(3):873–880, June 2009.
- [11] J.E. Eberhardt, R.D. Ryan, and A.J. Tavendale. Evaluation of epitaxial n-gaas for nuclear radiation detection. *Nuclear Instruments and Methods*, 94(3):463 – 476, 1971.
- [12] D.S. McGregor and H. Hermon. Room-temperature compound semiconductor radiation detectors. *Nuclear Instruments and Methods in Physics Research Section A: Accelerators, Spectrometers, Detectors and Associated Equipment*, 395(1):101 – 124, 1997. Proceedings of the Fourth International Workshop on GaAs Detectors and Related Compounds.
- [13] Jack F. Butler, F.Patrick Doty, Boris Apotovsky, Jean Lajzerowicz, and Loick Verger. Gamma- and x-ray detectors manufactured from cdlxznx te grown by a high pressure bridgman method. *Materials Science and Engineering: B*, 16(1):291 – 295, 1993.
- [14] H. Chen, S. A. Awadalla, K. Iniewski, P. H. Lu, F. Harris, J. Mackenzie, T. Hasanen, W. Chen, R. Redden, G. Bindley, Irfan Kuvvetli, Carl Budtz-Jrgensen, P. Luke, M. Amman, J. S. Lee, A. E. Bolotnikov, G. S. Camarda, Y. Cui, A. Hosain, and R. B. James. Characterization of large cadmium zinc telluride crystals grown by traveling heater method. *Journal of Applied Physics*, 103(1):014903, 2008.
- [15] Feng Zhang. *Events Reconstruction in 3-D Position Sensitive CdZnTe Gamma Ray Spectrometers*. PhD Thesis, University of Michigan, 2005.
- [16] Yuefeng Zhu. *Digital Signal Processing Methods for Pixelated 3-D Position Sensitive Room-Temperature Semiconductor Detectors*. PhD Thesis, University of Michigan, 2012.
- [17] M. Streicher, S. Brown, Y. Zhu, D. Goodman, and Z. He. Special nuclear material characterization using digital 3-d position sensitive cdznte detectors and high purity germanium spectrometers. *IEEE Transactions on Nuclear Science*, 63(5):2649–2656, Oct 2016.
- [18] D. Xu and Z. He. Filtered back-projection in 4picompton imaging with a single 3d position sensitive cdznte detector. *IEEE Transactions on Nuclear Science*, 53(5):2787–2796, Oct 2006.
- [19] H3D Website. Polaris H: Gamma Ray Imaging Spectrometers for Nuclear Power Plants. <http://h3dgamma.com/nuclearProducts.html>. [Online; accessed July 2015].

- [20] James Baciak. *Development of pixelated HgI<sub>2</sub> radiation detectors for room temperature gamma-ray spectroscopy*. PhD Thesis, University of Michigan, 2004.
- [21] L. J. Meng, Z. He, B. Alexander, and J. Sandoval. Spectroscopic performance of thick HgI<sub>2</sub> detectors. *IEEE Trans. Nucl. Sci.*, 53(3):1706–1712, 2006.
- [22] Alexei Churilov, William M. Higgins, Guido Ciampi, Hadong Kim, L Cirignano, Fred Olschner, and K. S. Shah. Purification, crystal growth and detector performance of TlBr. *Proc. SPIE*, 7079:70790K–70790K–8, 2008.
- [23] H Kim, L Cirignano, A Churilov, G Ciampi, W Higgins, F Olschner, and Kanai Shah. Developing Larger TlBr Detectors Detector Performance. *IEEE Trans. Nucl. Sci.*, 56(3):819–823, 2009.
- [24] V. Kozlov, M. Kemell, M. Vehkamäki, and M. Leskelä. Degradation effects in TlBr single crystals under prolonged bias voltage. *Nucl. Instruments Methods Phys. Res. Sect. A Accel. Spectrometers, Detect. Assoc. Equip.*, 576(1):10–14, jun 2007.
- [25] Will Koehler, Zhong He, Crystal Thrall, Sean O Neal, Hadong Kim, Leonard Cirignano, and Kanai Shah. Quantitative Investigation of Room-Temperature Breakdown Effects in Pixelated TlBr Detectors. *IEEE Trans. Nucl. Sci.*, 61(5):2573–2578, 2014.
- [26] Burçin Dönmez, Zhong He, Hadong Kim, Leonard J. Cirignano, and Kanai S. Shah. The stability of TlBr detectors at low temperature. *Nucl. Instruments Methods Phys. Res. Sect. A Accel. Spectrometers, Detect. Assoc. Equip.*, 623(3):1024–1029, nov 2010.
- [27] Will Koehler, Zhong He, Sean O’Neal, Hao Yang, Hadong Kim, Leonard Cirignano, and Kanai Shah. Quantification of the Conditioning Phase in Cooled Pixelated TlBr Detectors. *IEEE Trans. Nucl. Sci.*, 62(4):1785–1790, aug 2015.
- [28] Keitaro Hitomi, Tadayoshi Shoji, and Yoshio Niizeki. A method for suppressing polarization phenomena in TlBr detectors. *Nucl. Instruments Methods Phys. Res. Sect. A Accel. Spectrometers, Detect. Assoc. Equip.*, 585(1-2):102–104, jan 2008.
- [29] Keitaro Hitomi, Yohei Kikuchi, Tadayoshi Shoji, and Keizo Ishii. Improvement of energy resolutions in TlBr detectors. *Nucl. Instruments Methods Phys. Res. Sect. A Accel. Spectrometers, Detect. Assoc. Equip.*, 607(1):112–115, aug 2009.
- [30] Keitaro Hitomi, Tsutomu Tada, Toshiyuki Onodera, Seong-Yun Kim, Yuanlai Xu, Tadayoshi Shoji, and Keizo Ishii. TlBr Capacitive Frisch Grid Detectors. *IEEE Trans. Nucl. Sci.*, 60(2):1156–1161, apr 2013.
- [31] Keitaro Hitomi, Nobumichi Nagano, Toshiyuki Onodera, Seong-Yun Kim, Tatsuya Ito, and Keizo Ishii. Fabrication of double-sided thallium bromide strip

- detectors. *Nuclear Instruments and Methods in Physics Research Section A: Accelerators, Spectrometers, Detectors and Associated Equipment*, 823:15 – 19, 2016.
- [32] A. M. Conway, L. F. Voss, A. J. Nelson, P. R. Beck, T. A. Laurence, R. T. Graff, R. J. Nikolic, S. A. Payne, L. J. Cirignano, and Kanai Shah. Fabrication Methodology of Enhanced Stability Room Temperature TlBr Gamma Detectors. *IEEE Trans. Nucl. Sci.*, 60(2):1231–1236, apr 2013.
  - [33] J.H. Hubbell and S.M. Seltzer. Tables of x-ray mass attenuation coefficients and mass energy-absorption coefficients (version 1.4). Available: <http://physics.nist.gov/xaamdi>. [Online; accessed Nov 2017], National Institute of Standards and Technology, Gaithersburg, MD.
  - [34] Eiji Sakai. Present status of room temperature semiconductor detectors. *Nuclear Instruments and Methods in Physics Research*, 196(1):121 – 130, 1982.
  - [35] S. Croft and D.S. Bond. A determination of the fano factor for germanium at 77.4 k from measurements of the energy resolution of a 113 cm<sup>3</sup> hpge gamma-ray spectrometer taken over the energy range from 14 to 6129 kev. *International Journal of Radiation Applications and Instrumentation. Part A. Applied Radiation and Isotopes*, 42(11):1009 – 1014, 1991.
  - [36] Mirion Technologies. Standard electrode coaxial ge detectors. <http://www.canberra.com/products/detectors/pdf/SEGe-detectors-C49317.pdf>. [Online; accessed December 2017].
  - [37] Zhong He. Review of the ShockleyRamo theorem and its application in semiconductor gamma-ray detectors. *Nucl. Instruments Methods Phys. Res. Sect. A Accel. Spectrometers, Detect. Assoc. Equip.*, 463(1-2):250–267, may 2001.
  - [38] P. N. Luke. Single-polarity charge sensing in ionization detectors using coplanar electrodes. *Appl. Phys. Lett.*, 65(22):2884–2886, 1994.
  - [39] Z He, W Li, G F Knoll, D K Wehe, J Berry, and C M Stahle. 3-D position sensitive CdZnTe gamma-ray spectrometers. *Nucl. Instruments Methods Phys. Res. Sect. A Accel. Spectrometers, Detect. Assoc. Equip.*, 422:173–178, 1999.
  - [40] Z. He, G. F. Knoll, and D. K. Wehe. Direct measurement of product of the electron mobility and mean free drift time of CdZnTe semiconductors using position sensitive single polarity charge sensing detectors. *J. Appl. Phys.*, 84(10):5566, nov 1998.
  - [41] W. Koehler, M. Streicher, S. O’Neal, and Z. He. A correction factor to the two-bias method for determining mobility-lifetime products in pixelated detectors. *IEEE Transactions on Nuclear Science*, 63(3):1832–1838, June 2016.
  - [42] Karl Hecht. Zum mechanismus des lichtelektrischen primärstromes in isolierenden kristallen. *Zeitschrift für Physik*, 77(3):235–245, Mar 1932.

- [43] J. B. Varley, A. M. Conway, L. F. Voss, E. Swanberg, R. T. Graff, R. J. Nikolic, S. A. Payne, V. Lordi, and A. J. Nelson. Effect of chlorination on the tlbr band edges for improved room temperature radiation detectors (phys. status solidi b 6/2015). *physica status solidi (b)*, 252(6):n/a–n/a, 2015.
- [44] F. Zhang and Z. He. New readout electronics for 3-d position sensitive cdznte/hgi<sub>2</sub>detector arrays. *IEEE Transactions on Nuclear Science*, 53(5):3021–3027, Oct 2006.
- [45] Yuefeng Zhu, Stephen E. Anderson, and Zhong He. Sub-Pixel Position Sensing for Pixelated, 3-D Position Sensitive, Wide Band-Gap, Semiconductor, Gamma-Ray Detectors. *IEEE Trans. Nucl. Sci.*, 58(3):1400–1409, jun 2011.
- [46] Claude A. Klein. Bandgap dependence and related features of radiation ionization energies in semiconductors. *Journal of Applied Physics*, 39(4):2029–2038, 1968.
- [47] K.S. Shah, J.C. Lund, F. Olschner, L. Moy, and M.R. Squillante. Thallium bromide radiation detectors. *IEEE Trans. Nucl. Sci.*, 36(1):199–202, 1989.
- [48] K. Hitomi, T. Onodera, S. Y. Kim, T. Shoji, and K. Ishii. Experimental determination of the ionization energy in tlbr. *IEEE Transactions on Nuclear Science*, 62(3):1251–1254, June 2015.
- [49] R.H. Pehl, F.S. Goulding, D.A. Landis, and M. Lenzlinger. Accurate determination of the ionization energy in semiconductor detectors. *Nuclear Instruments and Methods*, 59(1):45 – 55, 1968.
- [50] G.D. Alkhazov, A.P. Komar, and A.A. Vorob’ev. Ionization fluctuations and resolution of ionization chambers and semiconductor detectors. *Nuclear Instruments and Methods*, 48(1):1 – 12, 1967.
- [51] S.D. Sordo, L. Abbene, E. Caroli, A. M. Mancini, A. Zappettini, , and P. Ubertini. Progress in the development of cdte and cdznte semiconductor radiation detectors for astrophysical and mediapl applications. *Sensors*, 9(5):3491 – 3526, 2009.
- [52] A. Holzer and M. Schieber. Reduction of Polarization in Mercuric Iodide Nuclear Radiation Detectors. *IEEE Trans. Nucl. Sci.*, 27(1):266–271, feb 1980.
- [53] Vernon Gerrish. Polarization and gain in mercuric iodide gamma-ray spectrometers. *Nucl. Instruments Methods Phys. Res. Sect. A Accel. Spectrometers, Detect. Assoc. Equip.*, 322(3):402–413, nov 1992.
- [54] Will Koehler. *Thallium Bromide as an Alternative material for Room-Temperature Gamma-Ray Spectroscopy and Imaging*. PhD Thesis, University of Michigan, 2016.



- [55] Yvan Boucher. *Analysis of Cadmium Zinc Telluride Detector Performance and Characteristics for Applications in Gamma-Ray Imaging Spectrometers*. PhD Thesis, University of Michigan, 2013.